Source Process Analysis of the 1995 Hyogo-ken Nanbu Earthquake(Dissertation_全文)

AUTHOR(S):

Sekiguchi, Haruko

CITATION:

Sekiguchi, Haruko. Source Process Analysis of the 1995 Hyogo-ken Nanbu Earthquake. 京都大学, 1999, 博士(理学)

ISSUE DATE:

1999-03-23

URL:

https://doi.org/10.11501/3149349

主論文

Rupture Process Analysis of the 1995 Hyogo-ken Nanbu Earthquake

by

Haruko Sekiguchi

A thesis presented to the

THE GRADUATE SCHOOL OF SCIENCE

KYOTO UNIVERSITY

In Partial Fulfillment of the Requirement of the Degree

DOCTOR OF SCIENCE

(Geophysical Sciences)

December 1998

ABSTRACT

This study aims to clarify the physics of the source process by detailed source process analysis and to understand the mechanism of ground motion generation during large earthquakes.

In Part #I, I investigated the source process of the 1995 Hyogo-ken Nanbu earthquake by the waveform inversion especially focusing on the fault geometry in the rupture termination. The branching possibility of Okamoto fault was suggested both by static displacement distribution and damage extension towards the east of Kobe (Nishinomiya area). In order to exclude data contaminated by the basin-edge diffracted wave into the waveform inversion process, I examined the spatio-temporal variation of its influence, and from comparison to the flat model, determined the appropriate windows for the data. Therefore, the present inversion procedure includes the largest amount of available instrumented information in the near-source region so far. The obtained source process showed that the rupture progressed upward in Awaji side; southeast of the hypocenter and went at depths larger than about 7km in Kobe side ; northeast of the hypocenter. Three subevents were identified: the largest one in the shallow part of the Awaji side, whereas the smaller two occurred at large depths (>7km) in the Kobe side. I found relatively large slips at the deep part of the branch. Total variance reduction is larger when the branch is assumed than when not. Resolution checks showed that my data set can discriminate the slips on the two branching segments, and that the slips on proposed branched portion is physical; it is not the effect of random data noise neither due to systematic errors of the Green's functions arising from misestimation of velocity structures. I conclude that branching possibility of the Okamoto fault during the Hyogo-ken Nanbu earthquake is very likely. Near-source ground motion is simulated to see the effect of slip on the branched fault using 3D FDM. Characteristic distribution of ground motion in the near-source region indicated by the damage distribution is well reproduced by modeling of both source process and wave propagation in the realistic 3-D velocity structure. The slip on the branched fault affected the ground motion in eastern part of Kobe (Nada and Higashi-Nada Ward), Ashiya and Nishinomiya City. Although its contribution is not dominant even in those regions; about 30 to 50 % in maximum velocity in frequency 0.1 to 1.0 Hz.

In Part #II, I introduced a convolution method (Ben-Menahem, 1961) which incorporate the effect of a bi-directional moving dislocation over a rectangular subfault with a point source synthetic waveform in calculation of element source waves for the waveform inversion. Each of such element source waves includes the effect of rupture

directivity itself. Therefore, the rupture directivity effect on the entire fault area is fully considered in the waveform inversion. The slip distribution inverted by these element source waves is expected to be different from that inverted by point source element waves and maybe closer to the true source process, because it seems more reasonable to expect continuous rupture distribution. For the same purpose, Wald and Heaton (1994) calculated many point sources over each subfault and summed them up considering rupture time delay (SM). Advantage of CM compared to SM is smaller computation. Only one or several Green's functions' calculation is needed for one subfault for most of the subfault-staion pairs, and a function of a finite, moving dislocation is convolved to each Green's function together with a sip time function. Appropriateness of CM is tested numerically. I examined the variation of the approximation error due to size of subfault, hypocenter distance, rupture propagation velocity and its direction by numerical tests, and showed that a ratio of right and left side of the Fraunhofer inequality condition is useful to estimate the approximation error of CM. Obtained moment release history for each subfault using this technique directly reflects the slip time function on the subfault. The inverted rupture process has a smooth slip distribution even inside the subfaults. Such a model, used as a source model in near-source ground motion simulation, escapes the problem of artificial, and large ground motion near the point sources due to the use of sparsely distributed point sources. I applied CM in the waveform inversion for the source process of the 1995 Hyogo-ken Nanbu earthquake. The global characteristics of moment release distributions are similar between two inversion results; one inverted with point source element waveforms (in Part #I) and the other with element source waves considering the finite moving dislocation effects inside each subfault. But details like places of peak moment releases differ between these two inversion results. Rise time shows a large spatial variation without remarkable depth dependence. Using the inverted source process for the Hyogo-ken Nanbu earthquake as an input, the near-source ground motions were simulated using 3-dimensional finite difference method to examine the effect of continuous rupture on the near-source ground motion simulation. Smoother distribution of the ground motion was obtained than that obtained by the source model with the sparsely distributed point sources (Part #II). Characteristics of ground motion distribution in the near-source region expected by the damage distribution are better reproduced with continuously distributed source model. Comparing the synthetic spectra at rock sites in Awaji Island and in Kobe, I found that the input ground motions at frequencies which was most effective to the damage generation (around 1Hz) were comparable in spite of the large and shallow slip in the Awaji side.

ACKNOWLEDGEMENTS

Let me express my special thanks to:

Kojiro Irikura, Tomotaka Iwata and Francisco J. Sanchez-Sesma for their encouraging advises, patience to read my poor English,

Andreas Rietbrock, Hiroshi Kawase, Michel Bouchon and Fabrice Cotton for their critical comments and sophisticated ideas,

the organizations who provided us with recordings; the Committee of Earthquake Observation and Research in the Kansai Area (CEORKA); Japan Meteorological Agency (JMA); Kansai Electric Power Co. Inc.; the Port and Harbor Research Institute; the Research Center of Earthquake Prediction of the Disaster Prevention Research Institute, Kyoto University (RCEP of DPRI, Kyoto Univ.); the Research Reactor Institute, Kyoto Univ. (RRI, Kyoto Univ.); the Public Works Research Institute (1995); Kobe City, Sekisui House Co. Inc.; Matsumuragumi Co. Inc.; and Railway Technical Research Institute, and all the other organizations whose recordings were not used explicitly in this work but gave me many useful information,

Olivier Coutant, Yasumaro Kakehi, Arben Pitarka, for helping me especially in computation codes and advises on computational techniques,

and, last but not least, all my present and former colleagues for lots of inspiration and kindness.

INDEX

PREFACE

In early 1980's, studies of kinematic source inversion to deduce slip distribution using strong ground motion data started. The kinematic source inversion is a straightforward and objective way of analyzing source process. Their results have provided important information about physics of the source. As quantity and quality of the strong ground motion data get higher and computer power become bigger, we have obtained more details of the source processes.

Their results have also been used for other related studies such as dynamic rupture modeling, tectonic stress field studies, and wave field modeling. Recently, total wave field modeling in order to understand mechanisms of ground motion generation and further to do reliable ground motion prediction for future earthquakes have been performed. The requirement of detailed and reliable source process modeling is again becoming large. It is desirable that the source modeling be reliable up to higher frequencies of engineering interests, at least 2 to 3 Hz, for waveform modeling. For waveform modeling in frequency range of engineering interests, source model should be reliable up to 2 to 3 Hz of wave generation, which is not achieved in present. For source modeling for future earthquakes we need to extract characteristics which a source should have, parameters such as source size, subevent size, rupture velocity, slip velocity, rise time, moment release (slip), and rules such as locations of rupture starting points.

The 1995 Hyogo-ken Nanbu earthquake is the first earthquake in Japan which provided strong ground motion data in the source region. Quality and quantity of the waveform data excels other earthquakes. Also many geodetic and aftershock data were recorded with high accuracy. For this reason, many scientific approaches to explain various seismological phenomena and damage features in the source region became possible.

In part #I, I explored the source process especially focusing on the fault geometry in the rupture termination. The branching possibility of Okamoto fault was suggested both by static displacement distribution and damage extension towards the east of Kobe (Nishinomiya area). There have been a numerical simulation of rupture process and geological observations which emphasized that irregularity of the rupture surface, such as fault bend and branching, works as a geometrical barrier to impede or terminate the rupture extension. But it has been still difficult to study such complex rupture geometry by the waveform inversions. This is a challenging study to judge a possibility of fault branching and examine the characteristics of slip in such a complex fault configuration by the waveform inversion. Many strong ground motion data recorded around the end region made it possible.

In part #II, I introduced a convolution method (Ben-Menahem, 1961) which incorporate the effect of a moving dislocation over a rectangular subfault with a point source synthetic waveform in calculation of element source waves for the waveform inversion. Each element source wave includes the effect of rupture directivity itself. Therefore the rupture directivity effect on the entire fault area is fully considered. The slip distribution inverted by these element source waves is expected to be closer to the true source process from that inverted by point source subfault waves.

Because it is reasonable to suppose continuous rupture distributions macroscopically. Slip history at each subfault directly indicates the slip time function separated from the rupture propagation duration. The inverted rupture process has a smooth slip distribution even inside each subfault.

Requirements of a realistic source model for near-source ground motion modeling was the motivating fact of my source analysis. Ground motion simulation near the source for the Hyogo-ken Nanbu earthquake showed that details of the source process are one cause of complicated ground motion strength distribution. This showed me the importance of the detailed source process modeling. We faced a problem that a source model represented by sparsely discretized point sources generate artificial and large velocities just above the point sources. This problem made me consider the continuous rupturing subfault.

PART I

Fault Geometry in the Rupture Termination of the 1995 Hyogo-ken Nanbu Earthquake

1.1 INTRODUCTION

What motivated me to consider branching fault model for the Hyogo-ken Nanbu earthquake was the result of near-source ground motion simulation by 3D FDM (Pitarka et al., 1998). The mechanism which caused the concentrated damage distribution, the so called "damage belt", has been intensively discussed. From the analyses of strong motion data, we have learned that rupture directivity constituting the source process, and the local surface geology including the basement topography played an important role in generation of the strong ground motion in the near-source area. To assess their combined effects, total simulations of near-source ground motions considering rupture process and 3-dimensional velocity structure were performed (Kawase et al., 1997; Pitarka et al., 1998; Furumura and Koketsu, 1998). Furumura and Koketsu (1998) and Pitarka et al.(1998) simulated near-source ground motion using 3-D finite difference method assuming the source models of Yoshida et al. (1996) and Sekiguchi et al.(1996b), respectively. They obtained a belt-shaped high ground velocity zone similar to the "damage belt" distribution. But their highest velocity zone stops around the eastern ends of Higashi-Nada ward, while the actual damage belt extended much further to the east.

From Suma to Nada ward, causative faults estimated from the aftershock hypocenter distribution (Nemoto et al., 1996) ran along the basin edge and the damage belt was formed with about 1km offset (Fig. 1.1). East of Nada ward, the estimated causative faults have strikes departing from the basin edge. On the contrary, the damage belt extended along the basin edge. The Okamoto fault, which begins near the junction of Suwayama and Gosukebashi faults (active structures estimated to be part of the causative fault system) and goes side by side with the basin edge to the east of Nada ward (Kobe City and Institute of Construction Engineering, 1998), was then suspected to have ruptured. The Okamoto fault is out of the dense aftershock zone, however several aftershocks occurred along it just after the mainshock occurrence (Fig. 1.2) (Nemoto et al., 1996). Observations of static displacements; asymmetry of the horizontal static displacement vectors on both sides of the Gosukebashi fault from triangulation observation (Hashimoto et al., 1996) and irregular fringes in the SAR interferogram around the Okamoto fault (Fig.1.3) (Murakami et al., 1995) also support the possibility of slip on the Okamoto fault. There have been geological observations (for example, King, 1986; Nakagawa et al., 1998) which emphasized that irregularity of the rupturing surface, such as fault bend and branching, works as a geometric barrier to impede or terminate the rupture extension. Kame and Yamashita (1998) studied the rupture extension by numerical calculation without specifying next rupturing surface. They found that the rupture surface tends to bend after achieving a certain level of rupture propagation velocity and terminate itself (Fig.1.4). At a certain rupture propagation velocity, surface of peak shear stress split into two, and when they permitted the rupture to branch, a branch in a lower normal stress area quickly bent and its stretch was short and the other branch in a higher normal stress area slowly extend and its stretch was long. This feature resembles very much the configuration of Suwayama, Gosukebashi and Okamoto faults. His calculation is for a virgin rock, but the essential mechanism that the rupture surface bends and then terminates is thought to be true even for a rupture on a weak zone such as

preexisting faults.

I think it worthwhile investigating the possibility of rupture on the Okamoto fault. From similar considerations, Koketsu (1998) examined possibilities of the slip on the Okamoto fault (pointed out as a part of Ashiya fault in his paper) by comparing waveform inversion result using fault plane models with and without the Okamoto fault. He concluded that there is some probability of slip on the Okamoto fault because the variance reduction of the waveform inversion with the Okamoto fault is better than that without it, but not quantitatively. In this paper I propose another fault plane model with a branched segment, the Okamoto fault.

1.2 SEQUENCE OF THE ANALYSIS

In order to investigate such a detailed rupture geometry with improved reliability, I gather a new data set adding records not used before and verified all the element of inversion. Therefore, I carried out the following steps (Fig.1.5): 1) relocate the various model fault planes, 2) examine the applicability of 1-D approximation of 3-D velocity structure to compute synthetic waveforms, 3) select the available records those more appropriate for analysis, 4) revise the 1-D velocity structure models for stations inside the Osaka basin, then 5) perform the waveform inversion, and after the inversion, 6) validate the likehood of results using numerical resolution test, and 7) simulate ground motion in near-source area by 3-D FDM.

1.3 METHODOLOGY

1.3.1 Representation of the Source in the Waveform Inversion

Faulting is represented as moment release vectors on planar surfaces. According to Aki and Richards (1980), the observation equation of ground motion at a position **x** due to a displacement discontinuity across a faulting surface Σ is

$$u_n(\mathbf{x},t) = \iint_{\Sigma} m_{pq}(\xi,\tau) * G_{np,q}(\mathbf{x},t\,;\,\xi,\tau)\, d\Sigma \qquad (1.1)$$

with,

$$m_{pq} \equiv [u_i]\, \upsilon_j c_{ijpq} \qquad (1.2)$$

where m_{pq} is the moment density tensor corresponding to slip distribution $[u_i]$, $G_{np,q}(x, t\,;\ \xi, \tau)$ is a spatial derivative of Green's tensor expressing nth component of a displacement response at a point x to a point dislocation in p-direction on a plane normal to q-direction at a position ξ, and ν is a vector normal to Σ, and c_{ijpq} is the elastic constant tensor of Hooke's law (Fig.1.6). In order to obtain a spatio-temporal rupture history (right side of (1.1)) I numerically invert ground motion data (left side of (1.1)) using the multi-time window linear waveform inversion procedure by Hartzell and Heaton (1983) in which the moment release distribution is discretized both in space and in time.

The discretization of moment release in time is achieved by putting a finite number of temporally-localized basis functions ϕ(t) at certain time intervals. The discretization in space is done by dividing the model fault planes into small subfaults. Arbitrary directed moment release on the fault plane model is realized by combination of two orthonormal unit vectors. By convolving unit moment function, ϕ (t), with the spatial derivative of Green's function representing the jth component of synthetic displacement from ith direction of moment release on lth subfault, $g_{jil}(\mathbf{x}, t0+h\Delta t)$, I prepare a matrix **A** of element waveforms,

$$A_{mn} = \int g_{jil}(\mathbf{x}, t0 + h\Delta t; l, \tau) * \varphi(\tau - (k-1)\Delta tw + trup_l) d\tau \qquad (1.3)$$

with

$$m = \sum_{j'}^{j-1} H_{j'} + (h-1), \qquad n = (k-1)IL + (i-1)L + l$$

$t0$ is an initial time of the time range of data used for analysis, $t0+h\Delta t$ means discereticized time with increment Δt, $trup_l$ is the time of rupture front arrival at the lth subfault, Δtw is interval between adjacent time windows. I, J, K, L and H_j are the total numbers of moment release directions, components of data, basis functions, subfaults, and data points of the jth component, respectively. Now the problem is to decide the weights assigned to each element slip discretized into space, time and two slip directions.

Discretized observation equation in vector form becomes

$$\mathbf{d} = A\mathbf{m} \qquad (1.4)$$

where **d** is observation data vector, and **m** is model parameter vector. We can construct observation equations in the same form as equation (1.4) with the same discretized source representation for other sites. By combining those sets for sufficient number and azimuthal coverage of observation stations, we get a large, overdetermined simultaneous equations system.

How to choose the subfault size is a problem for which no clear criterion has been established. To extract detailed information of source process, it is preferable to take as small subfaults as possible. But spatial changes finer than the smallest wave length for an analysis within a certain frequency range cannot be constrained by data. On the other hand, spatial periodicity arising from discretization of the fault is likely to generate spurious synthetic waves predominant in the corresponding frequency. I set the point source intervals so that the dominant frequency caused by the spatial periodicity is well outside the frequency range of this analysis.

In the present study I put point source grids on the fault segment planes at 2.05km intervals. The predominant frequency expected becomes slightly higher than the frequency range of the present study; 0.1-1.0 Hz. The moment release time history is modeled using six time windows, each 0.5 s apart. The slip in each time window is represented by a smoothed ramp function with 0.8 s rise time. I fixed rupture velocity at 3.1 km/s for the first time window.

1.3.2 Constraints

Although the discretized observation equation (1.4) is an overedetermined system (after combining the equations for a sufficient number of observation stations), the solution is unstable because the system includes underdetermined model parameters. Then stabilization techniques are necessary.

Various techniques (constraints) were adopted in the former source inversion studies. Non-negative constraint prohibiting back slips and/or limiting rake angle variations, and total moment release constraint are to include a priori information about global characteristics of the slip obtained from other analysis. Moment minimization and damping of singular values (Olson and Aspel, 1982) are to damp the underdeterminedness by mathematical criterions. Smoothing constraint is assigned to reduce instability or too much complexity beyond the resolvability of the data based on an inspection that slips close each other in space and in time should be similar.

1.3.2.1 Non-Negative and Rake Angle Variation Constraints

Non-negative constraints to prohibit backslips and to limit the rake angle variation is a must to suppress destructive interferences between subfaults. The nonnegative least-squares problem is solved using routine NNLS from Lawson and Hanson (1974).

1.3.2.2 Smoothing Constraints

To smooth model parameters, different measures of roughness have been proposed, most of which are based on the first and the second derivative of the model parameters with respect the spatial or temporal coordinates. In the present study I propose the following smoothing constraints.

I assign smoothing to every pair of unknown parameters n, n' with a strength normal to the inverse of the spatio-temoral distance between them,

$$r_{nn'} = \{trup_l - trup_{l'} + (k-k')\Delta tw\}V_s + rspace_{ll'} \tag{1.5}$$

and gather the smoothing equations concerning to a certain model parameter. Then one smoothing equation for the nth parameter is,

$$\left\{ \sum_{\substack{n' \\ r_{nn'} \le \frac{Vs}{f_h}}} \frac{1}{r_{nn'}} \right\} m_n - \sum_{\substack{n' \\ r_{nn'} \le \frac{Vs}{f_h}}} \frac{1}{r_{nn'}} m_{n'} = 0, \tag{1.6}$$

where $rspace_{ll'}$ is distance between lth and l'th subfault in space, V_s is a S-wave velocity at the subfaults and $n'=(k'-1)IL+(i'-1)L+l'$. The distance that smoothing reaches should be limited to a

length where S-wave travels in the period corresponding to the higher frequency limit (f_h) of the analysis.

A smoothing matrix **S** is constructed by combining equation (1.6) for all the model parameters. Then the system under scrutiny becomes,

$$\begin{bmatrix} \mathbf{A} \\ \lambda \mathbf{S} \end{bmatrix} \mathbf{m} = \begin{bmatrix} \mathbf{d} \\ 0 \end{bmatrix} \tag{1.7}$$

1.3.2.3 ABIC

When using a smoothing constraint, the resultant inversion solution depends on the value of λ, the trade-off parameter controlling the strength of the smoothing constraint. The smaller λ becomes, the better fitting between observed and synthesized waveforms I get. But the moment release distribution is too complicated because of overinterpretation of the data and the solution is unstable due to noise in the data and/or synthetic Green's functions. To determine the proper value of λ, I used Akaike's Bayesian information criterion (ABIC) (Akaike, 1980). Yoshida (1989) and Ide et al. (1996) introduced ABIC into source modeling.

When I solve the above system using least square inversion method, it means that I automatically assume Gaussian distribution of error such as,

$$P(\mathbf{d} \mid \mathbf{m}, \sigma) = (2\pi\sigma)\exp\left[-\frac{\left\| \mathbf{d} - \mathbf{G}\mathbf{m} \right\|^2}{2\sigma^2} \right] \tag{1.8}$$

for data error distribution, and

$$P(\mathbf{m}, \sigma') = (2\pi\sigma)\|\Lambda\|^{1/2} \exp\left[-\frac{\left\| \mathbf{S}\mathbf{m} \right\|^2}{2\sigma'^2} \right] \tag{1.9}$$

for parameter error distribution. $\|\Lambda\|$ is absolute value of multiplication of nonzero eigenvalue of $\mathbf{S}^T\mathbf{S}$. The ratio σ / σ' turns out to be λ. Following the idea of Akaike's Bayesian Information Criterion, a set of parameters which have the largest values in the product of the two probability distributions has the largest entropy and should occur most frequently, and extracting the information included in the simultaneous equations. The ABIC value is defined as follows (Akaike, 1980):

$$ABIC = -2\log\left[\int P(\mathbf{d} \mid \mathbf{m}, \sigma) P(\mathbf{m}, \sigma') d\mathbf{m} \right] \tag{1.10}$$

A solution is most appropriately determined in the present system when ABIC value is smallest. The ABIC value depends on unknown parameters $\{\mathbf{m}\}$ and strength parameter of smoothing, λ. We can calculate this value only after an inversion result was obtained. Then I perform several waveform inversions with different smoothing strengths, λ, calculate the ABIC value for each inversion, and find out the best set of parameters and smoothing strength.

1.4 FAULT MODEL

As I mentioned above, the source area is assumed to be planar surfaces. This is from the following reasons. First, the rupture, when appeared on the earth surface, often takes almost straight lines, which indicates that the rupture is localized within a thin planar surface. Aftershock epicenter distribution often shows planar structure, although they have some width due to uncertainty of epicenter locations or/and actual scattering of epicenters. Radiation pattern which an earthquake shows well agrees with that expected from a dislocation on a planar surface.

Model fault planes are usually assumed from surface trace of faulting, aftershock hypocenter distribution, static displacement deduced by GPS, triangulation and SAR images. Sekiguchi et al. (1996a, b) showed that particle motions in both sides of a strike slip faulting rotates in opposite direction and constrained the location of the intersection between the faulting and the earth surface.

First, I propose a new fault plane model (Fig. 1.7). The main part of the fault model was located considering many detailed studies done after the earthquake; the relocated mainshock and aftershock hypocenters by Nemoto et al. (1996, 1997), the static displacements of triangulation points by Hashimoto et al.(1996), the geodetic inversion results by Ozawa et al.(1997) and the constraints on the location of the intersection of the causative fault planes and the earth surface in Kobe city area obtained by Sekiguchi et al.(1996a, b). The fault model is segmented into five; main segments A, B, C, D (each corresponding to Nojima, Suma, Suwayama, Gosukebashi faults, respectively) and a branch, segment E, corresponding to the Okamoto fault. I perform the waveform inversion also with ABCDD' in order to examine the effect of segment E on the inversion result. Segment D' is introduced to keep the same number of parameters in the waveform inversion.

I put point source grids on the fault segment planes at 2.05km intervals. The predominant frequency expected becomes slightly higher than the frequency range of the present study; 0.1-1.0 Hz. The moment release time history is modeled using six time windows, each 0.5 s apart. The displacement in each time window is represented by a smoothed ramp function with an 0.8 s rise time. I fixed rupture velocity at 3.1 km/s for the first time window.

1.5 ROUGH EXAMINATION OF SPATIO-TEMPORAL VARIATION OF INFLUENCE OF BASIN EDGE DIFFRACTED WAVE

To obtain improved resolution in rupture distribution, I decided to use the near-source seismograms recorded on the Osaka sedimentary basin. As many researchers have pointed out, the waveforms there, especially in Kobe City area, are strongly affected by the diffraction from the

northern edge of the Osaka basin (Kawase 1995, 1996; Motosaka and Nagano, 1996; Pitarka et al., 1996). On the other hand, synthetics used in the waveform inversion are calculated assuming a flat layered velocity structure because of both computational limitation and lack of detailed underground structure information. Because the basin-edge diffracted wave produces a remarkable phase, the use of the records affected by the basin edge wave may mislead to a wrong slip distribution. Then it is necessary to evaluate the expected errors in synthetics when we approximate 3-D structure with 1-D (flat layer) structure in this area to avoid including such types of errors in the waveform inversion.

The effect of the basin edge diffracted wave differs depending on hypocenter depth and relative location of a site with respect to the source. To gauge the spatial variation of its effect, I simulated wave field in this 3D model space (Fig. 1.8) using 3-dimensional finite difference method (Pitarka et al., 1998).

Figure 1.9 shows the synthesized waveforms at stations at R_y=12km from a source at 10km depth. Solid lines correspond to the basin edge structure model while dashed lines are for the flat layered model. Cross mark (x) in each seismogram indicates the times when the difference of the two waveforms exceeds 20 % of the maximum amplitude of both traces. These differences are caused by the basin-edge diffracted waves and they propagate at a lower velocity than the apparent velocity of direct S-wave. So they affect the direct S-wave part in near-edge area but separates clearly from direct S-wave part in off-edge area. In figure 1.10, the synthesized waveforms from sources in various Ry and Zs for a site at 5km distance from the basin edge are displayed.

I found that (1) more than 10km farther from the basin edge, the whole direct S-wave part escapes the overlapping of the basin edge diffracted wave, (2) most records in Kobe City area are strongly affected from almost the beginning of the S-wave, (3) but KPI and RKI waveforms are not contaminated by the diffracted wave for the first few seconds after the S-arrival. (4) In addition, at KOB and MOT stations, several hundreds meters distant from the basin edge, the basin edge diffracted wave is not expected to have developed yet as clearly shown in Fig.1.9. Moya and Irikura (1998) has shown that the site response at low frequency range (<1Hz) at MOT is similar to that of a hard rock site, though more than 700m depth of alluvium layer is estimated there from the reflection survey analysis (e.g., Huzita, 1996).

1.6 DATA

This earthquake provided a lot of strong ground motion data in the source region, especially in the east of the hypocenter. Quality and quantity of the waveform data excels other earthquakes. Plenty of valuable data made it possible to examine such a complex fault configuration.

According to the simple examination of 1-D approximation for 3-D velocity structure, I selected 25 records (Fig. 1.11 and Table 1.2); most of them are within 100km epicentral distance. The original seismograms at stations KBU and MOT were clipped in some components. Kagawa et al. (1996) restored those seismograms based on the saturation characteristics of the servo velocity type seismographs.

1.7 VELOCITY STRUCTURE MODELS AND GREEN'S FUNCTIONS

The velocity structure modeling was done in the following way. I first construct starting model of average underground velocity structure based on geological information, preexisting structure models from reflection or refraction surveys and logging. Then I tuned the parameters of the underground structures by trial-and-error to explain the P- and S-wave travel time for the mainshock and specific phases in the aftershocks.

The models at sites inside the Osaka basin were based on the results of reflection surveys (e.g., Huzita, 1996) operated intensively after this earthquake for the depth of bedrock near the basin edge in Kobe. Velocities and densities of sedimentary layers are modelled following Kagawa et al. (1993)'s work. I assumed structures of nearly rock sites for KOB and MOT stations.

The discrete wavenumber method (Bouchon, 1981) associated with the reflection transmission method (Kennett and Kerry, 1979) were used to calculate the point source Green's functions in laterally homogeneous (1D) velocity structures. Velocity synthetics were calculated. The observed records were integrated into velocity if original records are in acceleration, and all the observed and point source synthetics were band-pass-filtered from 0.1 to 1.0 Hz and resampled with 5.0 Hz.

1.8 SOURCE INVERSION ANALYSIS

Rupture Process for Branching Fault Model

Six different source models with identical fault model, data set, Green's functions, and rake angle variation constraint with different smoothing strengths are illustrated in figure1.12. The result with λ =0.05 achieved the smallest ABIC values among the inversions I performed. I adopt this result as our source model. Misfit value drastically increases when λ exceeds 0.05. Total moment release varies a lot due to the smoothing strength. Because total moment release vary depending on how much destructive interference is suppressed by the smoothing constraint. It is understood that the total moment release values inverted assuming large number of model parameters have no high reliability.

Time progression of rupture inverted and the waveforms calculated for the ABCDE fault model are shown in figures. 1.13 and 1.14. As found in previous source inversion studies (Horikawa et al., 1996; Ide and Takeo, 1995; Sekiguchi et al., 1996b; Wald, 1996; Yoshida and Koketsu, 1996), the rupture progressed upwards in Awaji side, and went into deeper part in Kobe side. Spatial distribution is more complicated as compared to the previous results (Sekiguchi et al., 1996b) maybe because I used velocity waveforms and smaller grid spacing in the inversion. The three areas with relatively large moment release (subevents) are confirmed on segments A, B and C in agreement with our previous work. I found a subevent smaller than the above three at the bottom of the E segment. Clear contribution of the E segment is seen only at stations near this segment; there the second pulse in the waveforms are strengthened by the waves from slips on the E segment (Fig. 1.15). This kind of slips which appears at a very edge of an assumed fault plane are often suspected to be caused by either random noise contained in the data or errors in Green's functions due to

misestimation of shallow velocity structures. To examine its reliability, I performed another waveform inversion with ABCDD' model and carried out numerical resolution checks.

1.9 DISCUSSION

1.9.1 Reliability of the Solution

Reliability of the solution is a difficult thing to estimate objectively.

Das and Suhadolc (1996) discussed the influence of misassumptions of parameters such as fault size, rupture propagation velocity, seismic wave velocity structure and etc., by numerical experiments. They extracted hidden keys (important problems hidden) in the waveform inversion for a source process. First, they pointed out the significant role of non-negative constraints on moment rate on the fault. Second, they demonstrated that a faulting process is poorly reproduced when the fault is constrained to be narrower than its true width, when the rupture velocity is constrained to be lower than the true velocity, and when incorrect crustal structure is used.

In the present study, the extension of the source area on which the source process is searched for is set to cover the regions of the aftershocks distribution. Rupture velocity for the onset of the first time windows is fixed to 3.1km/s in our studies. Bouin et al.(1998) investigated the rupture process of this earthquake by analyzing the S-wave polarization of near-source ground motions and estimated that average rupture velocity ranged between 2.4 and 3.1km/s. Their estimation supports the validity of our assumption about the rupture velocity. Modeling of the underground velocity structure is restricted by limitations of both geological information and computation. Laterally inhomogeneous velocity structure modeling is practically difficult because of fine discretization of the source region. In order to find good one-dimensional horizontally layered structure models, I estimated different structures model for each sites and tuned their parameters to explain the travel time and specific phases in the observed records. On the other hand, I examined the spatio-temporal variation of the influence of the basin-edge diffracted waves observed inside the Osaka basin and eliminated the data contaminated by the phase because such diffracted waves are not produced in the synthetics by one-dimensional structure models.

1.9.2 Rupture Process for a Fault Model without Branching

I perform the waveform inversion with the ABCDD' model (without the Okamoto fault) (Fig. 1.7), and compare the result with that of the ABCDE model. Final moment release distribution for this fault model is shown in figure 1.16(b). Overall rupture distribution characteristics are similar each other. Large moment releases were not seen at the northeastern part in this case. Variance reduction is slightly higher for the ABCDE model than that for the ABCDD' model. Especially at stations near the branch, variance reduction was higher when I assumed branching.

1.9.3 Numerical Resolution Check 1: Examination of Capability of Discriminating Slips on the Segment D and E.

The first validating of our result consists in establishing whether our data set can discriminate a

slip on the segment E from that on the segment D. I computed target waveforms for the two scenarios in which homogeneous pure strike slips were assumed all over the ABCD and the ABCE. Then I performed the waveform inversion and obtained the moment release vector distributions. In both cases recovery is complete and no leak out was detected from the segment D to the segment E neither from segment E to segment D.

1.9.4 Numerical Resolution Check 2: Examination of the Effect of Random Noise to the Inversion Result

This was done to find out whether a random noise in data can generate a ghost subevent on the Okamoto fault or not. Again I assumed homogeneous pure strike slips on the areas surrounded by the bold line, and generated target waveforms (Fig. 1.17) for two conditions. In case 1, 4 subevents were assumed and in case 2, 3 subevents were assumed. I added gaussian noise to the target waveforms. The standard deviation of noise was 20% of the peak amplitude of the target waveforms. Noise level was deduced from misfitting of target and inverted waveforms for available aftershocks assuming velocity structure models used in the present waveform inversion (Bouchon et al., 1998). Because of noise and smoothing constraints in the waveform inversion, moment releases appear even out of the assumed subevent areas, especially around subevents. In the case 1, an assumed subevent at the bottom of the Okamoto fault was recovered. In the case 2, I did not get a remarkable ghost subevent there. This means that a subevent like the one I obtained at the bottom of the Okamoto fault in the real data inversion cannot be generated even assuming as much as 20% of random noise.

1.9.5 Numerical Resolution Check 3: Examination of Misestimation of the Velocity Structure to the Inversion Result

Next, I examined if the effect of misestimation of the velocity structure can generate a ghost subevent on the Okamoto fault or not. Such misestimation is supposed to induce systematic errors in Green's functions for the inversion. As explained before, I tuned velocity structure models by trial and error to achieve P, S-arrival or P-S time in the observations. But the tuning is not completely done and moreover, lateral heterogeneity of the velocity structure which is not considered in our calculation generates error in the Green's functions. The errors would be characterized by amplitude misestimation and arrival time differences, the latter one will be more severe in the waveform inversion. Average error of S-arrival times of Green's function calculated between the hypocenter subfault and the observation stations where absolute time information is available is about 3.5% of S-wave travel time. It turns out that the average seismic wave velocity in the medium is determined with about 3.5 % error in our study. I generate a set of element waveforms, give time shifts corresponding to misestimation of the average velocity whose deviation ranging following Gaussian distribution with standard deviation 3.5% of the average velocity of each station's structure model. Of course all the element waveforms which are shifted in time for structure model misestimation, are time shifted again so that the S-arrival from the hypocenter

subfault meets the S-arrival of the observation as usually done in the waveform inversion procedure. Target waveforms were calculated assuming 3 and 4 subevents in case 1 and 2, respectively, using no time shifted element waveforms (Fig. 1.18).

Recovery of the moment release distribution is not good even with only 3.5%misestimation of average seismic wave velocity. This result shows thatmisestimation of velocity structure cause large errors in the resultant solution and emphasize the importance of construction of reliable velocity structure models for the waveform inversion. Even though, in the case 1, an assumed subevent at the bottom of the Okamoto fault was recovered in the case 1 and not recovered in the case 2. This means that an subevent like what I obtained at the bottom of the Okamoto fault in the real data inversion cannot be generated by 3.5% ofmisestimation of average velocity of the seismic wave in the crust.

1.9.6 Contribution of Branching Segment to the Near-Source Ground Motion

Near-source ground motion is simulated to gauge the effect of slip on the branched fault using 3-D FDM (Pitarka et al., 1998). I used the same heterogeneous underground structure model used in Iwata et al.(1998). This model is assumed based on the results of reflection surveys (e.g., Huzita, 1996) operated intensively after this earthquake for the depth of bedrock near the basin edge in Kobe. Velocities and densities of sedimentary layers are modelled considering Kagawa et al. (1993, 1998)'s work. Bird's eye view of the sediment-bedrock interface topography in the model space is illustrated in figure 1.19. The model parameters of the underground structure are listed in Table 1.3 The size of the model space is 58km in length (in the direction of N58° E, nearly parallel to causative faults), 13.6km in width (in the direction of N148° E), and 23km in depth. Grid spacing is 120m and simulation frequency range is 0.1 to 1.0 Hz. Figures 1.20(a) and 1.20(b) show the distribution of peak ground velocity when whole moment release (inside the model space) is introduced and when moment release on only the branched fault is assumed, respectively. Characteristic distribution of ground motion in the near-source region indicated by the damage distribution (lowermost of Fig.1.20(a)) is well reproduced by modeling of both source process and wave propagation in the realistic 3-D velocity structure. The slip on the branched fault affected the ground motion in eastern part of Kobe (Nada and Higashi-Nada Ward), Ashiya and Nishinomiya City. But its contribution is not dominant even in those regions.

1.10 CONCUSION

I performed the waveform inversion for the source process of the 1995 Hyogo-ken Nanbu earthquake focusing on fault geometry and slip distribution at rupture termination. I assumed fault branching at the northeastern part of the fault plane model because such possibility was suggested by the static displacements and damage extension towards the east of Kobe (Nishinomiya area). The three main subevents are again recovered in agreement to our previous work (Sekiguchi et al., 1996b). I found a subevent smaller than the above three at the bottom of the assumed branching E

segment. Clear contribution of the E segment is seen only at stations near this segment. In such stations the second pulse in the waveforms is strengthened by the waves from slips on the E segment. Total variance reduction is larger when I assumed the branch than that when I did not. Resolution checks showed that our data set can discriminate the slip on the two branching segments, and that the slip on the branched segment is caused neither by random noise contained in the data nor by synthetic errors of the Green's function due to misestimation of shallow velocity structures.

I conclude that the scenario in which the possibility of causative fault branched and rupture advanced on to the bottom of the Okamoto fault could be very likely. I carefully eliminated the records contaminated by strong diffraction wave generated due to 3-D bedrock topography near the basin edge, and after the inversion result was obtained, I ruled out the possibility that it was caused by random noise or misestimation of shallow velocity structures.

This result agrees with the result of Koketsu (1998). He performed the joint inversion of the near- and far-field waveforms and geodetic data assuming fault models with and without the Okamoto fault branch (they call it Ashiya fault) and obtained slightly better fitting to the data when he assumed branching model.

As I briefly referred in the introduction, the static displacement and the SAR interferogram around the Okamoto fault indicate the possibility of dislocation on the Okamoto fault. No strong and conclusive evidences are found yet, but we have plenty of positive supports for rupture branching at northeastern part of the source fault.

Near-source ground motion is simulated to demonstrate the effect of slip on the branched fault using 3D FDM. Characteristic distribution of ground motion in the near-source region indicated by the damage distribution is well reproduced by modeling of both source process and wave propagation in the realistic 3-D velocity structure. The slip on the branched fault affected the ground motion in eastern part of Kobe (Nada and Higashi-Nada Ward), Ashiya and Nishinomiya City. Although its contribution is not dominant even in those regions; about 30 to 50 % in maximum velocity in frequency 0.1 to 1.0 Hz.

PART II

Source Inversion for Estimating Continuous Slip Distribution on the Fault

- Introduction of Green's Functions Convolved with a Correction Function to give Moving Dislocation Effects in Subfaults -

2.1 INTRODUCTION

Usually, a source fault in the waveform inversion used to be represented by a set of point sources placed at several kilometers intervals on planar surfaces. Such technique has the following problems.

(1) Each point source is assumed to represent a sum of moment release around it, but a wave from each of the point sources does not include rupture directivity effect itself. In this case, the rupture directivity from the total source is realized by overlapping of waves from an aggregate of the point sources. Therefore the amplitudes of the waves from the entire source area in forward directivity region are underestimated. And on the contrary, those in the backward directivity region are overestimated (Fig.2.1). The rupture directivity effect is caused by coherent overlappings of waves. It is expected that coherent overlapping of waves be gradually suppressed as the frequency of the waves become higher because of heterogeneity of wave-propagation and rupture process. Somerville et al. (1997) showed this phenomenon in observations in near-source area. They said that the rupture directivity effect is remarkable in period longer than 0.6s. The frequency range of our waveform inversion is 0.1 to 1.0 Hz where the directivity effect is strongest according to Somerville et al. (1997). Using element waves with no rupture propagation inside the subfaults in the waveform inversion,misestimation of the moment release values may happen depending on the distribution of observation stations.

(2) Obtained moment release history on each point source includes both slip time function and rupture propagation effect inside each subfault. It is impossible to separate them because rupture propagation inside each subfault is not defined.

(3) Recently, total wave field modeling considering both of source process and wave propagation in realistic 3-D structure have been performed in order to understand the mechanisms of ground motion generation and further to do reliable ground motion prediction for future earthquakes have been performed. If a source model represented by sparsely distributed point sources is used as an input to such ground motion simulations, the highly concentrated sources near the earth surface can generate artificial, and large ground motion around themselves.

Considering the facts listed above, it is desired to take into account rupture propagation inside each subfault. In order to give rupture directivity to slips on each subfault, Wald and Heaton (1994, 1996) calculated synthetic waves from many point sources over each subfault (25 point sources in Wald, 1996) and summed them up considering rupture time delays (SM). But this method requires a lot of the Green's functions' calculation. In fact, Wald and Heaton (1995) did interpolation of the Green's functions to reduce the amount of computation.

In the present study, by convolving a function representing bi-directional moving-dislocation on each subfault with the point source synthetic wave from each subfault center (CM), we get an approximate synthetic wave from a uniformly distributed slip inside the subfault successively activated and propagating into arbitrary directions. Advantage of CM compared to SM is smaller computation. Only one or several Green's functions' calculation is needed for one subfault And when a station-subfault distance is large compared with the linear dimension of the subfault,

waveforms calculated by CM are close to those calculated by SM summing an infinite number of point sources.

The representation of moving dislocation effect in convolutional form is first formulated by Ben-Menahem (1961). He evaluated Love wave and Rayleigh wave from a finite moving source and showed that source dimension and rupture propagation velocity play important roles in radiation pattern when the size of source becomes order of dominant wavelength of radiated waves. Aki (1968) added unidirectional moving dislocation effect to grid point sources using this method in forward modeling of the observed waveforms recorded at 80m distance from the causative fault during the 1960 Parkfield earthquake.

The inverted rupture process using the element source waves by CM has continuous slip distribution even inside each subfault. The obtained moment release time history on a subfault directly reflects the slip time function at any point on the subfault. Such a model, used as an input of near-source ground motion simulation, avoid the problem of artificial, and large ground motions around the point sources due to the use of sparsely distributed point sources.

2.2 METHODOLOGY

2.2.1 Moving Dislocation Inside Subfaults by Convolution in a Homogeneous Media

The representation of moving dislocation effect in the convolutional form in a homogeneous is deduced as follows, being modified from Sato (1969).

A displacement field from a double couple point source is expressed as,

$$U_n(\mathbf{x},t) = M_{pq}(\xi,\tau) * G_{np,q}(\mathbf{x},t;\xi,\tau) \tag{2.1}$$

where $M_{pq}(\xi, \tau)$ is a moment tensor representing dislocation in p-direction on a plane normal to q-direction at a position ξ, and $G_{np,q}(x,t;\xi,\tau)$ is a spatial derivative of Green's tensor representing nth component of a displacement response at a point x to the impulse source $M_{pq}(\xi, \tau)$.

Now I consider a rectangular subfault with length L and width W on $\xi_1\,\xi_2$-plane, dislocations parallel to the plane uniformly distributed inside the subfault, and a propagating rupture on it. A displacement field from this extended source is,

$$\begin{aligned} U_n(\mathbf{x},t) &= \iint_{\Sigma} m_{pq}(\xi,\tau) * G_{np,q}(\mathbf{x},t;\xi,\tau) d\xi \\ &= \iint_{\Sigma} \sum_{p=\xi 1,\xi 2} m_{p\xi_3}(\xi_1,\xi_2,\tau) * G_{np,\xi_3}(\mathbf{x},t;\xi_1,\xi_2\tau) d\xi_1 d\xi_2 \end{aligned} \tag{2.2}$$

where m_{pq} is the moment density tensor. When the extension of the subfault is much smaller than the distance between a reference point (the center of the subfault) and a station, and 2nd (higher) order micro terms in difference of two distances; one between the reference point ((ξ_1, ξ_2) = (0,0)) and a station and one between an arbitrary point on the subfault and the station, is negligible, the

Green's function from an arbitrary point on the subfault to the station approximates to that from the reference point after correctimg time delay due to difference of location (hereafter, I call it "plane wave approximation".)

$$G_{np.q}(\mathbf{x},r;\xi,\tau) \cong G_{np.q}(\mathbf{x},t-t_d;0,\tau) \tag{2.3}$$

$$t_d = \begin{cases} \dfrac{1}{Vp}\left(\dfrac{\xi\, x}{R}\right) = \dfrac{1}{Vp}\left(\dfrac{\xi_1 x_1 + \xi_2 x_2}{R_{\xi_1\xi_2}}\right) & (for\ P-wave\ part) \\ \dfrac{1}{Vs}\left(\dfrac{\xi\, x}{R}\right) = \dfrac{1}{Vs}\left(\dfrac{\xi_1 x_1 + \xi_2 x_2}{R_{\xi_1\xi_2}}\right) & (for\ S-wave\ part) \end{cases} \tag{2.4}$$

where (x_1, x_2) is a station location in the subfault coordinate and $R_{\xi 1, \xi 2}$ is distance between the reference point and the station projected onto the $\xi_1\ \xi_2$-plane ($R_{\xi 1, \xi 2}$= sqrt (x_1**2 + x_2**2)), Vp and Vs are P- and S-wave velocities, respectively, at the source location. A condition to be satisfied for making the plane wave approximation is the same as what should be satisfied for the region of Fraunhofer diffraction in optics (see Aki and Richards, 1980. Hearafter I call it "Fraunhofer (inequality) condition".)

$$L_{eff}{}^2 << \frac{\lambda R}{2} \tag{2.5}$$

where L_{eff}, λ, R are a linear dimension of a source area, wavelength, and distance between a receiver and the source.

I assume a common moment release function (i.e., common mechanism and time history) over a subfault and linear rupture front propagation whose velocity in ξ_1 and ξ_2 directions are V_{r1} and V_{r2}, respectively, then,

$$m_{p\xi_3}(\xi_1,\xi_2,\tau)\Big|_{p=\xi_1,\xi_2} = m_{0\,p\xi_3}\left(0,0,\tau-\frac{\xi_1}{V_{r1}}-\frac{\xi_2}{V_{r2}}\right)\Bigg|_{p=\xi_1,\xi_2} \tag{2.6}$$

Substituting (2.4) for S-wave part (direct S-wave is dominant in the waveform inversion) and (2.6), (2) becomes,

$$U_n(\mathbf{x},t) = \sum_{p=\xi_1,\xi_2}\left\{\iint_{\Sigma} m_{0\,p\xi_3}\left(0,0,\tau-\frac{\xi_1}{V_{r1}}-\frac{\xi_2}{V_{r2}}\right) * G_{np,\xi_3}\left(\mathbf{x},t-\frac{1}{Vs}\left(\frac{\xi_1 x_1}{R_{\xi_1\xi_2}}+\frac{\xi_2 x_2}{R_{\xi_1\xi_2}}\right);0,0,\tau\right) d\xi_1 d\xi_2\right\} \tag{2.7}$$

Taking Fourier transform of both sides of the above formula,

$$U_n(\mathbf{x},\omega) = \sum_{p=\xi 1,\xi 2}\left[m_{0\,p\xi_3}(0,0,\omega) G_{np,\xi_3}(0,0,\omega) \iint \exp\left\{ -i\left(\frac{\xi_1}{Vr_1}+\frac{\xi_2}{Vr_2}\right) - i\frac{1}{Vs}\left(\frac{\xi_1 x_1}{R_{\xi_1\xi_2}}+\frac{\xi_2 x_2}{R_{\xi_1\xi_2}}\right)\right\} d\xi_1 d\xi_2 \right]$$

$$= \sum_{p=\xi 1,\xi 2}\left[m_{0\,p\xi_3}(0,0,\omega) G_{np,\xi_3}(0,0,\omega) \iint \exp\left\{ -i2Xs\left(\frac{\xi_1}{L}\right) - i2Ys\left(\frac{\xi_2}{W}\right)\right\} d\xi_1 d\xi_2 \right]$$

$$= \sum_{p=\xi 1,\xi 2} m_{0\,p\xi_3}(0,0,\omega) G_{np,\xi_3}(0,0,\omega) LW \frac{\sin Xs}{Xs}\frac{\sin Ys}{Ys} \qquad (2.8)$$

with

$$Xs = \frac{\omega L}{2Vs}\left(\frac{Vs}{Vr_1} - \frac{x_1}{R_{\xi_1\xi_2}}\right) \qquad Ys = \frac{\omega W}{2Vs}\left(\frac{Vs}{Vr_2} - \frac{x_2}{R_{\xi_1\xi_2}}\right) \qquad (2.9)$$

From equation (2.8) it is understood that displacement field from a rectangular finite moving dislocation is obtained by convolving Green's function with a common moment density function and a "finite moving dislocation function",

$$\frac{\sin Xs}{Xs}\frac{\sin Ys}{Ys} \qquad (2.10)$$

2.2.1 Extension to an Inhomogeneous Medium

More generally, arrival time difference of direct S-wave, τ_d in (2.3), can be written as,

$$t_d = \frac{1}{Vs}\left(\xi_1 r_{01} + \xi_2 r_{02}\right) \qquad (2.11)$$

r0 = ($r0_1$, $r0_2$, $r0_3$) : takeoff vector of ray at the source

Then equation (2.9) becomes,

$$Xs = \frac{\omega L}{2Vs}\left(\frac{Vs}{Vr_1} - r_{01}\right), \qquad Ys = \frac{\omega W}{2Vs}\left(\frac{Vs}{Vr_2} - r_{02}\right) \qquad (2.12)$$

Practically, I perform ray tracing to obtain the takeoff vector of direct S-wave ray for each subfault-station pair.

2.3 QUANTITATIVE ESTIMATION OF ERRORS DUE TO APPROXIMATION IN CM

As I saw in the previous section, the applicability of CM is based on the plane wave

approximation assumption. The Fraunhofer inequality condition (2.5) is qualitative and cannot be used to estimate the approximation error expected for a given set of (L, λ , R). I assume that the right side of the Fraunhofer inequality divided by the left side,

$$C_{fraun} = \frac{\lambda R}{2L^2} \tag{2.13}$$

with

$$\lambda = t0 + \frac{L}{Vr1} \pm \frac{Leff}{Vs},$$

works as an index to predict the approximation error, and try to find a critical value of it to give sufficiently small error by numerical tests.

The amount of the approximation error depends on the takeoff vector of direct S-wave ray (**r**) as well as on the distance R between the center of the subfault and a station, source size L and wavelength λ, because the effective source extensions seen from stations vary with the takeoff vectors. When rupture propagation inside the subfault is considered, the amount of error also depends on rupture propagation direction (measured by angle, δ, between rupture propagation direction and subfault strike) and velocity (V_{rup}). I search for a condition to give quantitative error estimation required for plane wave approximation combined with moving dislocation in the following process.

I 1) search a condition of (**r**, δ , V_{rup}) to give the maximum error for fixed (L, R), 2) examine how the approximation error varies with R for fixed L and the "worst set" of (**r**, δ , V_{rup}) found in 1), determine the value of R to give a 10% error as critical distance for corresponding L, determine $C_{fraun,critical}$ corresponding to 10% error, and 3) examine the change of error when L and R varies keeping $C_{fraun,critical}$ for a fixed (**r**, δ , V_{rup}) .

In the following numerical tests, I calculate target waveforms to be compared with waveforms by CM using SM with sufficient number of point sources. The accuracy of numerical integration increases as the discretization interval become small. I have found that the point source interval of about 400m (5 x 5 point sources on a 2km x 2km subfault) is enough to well realize the directivity effect in the frequency range of our present study.

The subfault is a square in shape. The approximation errors are measured with misfits between waveforms by CM and those by SM. The misfit is defined as summation of square residuals between the two waveforms divided by maximum of the three components of the summation of square amplitudes of the target waveforms,

$$Misfit = \frac{\int (d_{SM} - d_{CM})^2 dt}{Max_{icmp=1,2,3}\left\{\int d_{SM}{}^2 dt\right\}} \tag{2.14}$$

because in the waveform inversion observed and synthetic waveforms at each station are normalized by the maximum amplitude of the three components of the observation. The calculated waveforms were bandpass-filtered in the range from 0.1 to 1.0 Hz which is the same frequency

range as that used in the waveform inversion.

In the first step of the numerical test, I fixed L = 2km, R = 10km, and rake of slip vector = 180° . Varying V_{rup} from 50 to 100 % of Vs, and δ from 0 to 360° , the waveforms at stations in various directions **r** (denoted by θ and ϕ) are calculated by both CM and SM (Fig.2.2). The stations are distributed at about every 10° in θ and ϕ . Although throughout the numerical tests, the dip angle of the subfault and the rake angle of slip is fixed, all possible situations are covered using symmetry in a discrete manner because δ , θ and ϕ vary in the ranges indicated above. Examples of the waveforms by both methods for one V_{rup} and one **r** and for various δ are shown in figure 2.3 Compilation of the approximation errors for all the cases I calculated is shown in figure 2.4. The data are omitted from plotting of figure 2.4 when the takeoff vector is in nodal direction of the radiation pattern of the corresponding component (less than 10% of the maximum radiation). The misfit is largest when V_{rup} is smallest in the range I tested, δ is around 170° – 180° , and in the direction of station No.33.

In the second step, I calculated the waveforms fixing L = 2.0km, fixing the "worst set" of (**r**, δ , V_{rup}); δ = 170° , V_{rup} = 0.5Vs, station No. 33 (θ = 75° and ϕ =85°), and varying R = 5 ~ 40km. The misfit decays almost proportionally to the inverse of R, and gets 10% error (*Misfit* = 0.1) at R = 16.3km (Fig.2.5). This is the critical distance for L = 2.0km. C_{fraun} value for the condition of the critical distance was 13.6 when L = 2.0km.

In the third step, to assess whether C_{fraun} can be an index to evaluate errors in a waveform by CM originated from the plane wave approximation, I examined the variation of misfit for fixed (**r**, δ , V_{rup}), when L and R are varied keeping C_{fraun} =13.6, which is the value at the critical distance for L = 2.0km. The misfits kept constant level as I expected for larger distances (Fig.2.6). But for smaller distances, the misfits are smaller than those expected from C_{fraun}. This is because the wavelength corresponding to the predominant frequency of the filtered waveform is larger than the characteristic wavelength evaluated from L. Effectively C_{fraun} become larger than 13.6. From these results, it is confirmed that the C_{fraun} is useful for estimating the maximum error from the plane wave approximation for any hypocenter distance and subfault size. By calculating C_{fraun} value, I can judge whether only one Green's function from a reference point inside a subfault to a station is enough to approximate to a path effect between any point inside the subfault and the station. If the subfault-station distance is smaller than the critical distance for a given subfault size from the viewpoint of C_{fraun}, I can divide the subfault into smaller pieces so that the piece size satisfy the $C_{fraun} > C_{fraun,critical}$. Then I can apply CM for each piece.

2.4 APPLICATION TO THE WAVEFORM INVERSION OF THE HYOGO-KEN NANBU EARTHQUAKE

2.4.1 Flow of Element Source Waveforms Preparation

On introducing CM to calculation of element source waveforms for the waveform inversion, I take the following process (Fig.2.7) considering the applicability condition examined in the previous section. After locating model fault planes and discretizing them into small subfaults, I

calculate distances between every pair of subfault and station. If the distance between a pair of subfaut and station is larger than the critical distance for a given subfault size, I calculate one Green's function between the center of the subfault and the station, and convolve it with the "finite moving dislocation function" and the element slip time function (equation (2.8)). If the distance is smaller than the critical subfault-station distance, I calculate the critical source size to satisfy $C_{fraun} > C_{fraun,critical}$ for the distance, subdivide the subfault into smaller pieces so that the size of the pieces is smaller than the critical source size, calculate the Green's functions between point sources on all the pieces and the station, convolve them with the "finite moving dislocation function" and the element slip time function, then sum them up considering the rupture time delays to get one element source waveform for one subfault. Equation (2.7) can be rewritten as follows when subdiving of a subfault into smaller pieces is required.

$$U_n(\mathbf{x},t) = \sum_{i=1}^{Ns^2} \sum_{p=\xi_1,\xi_2} \left\{ \iint_{\Sigma_i} m_{0\xi_3}\left(0,0,\tau - \frac{\xi_1}{V_{r1}} - \frac{\xi_2}{V_{r2}}\right) * G_{np,\xi_3}\left(\mathbf{x}, t - \frac{1}{V_s}\left(\frac{\xi_1 x_1}{R_i} + \frac{\xi_2 x_2}{R_i}\right); \xi_{0_i1}, \xi_{0_i2}, \tau\right) d\xi d_1 \xi_2 \right\} \qquad (2.15)$$

where Ns^2 is the number of the subdivision required. (ξ_{0i1}, ξ_{0i2}) is the coordinate of the center of ith piece and R_i is the distance between the point (ξ_{0i1}, ξ_{0i2}) and the station projected onto the ξ_1, ξ_2-plane. Transformed into the frequency domain, (2.15) becomes,

$$U_n(\mathbf{x},\omega) = \sum_{i=1}^{Ns^2} \sum_{p=\xi_1,\xi_2} \left[m_{0\xi_3}(0,0,\omega) * G_{np,\xi_3}(\xi_{0_i1}, \xi_{0_i2}, \omega) \frac{LW}{N_s^{\,2}} \frac{\sin X_{s_i}}{X_{s_i}} \frac{\sin Y_{s_i}}{Y_{s_i}} \exp\left\{ i\omega \frac{\xi_{0_i1}}{V_{r1}} + i\omega \frac{\xi_{0_i2}}{V_{r2}} \right\} \right] \qquad (2.16)$$

with

$$Xs_i = \frac{\omega L}{2V_s N_s}\left(\frac{V_s}{V_{r_1}} - r_{0_i1}\right), \qquad Ys_i = \frac{\omega W}{2V_s N_s}\left(\frac{V_s}{V_{r_2}} - r_{0_i2}\right). \qquad (2.17)$$

2.4.2 Fault Model and Velocity Structure Models

I apply CM in the waveform inversion for the source process of the 1995 Hyogo-ken Nanbu earthquake. I use the same fault plane model as that in Sekiguchi et al. (1998) (Fig.2.8) considering the surface rupture trace of the Nojima fault, the distribution of aftershocks occurring within 18 hours after the earthquake (Nemoto et al., 1996), the static displacement determined from triangulation (Hahimoto et al. 1996), SAR (Synthetic Aparture Rader) interferograms (Murakami et al., 1995), and the particle motion rotations observed very close to the causative fault (Sekiguchi et al., 1996). The fault plane is descretized into 310 subfaults, each of them has 2.05km length and

2.05km width. For this size of subfault, the critical hypocenter distance of 10% misfit is about 13.5km. Most of station-subfault pairs have larger hypocenter distances than the critical hypocenter distance, and for such pairs only one Green's function on a subfault is enough to well approximate the responses at the station to distributed slips over the subfault. For the station-subfault pairs with smaller distances than the critical hypodenter distance, subdivision of the subfaults is required. Figure 2.9 shows how the subfaults should be divided for calculating moving-dislocation element source waveforms at KBU station in order to hold down the plane wave approximation error within 10% in misfit. The rupture propagation velocity vectors to be convolved with each Green's function were calculated from the source model of Sekiguchi et al.(1998), assuming that the rupture arrival at each subfault is the time when the moment release exceeded 10% of the total moment release (Fig.2.10).

The figure 2.11 shows the element source waveforms from the subfaults at 2km depth calculated for KBU station, with and without moving dislocation effect. The waveforms with rupture propagation toward the station have narrower pulse and drastically larger amplitudes than those with rupture propagation against the station. Such differences are not seen in the element source waveforms without considering rupture propagation inside each subfault.

2.4.3 The Waveform Inversion

The multi-time window linear waveform inversion methodology (Hartzell and Heaton, 1983) is applied to estimate the source process. The moment release spatio-temporal distribution is represented by a set of element sources descretized in space and in time. As already mentioned, the model fault plane is divided into 2.05km square subfaults located at 2.05km intervals in strike and dipping directions. The moment release at any point on the model fault plane is represented by the successively activated smoothed ramp functions, each of which have a unit duration of 0.6 s at 0.4 s time intervals. The time windows therefore partially overlap each other. The triggering time of the first time window assigned to each subfault is calculated from the source model of Sekiguchi et al. (1998) (Fig.2.10). As this inverse problem includes underdetermined model parameters, I impose two constraints; one for restricting rake angle variation range and one to smooth out moment release vectors among adjacent model parameters with a strength proportional to inverse of a distance between model parameters in spatio-temporal domain (Sekiguchi et al., 1998).

2.4.3 Inversion Results

Figures 2.12(b) and 13 show the time progression of moment release on the model fault plane and comparison between synthesized waveforms using the inverted weights and observed waveforms. General features of the moment release distribution obtained using the element source waveforms without the finite moving dislocation effect (Fig. 2.12(a), after Sekiguchi et al., 1998) and with moving dislocation effect (Fig.2.12(b)) are similar each other; areas of relatively large moment release (subevents) at shallow part on the segment A, around the rupture starting point on the segment B, at deep part on the segment C, a subevent smaller than the previous three at deep

part on the segment E. But the places where the peak of the moment release appears in each subevent area are different.

Figure 2.14(a) shows the slip velocity time function obtained for each subfault. Long duration and high slip velocity at shallow part of the segment A catch our eyes. The distribution of rise time is shown in figure 2.14(b). Here, I define that a time duration where the slip velocity exceed 10% of maximum value over the model fault planes is "rise time" on a corresponding subfault. The rise time varies a lot spatially, up to around 3.5s. No remarkable depth dependence was found for the rise time.

2.5 NEAR-SOURCE GROUND MOTION SIMULATION USING 3-D FINITE DIFFERENCE METHOD

Using the inverted source process as an input, I simulated the near-source ground motions using 3-D finite difference method (3-D FDM) to examine the effect of continuous rupture to the near-source ground motion simulation. The model space for 3D FD calculation is the same as what used in Part I (Fig.1.19). The inverted source process has a continuous moment release distribution. On the other hand, the model space for the FD calculation is represented by discrete grids. Then I have to discretize the continuous moment distribution and distribute them to the FD grids. To consider how to discretize the continuous moment distribution, I go back to (2.7). If I divide the surface integral into *Ns* x *Ns* equal areas, as,

$$U_n(\mathbf{x},t)=\sum_{i=1}^{Ns^2}\sum_{p=\xi_1,\xi_2}\left\{\iint_{\Sigma_i} m_{0\xi_3}\left(0,0,\tau-\frac{\xi_1}{Vr1}-\frac{\xi_2}{Vr2}\right)*G_{np,\xi_3}\left(\mathbf{x},t-\frac{1}{Vs}\left(\frac{\xi_1 x_1}{R}+\frac{\xi_2 x_2}{R}\right);0,0,\tau\right)d\xi d_1\xi_2\right\} \quad (2.17)$$

and take Fourier transformation of the both sides of the above equation, I get,

$$U_n(\mathbf{x},\omega)=\sum_{i=1}^{Ns^2}\sum_{p=\xi_1,\xi_2}\left[m_{0\xi_3}(0,0,\omega)*G_{np,\xi_3}(0,0,\omega)\frac{LW}{Ns^2}\frac{\sin Xs_i}{Xs_i}\frac{\sin Ys_i}{Ys_i}\exp\left\{i2Xs_i\frac{\xi_{0_i1}}{L}+i2Ys_i\frac{\xi_{0_i2}}{W}\right\}\right] \quad (2.18)$$

X_{si} and Y_{si} are the same as (2.16). This equation shows that in order to get a displacement field completely equivalent to (2.7) I need to convolve the finite moving dislocation function with the convolution products of the slip time function and the Green's function in each piece, and sum them up. But I cannot convolve the moving dislocation function with the slip time functions in FD calculation. Because this function is defined for a certain subfault-station pair, and on the other hand, displacement field in the whole 3-D media is calculated all together without considering subevent –station pair in 3-D FD calculation. Then I divide the subfaults into enough small pieces because the accuracy of numerical integration increases as the discretization interval become small. I have found that the point source interval of about 400m (5 x 5 point sources on a 2km x 2km subfault) is enough to well realize the directivity effect in the frequency range of our present study.

I discretize the subfaults into 5 x 5 point sources, which is possible for FD grid interval of our model is smaller (120m). Instead of convolving the moving dislocation function, I change the duration of the element time function to include the rupture propagation time inside each piece, just as I did in SM in the numerical tests for examining applicability condition of CM.

Peak ground velocity distribution simulated is shown in Fig.2.15. Characteristic distribution of ground motion in the near-source region indicated by the damage distribution (lowermost of Fig.2.15) is well reproduced by modeling of both source process and wave propagation in the realistic 3-D velocity structure. Smoother distribution of the ground motion is obtained compared to that obtained by the source model with the sparsely distributed point sources (Fig.1.20(a)).

The spectrum of synthesized waveforms by FDM at rock sites in Awaji island and Kobe are compared (Fig.2.16). Sites are at almost the same distance from the surface trace of the causative faults (indicated by dots in the figure of the horizontal peak ground velocity distribution in Fig.2.15). Information in the frequency range of the source inversion analysis and the 3-D FDM calculation; 0.1 to 1.0 Hz, is reliable. Although slips with relatively long rise time were observed in the shallow part of the segment A (Fig. 2.14(a)), the simulated ground velocities on the Awaji island are not richer in lower frequency than those in Kobe. The horizontal component of the spectrum ratio of Awaji synthetics to Kobe synthetics demonstrates that the input level of ground motion is slightly lower on Awaji island than in Kobe in the range 0.1 to 0.5 Hz and nearly the same in the range 0.5 to 1.0 Hz. The frequencies effective for the damage generation in Kobe area is estimated around 1.0 Hz. Considering this point, I can say that the input ground motion around the damage generating frequencies were in comparable level in the two areas. What caused the drastic difference of damage levels between these two areas is, then, estimated to be the difference in geological circumstances in Awaji island and Kobe; almost no coverage of sediment on Awaji island and on the contrary, steep basin edge and thick sediment in Kobe area.

2.6 CONCLUSIONS

I introduced a convolution method (Ben-Menahem, 1961) which incorporate the effect of a moving dislocation over a finite area with a point source synthetic waveform in the calculation of element source waveforms used in the waveform inversion for earthquake rupture process. Each of such element source waves includes the effect of rupture directivity itself. Therefore, the rupture directivity effect on the entire fault area is fully considered in the waveform inversion.

The inverted rupture process by this method has a smooth slip distribution even inside the subfaults. Obtained moment release history for each subfault directly reflects a slip time function on the subfault because the rupture propagation effect inside each subfault is separated. Near-source ground motion simulation using the source model obtained by this method escapes from the problem of artificial, and large ground motion near the point sources due to the use of sparsely distributed point sources.

CM surpasses SM in amount of computation. SM requires calculation of many Green's functions to do surface integration numerically. On the other hand, only one or several Green's

functions' calculation is needed for one subfault in CM because the surface integration is done analytically.

Applicability and limitation of CM was tested numerically. CM is based on the plane wave approximation. I examined the variation of the error arising from the plane wave approximation, due to subfault size, hypocenter distance, rupture propagation velocity and found that a ratio of right and left sides of the Fraunhofer inequality condition required for the plane wave approximation is a useful index to estimate the error of CM. Using this index, I can evaluate the maximum error level caused by CM for given source size, hypocenter distance, faulting mechanism, and rupture velocity.

I applied CM in the waveform inversion for the source process of the 1995 Hyogo-ken Nanbu earthquake. The overall characteristics of the moment release distributions are similar between two inversion results; one inverted with point source element waveforms and the other with element source waves considering the finite moving dislocation effects inside each subfault. But details like places of peak moment releases differ between these inversion results. I found that the rise time varies a lot spatially, without remarkable dependency on depth.

Using the inverted source process for the Hyogo-ken Nanbu earthquake as input, I simulated the near-source ground motions using 3-dimensional finite difference method to examine the effect of continuous rupture to the near-source ground motion simulation. Characteristic distribution of ground motion in the near-source region indicated by the damage distribution is well reproduced by modeling of both source process and wave propagation in the realistic 3-D velocity structure. Smoother distribution of the ground motion is obtained compared to that obtained by the source model with the sparsely distributed point sources. Comparing the synthetic spectra at rock sites in Awaji Island and Kobe, I found that the input ground motion at frequencies most effective to the damage generation was in comparable level, in spite of the large and shallow slip in the Awaji side.

This thesis is based on the following papers;

1. Fault geometry in the rupture termination of the 1995 Hyogo-ken Nanbu earthquake,
being planed to be submitted to Geophysical Journal International,
by authors, Haruko Sekiguchi, Kojiro Irikura, and Tomotaka Iwata.

2. Source Inversion for Estimating Continuous Slip Distribution on the Fault - Introduction of Green's Functions Convolved with a Correction Function to give Moving Dislocation Effects in Subfaults -
being planed to be submitted to Geophysical Journal International,
by authors, Haruko Sekiguchi, Kojiro Irikura, and Tomotaka Iwata.

3. REFERENCES

Akaike, H., Likelihood and the Bayes procedure, in *Bayesian Statics*, J. M. Bernardo, M. H. DeGroot, D. V. Lindley, and A. F. M. Smith (Editors), University Press, Valencia, Spain, 143-166, 1980.

Aki, K., Seismic Displacements near a Fault, J. Geophys. Res., 73, 16, 1968.

Aki, K. and Richards, Quantitative Seismology, W. H. Freeman and Co., 1980

Ben-Menahem, A., Radiation of seismic surface-waves from finite moving sources, Bull. Seism. Soc. Am., 51, 3, 401-435, 1961.

Bouchon, M., A simple method to calculate Green's function for elastic layered media, *Bull. Seism. Soc. Am.*, **71**, 959-971, 1981.

Furumura, T. and K. Koketsu, Specific distribution of ground motion during the 1995 Kobe earthquake and its generation mechanism, *Geophys. Res. Lett.*, **25**, 785-788, 1998.

Hartzell, S. H. and T. H. Heaton, Inversion of strong ground motion and teleseismic waveform data for the fault rupture history of the 1979 Imperial Valley, California, earthquake, *Bull. Seism. Soc. Am.*, **73**, 1553-1583, 1983.

Hashimoto, M., T. Sagiya, H. Tsuji, Y. Hatanaka, and T. Tada, Coseismic displacements of the 1995 Kobe earthquake, *J. Phys. Earth*, **44**, 255-279, 1996.

Horikawa, H., K. Hirahara, Y. Umeda, M. Hashimoto, F. Kusano, Simultaneous inversion of geodetic and strong motion data for the source process of the Hyogo-ken Nanbu, Japan, earthquake, *J. Phys. Earth*, **44**, 455-471, 1996.

Huzita, K., On survey results of active faults in Osaka-Kobe area, Proc. 9th seminar on studying active faults 'On deep structure of Osaka-bay area', 1-10, June, 1996 (in Japanese).

Ide, S., M. Takeo and Y. Yoshida, Source process of the 1995 Kobe earthquake: Determination of spatio-temporal slip distribution by Bayesian Modeling, *Bull. Seism. Soc. Am.*, **86**, 547-566, 1996.

Ishihara, M., S. Yoshikawa, M. Mitamura, K. Mizuno and T. Hayashi, 1:125,000 "Quaternary Geological Map of Osaka and Adjacent Areas, Kinki, Japan", *Urban Kubota*, No.30, 1991 (in Japanese).

Kagawa, T., S. Sawada, Y. Iwasaki and A. Nanjo, Modeling of the deep underground structures of the Osaka basin, *Proc. 22th JSCE Earthq. Eng. Symp.*, 199-202, 1993 (in Japanese).

Kagawa, T., K. Irikura and I. Yokoi, Restoring clipped records of the near field strong ground motion during the 1995 Hyogo-ken Nanbu (Kobe), Japan, earthquake, *J. Natural Disas. Sci.*, **18-1**, 43-57, 1996.

Kame, N. and T. Yamashita, Why do small earthquakes occur more frequently than larger ones ? - Earthquake faulting can stop by itself -, *Science Journal KAGAKU*, 68, 702-709, 1998 (in Japanese).

Kawase, H., The cause of the damage belt in Kobe: "The basin-edge-induced diffracted Rayleigh waves", *Seism. Res. Lett.*, **67**, 25-34, 1996.

Kennett, B. L. N. and N. J. Kerry, Seismic waves in a stratified half-space, *Geophys. J. R. astr. Soc.*, **57**, 557-583, 1979.

Kobe City and Institute of Construction Engineering, Hanshin-Awaji earthquake disaster, and geology and active faults in Kobe, Kobe City, Kobe, 1998.

Koketsu, K. An overview of the rupture process, Report on the Hanshin-Awaji Earthquake Disaster, Common Series 2, Maruzen, Tokyo, 168-175, 1998 (in Japanese).

Motosaka, M. and M. Nagano, Analysis of amplification characteristics of ground motions in Kobe City taking account of deep irregular underground structure, - Interpretation of heavily damaged belt zone during the 1995 Hyogo-ken Nanbu earthquake-, *J. Struct. Constr. Eng., AIJ,* **488**, 39-48, 1996.

Moya, C. A., and K. Irikura, Seismic attenuation, kappa and site response in the Osaka area, Japan, submitted to *Bull. Seism. Soc. Am.*, 1998.

Murakami, M., S. Fujiwara, and T. Saito, Detection of Crustal Deformations associated with 1995 Hyogoken-Nanbu earthquake by interferometric SAR, Current News of Geophysical Survey Institute of Japan, No.83, 24-27, 1995.

Nakamura, Y., F. Uehan, and H. Inoue, Waveform and its analysis of the 1995 Hyogo-ken Nanbu earthquake (II), JR Earthquake Information No. 23d, Railway Technical Research Institute, March 1996 (in Japanese).

Nemoto, H., H. Katao, E. Suzuki, Y. Yoshida, and K. Irikura, The spreading of aftershocks area directly after the 1995 Hyogo-ken Nanbu earthquake, *Programme and Abstracts of Seism. Soc. Japan 1996 No.2*, 1996 (in Japanese).

Nemoto, H., H. Negishi, and K. Irikura, Re-examination of the hypocenter of the Hyogo-ken Nanbu earthquake, *Zisin* (J. Seism. Soc. Japan), **50**, 125-129, 1997 (in Japanese).

Ozawa, S., M. Murakami, S. Fujiwara, and M. Tobita, Synthetic aperture radar interferogram of the 1995 Kobe earthquake and its geodetic inversion, *Geophys. Res. Lett.*, **24**, 2327-2330, 1997.

Pitarka, A., K. Irikura, T. Iwata, and H. Sekiguchi, Three-dimensional simulation of the near-fault ground motion for the 1995 Hyogo-ken Nanbu (Kobe), Japan, earthquake, *Bull. Seism. Soc. Am.* **88**, 428-440, 1998.

Public Works Research Institute, Ministry of Construction, Strong-Motion Acceleration Records from Public Works in Japan (No. 21), Technical note of public works research institute, 64, Public Works Research Institute, Ministry of Construction, 265pp, Tsukuba, 1995.

Sato, R., Formulations of solutions for earthquake source models and some related problems, J. Phys. Earth, 17, 2, 1969.

Sekiguchi, H., K. Irikura, T. Iwata, Y. Kakehi and M. Hoshiba, Determination of the location of faulting beneath Kobe during the 1995 Hyogo-ken Nanbu, Japan, earthquake from near-source particle motion, *Geophys. Res. Lett.*, **23**, 387-390, 1996a.

Sekiguchi, H., K. Irikura, T. Iwata, Y. Kakehi and M. Hoshiba, Minute locating of fault planes and source process of the 1995 Hyogo-ken Nanbu, Japan, earthquake from the waveform inversion of strong ground motion, *J. Phys. Earth*, **44**, 473-487, 1996b.

Sekiguchi, H., K. Irikura and T. Iwata, Fault Geometry in the Rupture Termination of the 1995 Hyogo-ken Nanbu Earthquake, in preparation for submitting to *Geophys. J. Inter*, 1998.

Somerville, P., N. F. Smith, R. W. Graves and N. A. Abrahamson, Modification of empirical strong ground motion attenuation relations to include the amplitude and duration effects of rupture directivity, *Seism. Res. Lett.*, **68**, 199-222, 1997.

Wald, D. J., Slip history of the 1995 Kobe, Japan, Earthquake determined from strong motion, teleseismic, and geodetic data, *J. Phys. Earth*, **44**, 489-503, 1996.

Wessel, P. and W. H. F. Smith, Free software helps map and display data, *EOS Trans Amer. Geophys. U.*, **72**, 441, 445-446, 1991.

Yoshida, S., K. Koketsu, B. Shibazaki, T. Sagiya, and Y. Yoshida, Joint inversion of near- and far-field waveforms and geodetic data for the rupture process of the 1995 Kobe earthquake, *J. Phys. Earth*, **44**, 437-454, 1996.

Yoshida, S., Waveform inversion using ABIC for the rupture process of the 1983 Hindu Kush earthquake, *Phys. Earth Planet. Inter.*, **56**, 389-405, 1989.

4. TABLES

5. FIGURES

Figure 1.1 "Damage belt" in Kobe area is indicated by light gray zone. The digitized "damage belt" location data by Koketsu (1997). Dark gray lines show the active fault traces from Ishihara et al. (1991). Circles are epicenters of aftershocks since just after till 18 hours after the mainshock determined by Nemoto et al. (1996).

Figure 1.2 Section view of aftershock hypocenter distribution (Nemoto et al., 1996). (upper) Section view along a plane nearly parallel to the causative faults' striks. (lower left) Section view on a surface normal to the strike of the fault segment southwest of the hypocenter (Nojima Fault). (lower right) Section view on a surface normal to the strike of the segments northeast of the hypocenter. Star indicates the hypocenter location.

Figure 1.3 (left) SAR (Synthetic Aperture Radar) interferogram made by comparing two SAR imagery observed before and after the Hyogo-ken Nanbu earthquake (Murakami et al., 1995). Detected crustal deformation by SAR interferometry represents the ground displacements parallel to the satellite line of site. (right) Active fault systems in the source region of the Hyogo-ken Nanbu earthquake (Ishihara et al., 1991). The area and scale of this map is the same as that in the right hand side. Dense fringes are observed along main stream of the estimated causative faults; Nojima, Suwayama, Suma and Gosukebashi faults. Some irregular fringes are identified around the surface trace of the Okamoto fault. (See figure 1.1 for names of the active faults.)

Figure 1.4 Snap shots of spontaneous rupture growth with no constraints on the crack geometry (Kame and Yamashita, 1998). Coulomb's frictional force is assumed to act on the rupturing surface through the calculation.

Figure 1.5 Sequence of Analysis.

Figure 1.6 Schematic explanation of source representation and parameterization.

Figure 1.7 Fault plane model (with segments A, B, C, D and E). Gray lines show the active fault traces from Ishihara et al. (1991). Vectors show static displacement during 1984 and 1995 after the earthquake determined by Hashimoto et al.(1996) using GPS data. Epicenters of the mainshock and aftershock during the day of the mainshock occurrence are determined by Nemoto et al. (1996, 1997). Circles are epicenters of aftershocks since just after till 18 hours after the mainshock. Fault plane model with segments A, B, C, D and D' is a reference model to examine the effect of segment E.

Figure 1.8 Model space for 3-D FDM wavefield simulation to investigate the applicability of 1-D approximation of 3-D velocity structure. A part of a basin is modeled and its edge goes along the Y-axis. The thickness of the sediments is constantly 1.8 km, which is the typical value estimated in the shoreline in Kobe area. A point source was located 0.5 km away from the edge to the hard rock region and at a certain depth. Ry is the distance from the source to a site along Y-axis. Waveforms were calculated over the shaded area. Simulation was done also with a flat layer model having a flat sediment layer with the same thickness and material parameters.

Figures 1.9 Waveforms generated from a source at 10km depth for sites at Ry=12km in the model space shown in Fig. 1.8. Solid lines are synthetic waveforms for the basin edge structure, and dashed lines are for the flat layer structure. FN and FP correspond to X- and Y-axis directions in figure 1.8. Cross mark (x) indicates the time when the difference of the two waveforms exceeds 20 % of the maximum amplitude of the two traces. Vertical measure indicates the distance from the basin edge to sites.

Figure 1.10 Waveforms generated from sources at various Ry and Zs in the model space shown in Fig. 1.8 at a site at 5km distance from the basin edge.

Figure 1.11 25 stations used in the waveform inversion. Organization of each record are listed in Table 1.3

Figure 1.12 (left) Six different inversion results with identical fault model, data set, Green's functions, and rake angle variation constraint, and with different smoothing strengths. (right) Variation of ABIC, misfit and total moment due to the smoothing constraint strength λ.

Figure 1.13 Time progression of rupture illustrated in terms of moment release density at 1s intervals.

Figure 1.14 Observed velocity waveforms (solid lines) and synthetics (dashed lines).

Figure 1.15 Observed (bold line) and synthetic (thin line) waveforms at KBU station. From the top trace, observation, synthetics from all 5 segments (ABCDE), synthetics from segment A, B, C, D and E, respectively.

Figure 1.16 Final moment release distribution (a) for the ABCDE fault model with segments A, B, C, D and E, and (b) for the ABCDD' fault model, respectively.

Figure 1.17 Distribution of final moment release and slip of the assumed and inverted source

models for the resolution check 2.

Figure 1.18 Distribution of final moment release and slip of the assumed and inverted source models for the resolution check 3.

Figure 1.19 Bird's eye view of the sediment-bedrock interface topography of the model space for 3-D FDM wave field modeling. The space stretches 58km in the direction of N58° E, 13.6km in in the direction of N148° E, and 23km in depth direction.

Figure 1.20 (a) Distribution of peak ground velocity simulated in the 3-D model space (figure 1.16) when whole moment release (inside the model space) is introduced. "Fault normal" component means the breadth direction of the map (N148° E) and "fault parallel" component means the length direction of the map (N58° E). (b) The same as (a) but when moment release on only the branched fault is assumed.

Figure 2.1 Schematic explanation of difference in rupture directivity effect expected to appear in the waveforms between caused by with and without considering rupture propagation inside each element source area.

Figure 2.2 Configuration of numerical tests for examining validity and limitation of CM. ξ_1 and ξ_3 directions correspond to north and east directions in the following figures (from fig.2.3 to fig.2.6), respectively.

Figure 2.3 Synthetic velocity waveforms using CM (solid lines) and SM (dashed lines) for half space velocity structure. All the synthetics are bandpass filtered in the range 0.1 – 1.0 Hz.

Figure 2.4 Compilation of numerical tests fixing hypocenter distance and subfault size, and varying rupture propagation velocity and direction, and takeoff angle (station location).

Figure. 2.5 Variation of approximation error (misfit) against hypocenter distance fixing rupture velocity, rupture propagation direction, takeoff angle, and subfault size to "worst set"; Vrup=0.5Vs, δ = 170 , station No. 33 (θ , ϕ) = (75, 85).

Figure 2.6 Variation of misfit against hypocenter distance fixing rupture velocity, rupture propagation direction, takeoff angle, and varying subfault size and hypocenter distance so that C_{fraun} value keeps constant.

Figure 2.7 Flow for calculation of element waveforms with finite moving dislocation effect for the waveform inversion.

Figure 2.8 Fault plane model for the waveform inversion for the source process of the 1995 Hyogo-ken Nanbu earthquake. Gray lines show the active fault traces from Ishihara et al. (1991). Vectors show static displacement during 1984 and 1995 after the earthquake determined by Hashimoto et al.(1996) using GPS data. Epicenters of the mainshock and aftershock during the day of the mainshock occurrence are determined by Nemoto et al. (1996, 1997). Circles are epicenters of aftershocks since just after till 18 hours after the mainshock.

Figure 2.9 Subdivision of subfaults in order to apply CM for computation of element source waveforms at KBU station keeping the approximation error less than 10%.

Figure 2.10 The rupture propagation velocity vectors to be convolved with the Green's functions were calculated from the source model of Sekiguchi et al.(1998), assuming that the rupture arrival at each subfault is the time when the moment release exceeded 10% of the total moment release (contour). The contour of rupture arrival time is drawn for every 1 second.

Figure 2.11 The element source waveforms from subfaults centered at 2km depth calculated for KBU station, with (solid lines) and without (dashed lines) moving dislocation effect.

Figure 2.12 Time progression of rupture in terms of moment release density; (a) using point source element waveforms (Sekiguchi et al., 1998), and (b) using element source waveforms from finite moving dislocation using CM.

Figure 2.13 Observed (solid lines) and synthesized (dashed lines) waveforms.

Figure 2.14 (a) The slip velocity time function on each subfault. (b) The spatial variation of rise time.

Figure 2.15 Distribution of peak ground velocity simulated in the 3-D model space (figure 1.16) using the source process shown in figure 2.12(b). "Fault normal" component means the breadth direction of the map (N148° E) and "fault parallel" component means the length direction of the map (N58° E).

Figure 2.16 (middle and bottom) Dashed lines are synthetic spectra at rock sites in Awaji Island

and Kobe (indicated by dots in the figure for the horizontal ground velocity distribution in figure 2.15). Solid lines are the average spectra at each area. (top) Spectral ratio of the Awaji island to Kobe. "Horizontal" means a vector summation of the horizontal two components.

Table 1.1

	active fault	strike(deg)	dip(deg)	length(km)
segment A	Nojima	45.0	78.0	20.5
segment B	Suma	50.0	90.0	14.35
segment C	Suwayama	233.0	82.0	10.25
segment D	Gosukebashi	218.0	82.0	12.3
segment E	Okamoto	268.0	82.0	6.15

Table 1.2

	Vp Km/s	Vs Km/s	ρ g/cm^3	Qp= Qs	Depth Km
Sediment 1	2.0	0.6	2.1	80	0.85 (inside basin)
Sediment 2	2.2	1.1	2.1	80	1.8 (inside basin)
1st rock	5.5	3.2	2.4	300	4.0
2nd rock	6.0	3.5	2.7	400	17.8
Half space	6.7	3.9	2.8	500	---

Table 1.3

Station	Lat.	Lon.	Organization
AMC	34.7180	135.4080	CEORKA
CHY	34.4390	135.6590	CEORKA
KBU	34.7250	135.2400	CEORKA
MOT	34.7250	135.2810	CEORKA
TDO	34.4800	135.4080	CEORKA
TOY	34.8010	135.5010	CEORKA
AID	34.940	134.168	JMA
AIO	33.792	134.452	JMA
AWA	34.336	134.908	JMA
HEG	34.653	135.685	JMA
KOB	34.69	135.18	JMA
KOY	34.218	135.593	JMA
MRT	33.2483	134.1800	JMA
OKA	34.6583	133.9183	JMA
OSA	34.6783	135.5217	JMA
WAC	35.283	135.402	JMA
NKY	34.9667	135.6222	Kansai Electric Power Co. Inc.
SOK	34.7431	135.4417	Kansai Electric Power Co. Inc.
KMT	34.383	135.35	RRI, Kyoto Univ.
ABU	34.8600	135.5735	RCEP DPRI, Kyoto Univ.
KN1	34.855	135.217	Matsumuragumi Co. Inc.
NRT	34.234	134.641	Honshu-Shikoku Bridge Public Corporation
TZK	34.8083	135.3437	Railway Technical Research Institute
RKI	34.6883	135.2728	Sekisui House Co. Inc.
KPI	34.670	135.208	Kobe City

Table 1.4

	Vp Km/s	Vs Km/s	ρ g/cm^3	Qp=Qs	Depth Km
Sediment 1	2.0	0.6	2.1	80	Irregular
Sediment 2	2.2	1.1	2.1	80	Irregular
1st rock	5.5	3.2	2.4	300	4.0
2nd rock	6.0	3.5	2.7	400	17.8
Half space	6.7	3.9	2.8	500	---

Table 2.1

C_{fraun}	0.05	0.1	0.2
Max. plane wave approximation error	21.0	13.6	9.8

Table 2.2

	active fault	strike(deg)	dip(deg)	length(km)
segment A	Nojima	45.0	78.0	20.5
segment B	Suma	50.0	90.0	14.35
segment C	Suwayama	233.0	82.0	10.25
segment D	Gosukebashi	218.0	82.0	12.3
segment E	Okamoto	268.0	82.0	6.15

Table 2.3

Station	Lat.	Lon.	Organization
AMC	34.7180	135.4080	CEORKA
CHY	34.4390	135.6590	CEORKA
KBU	34.7250	135.2400	CEORKA
MOT	34.7250	135.2810	CEORKA
TDO	34.4800	135.4080	CEORKA
TOY	34.8010	135.5010	CEORKA
AID	34.940	134.168	JMA
AIO	33.792	134.452	JMA
AWA	34.336	134.908	JMA
HEG	34.653	135.685	JMA
KOB	34.69	135.18	JMA
KOY	34.218	135.593	JMA
MRT	33.2483	134.1800	JMA
OKA	34.6583	133.9183	JMA
OSA	34.6783	135.5217	JMA
WAC	35.283	135.402	JMA
NKY	34.9667	135.6222	Kansai Electric Power Co. Inc.
SOK	34.7431	135.4417	Kansai Electric Power Co. Inc.
KMT	34.383	135.35	RRI, Kyoto Univ.
ABU	34.8600	135.5735	RCEP DPRI, Kyoto Univ.
KN1	34.855	135.217	Matsumuragumi Co. Inc.
NRT	34.234	134.641	Honshu-Shikoku Bridge Public Corporation
TZK	34.8083	135.3437	Railway Technical Research Institute
RKI	34.6883	135.2728	Sekisui House Co. Inc.
KPI	34.670	135.208	Kobe City

Table 2.4

	By element wave without considering rupture propagation	By element wave considering rupture propagation
total	329.	408.
A	131.	170.
B	65.	83.
C	53.	62.
D	50.	64.
E	30.	29.

(10^{17}Nm)

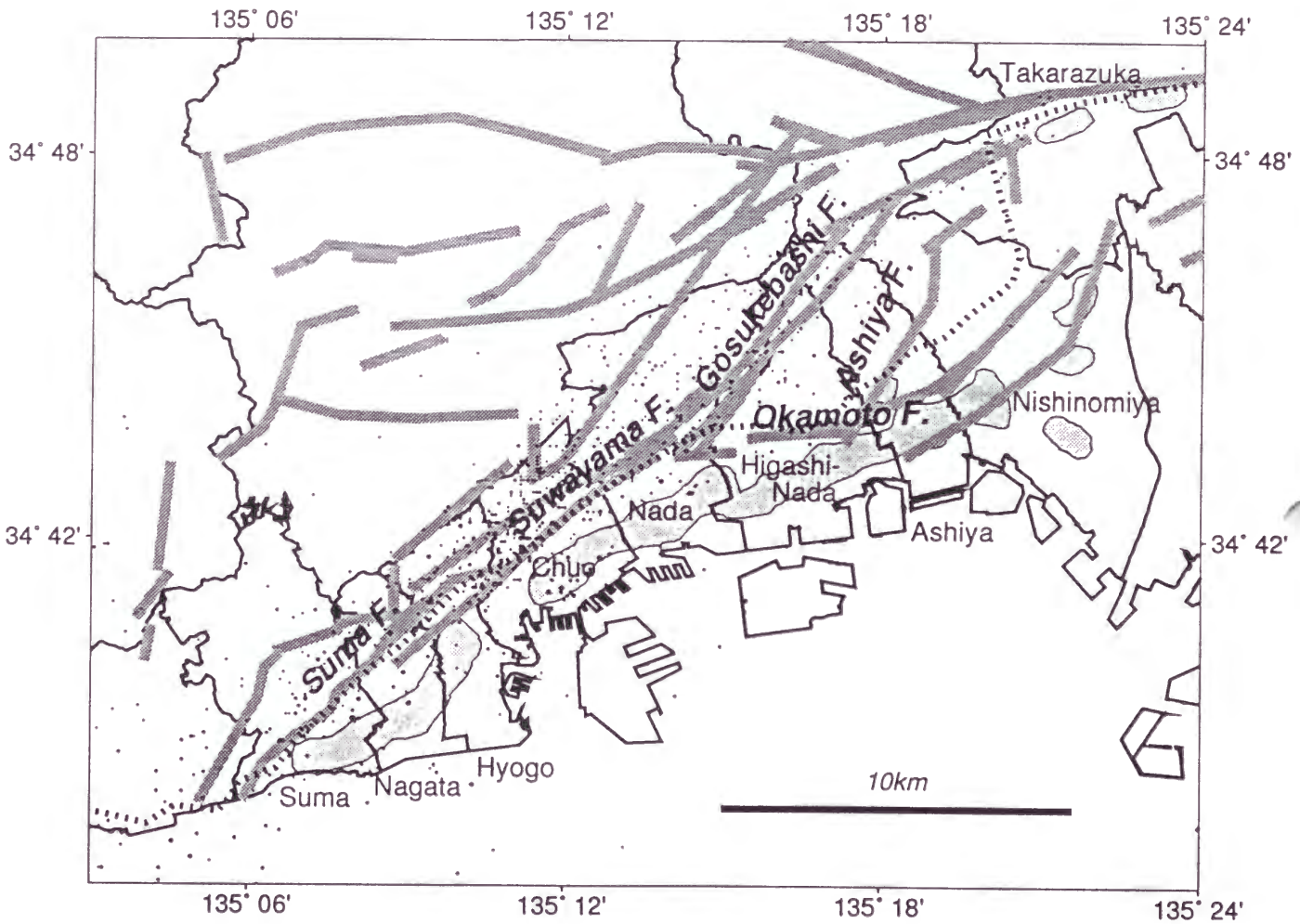
135° 06'
135° 12'
135° 18'
135° 24'
34° 48'
34° 42'
Takarazuka
Gosukebashi F.
Ashiya F.
Okamoto F.
Suwayama F.
Suma F.
Nishinomiya
Higashi-
Nada
Nada
Ashiya
Chuo
Hyogo
Nagata
Suma
10km

Figure 1.1

Section View of Aftershock Hypocenters

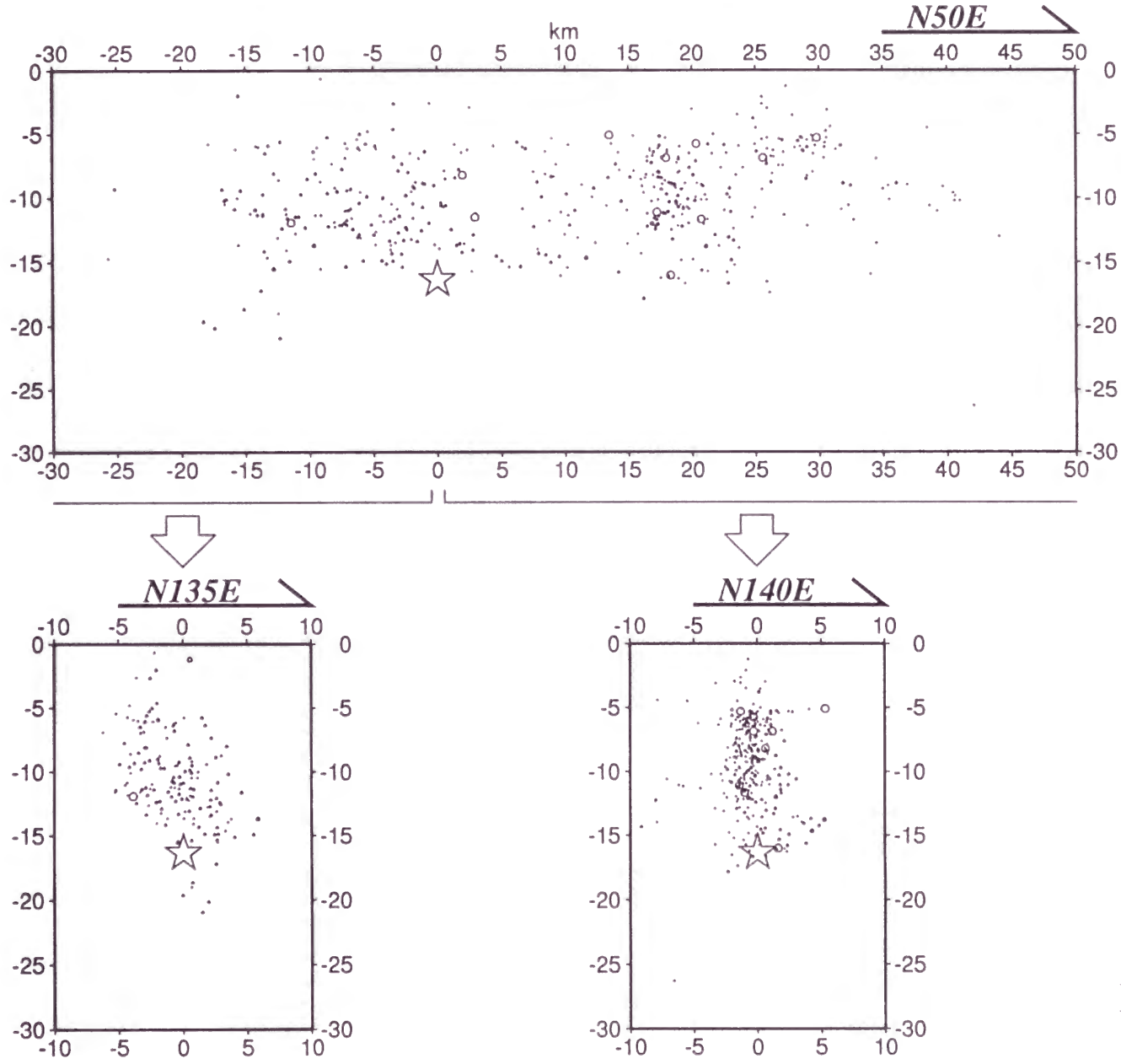

Figure 1.2

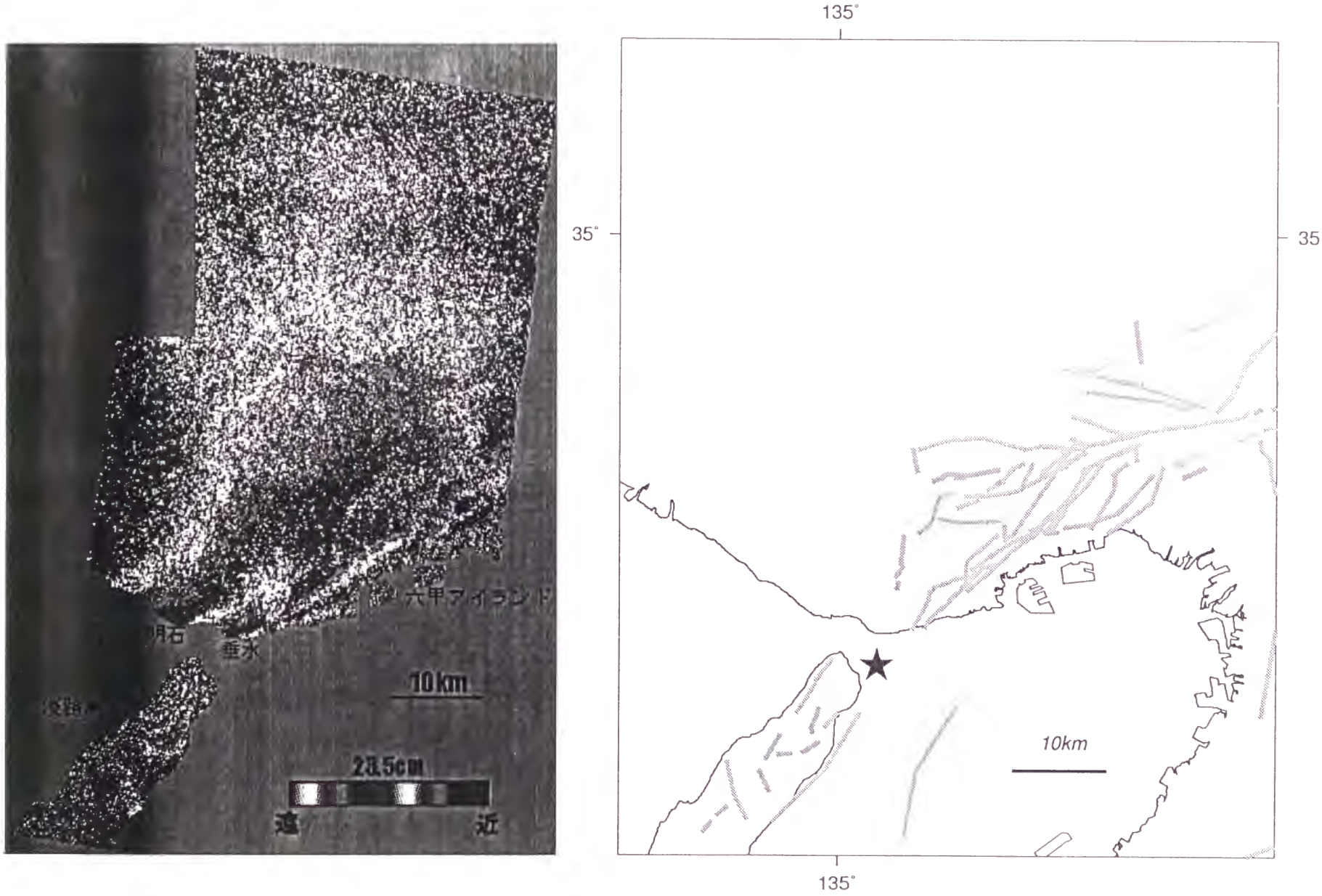

Figure 1.3

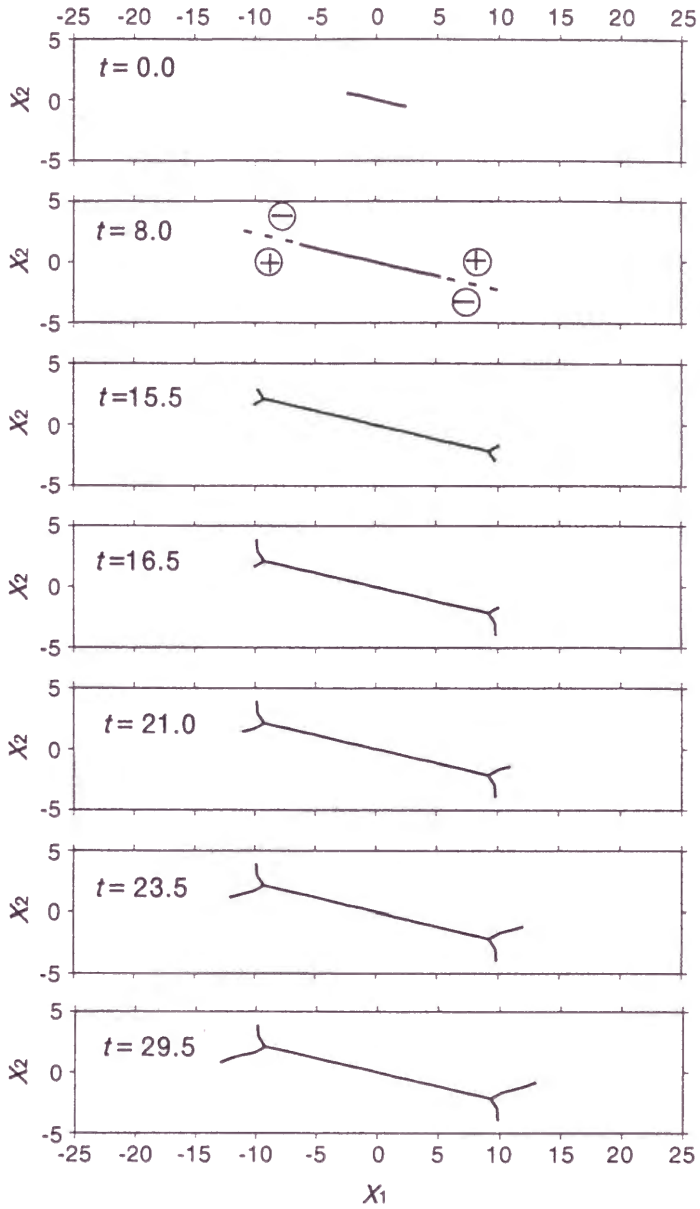
-25 -20 -15 -10 -5 0 5 10 15 20 25
t = 0.0
t = 8.0
t =15.5
t =16.5
t = 21.0
t = 23.5
t = 29.5
X2
X1
5
0
-5

Figure 1.4

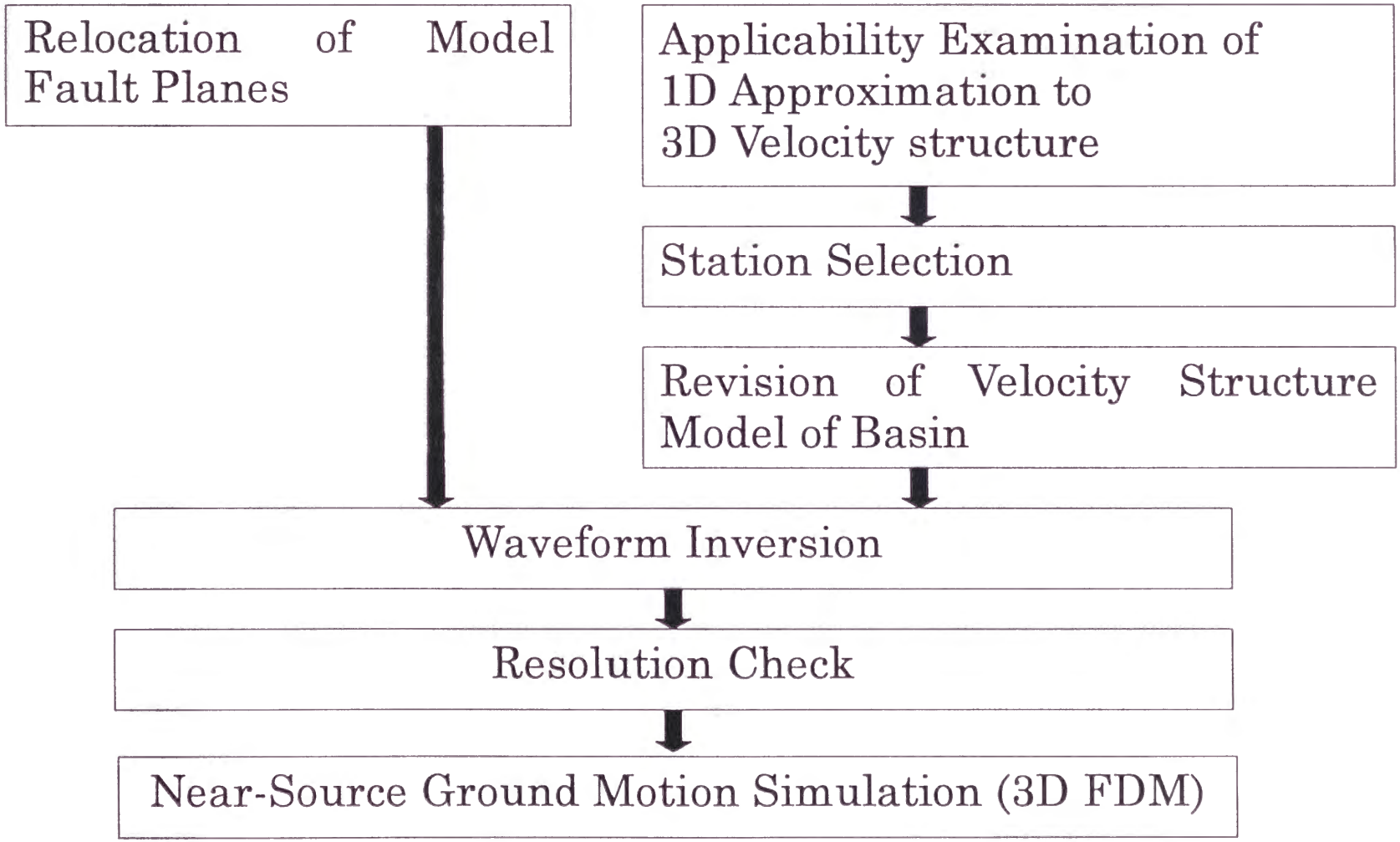
Relocation of Model Fault Planes
Applicability Examination of 1D Approximation to 3D Velocity structure
Station Selection
Revision of Velocity Structure Model of Basin
Waveform Inversion
Resolution Check
Near-Source Ground Motion Simulation (3D FDM)

Figure 1.5

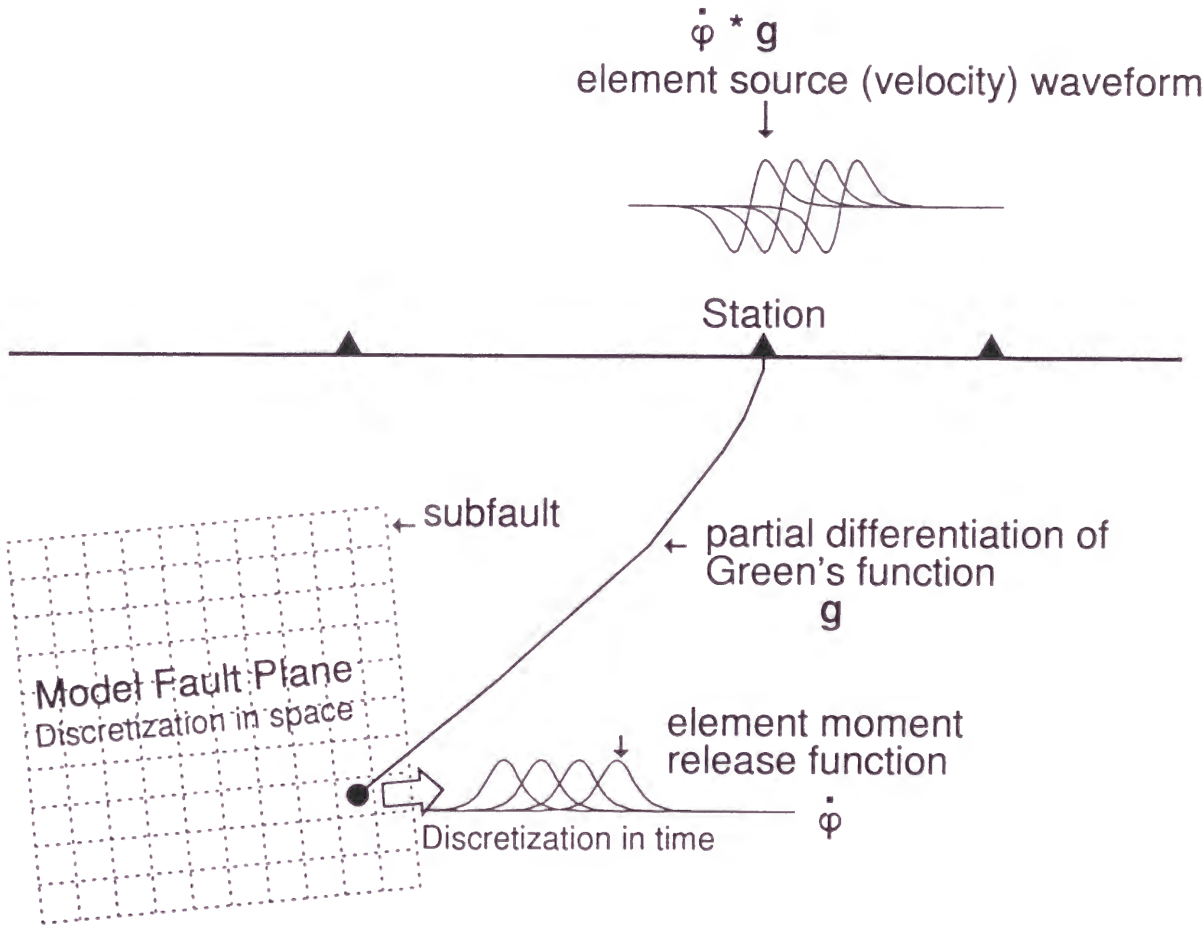
$\dot{\varphi} * g$
element source (velocity) waveform
Station
subfault
partial differentiation of
Green's function
g
Model Fault Plane
Discretization in space
element moment
release function
$\dot{\varphi}$
Discretization in time

Figure 1.6

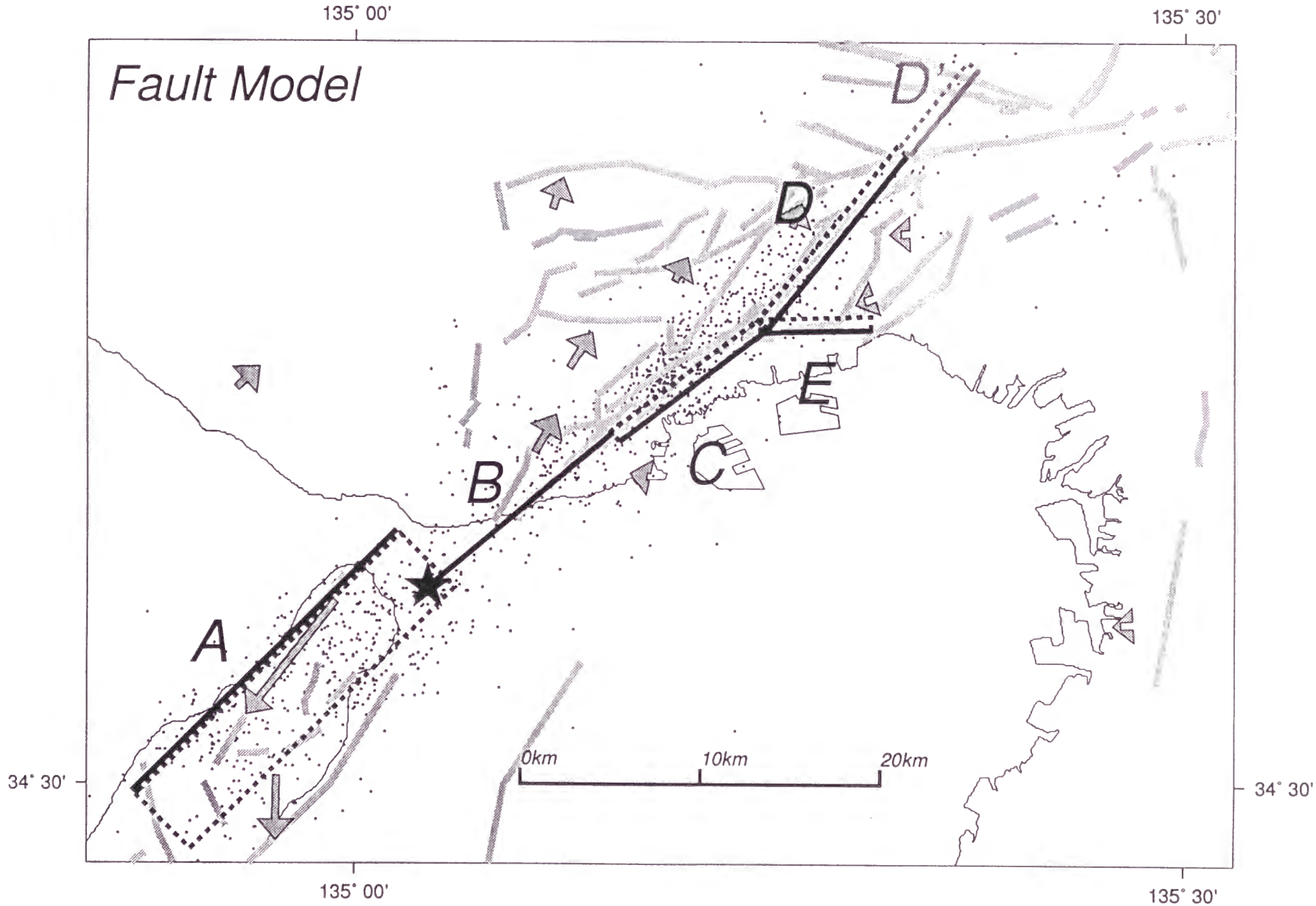

Figure 1.7

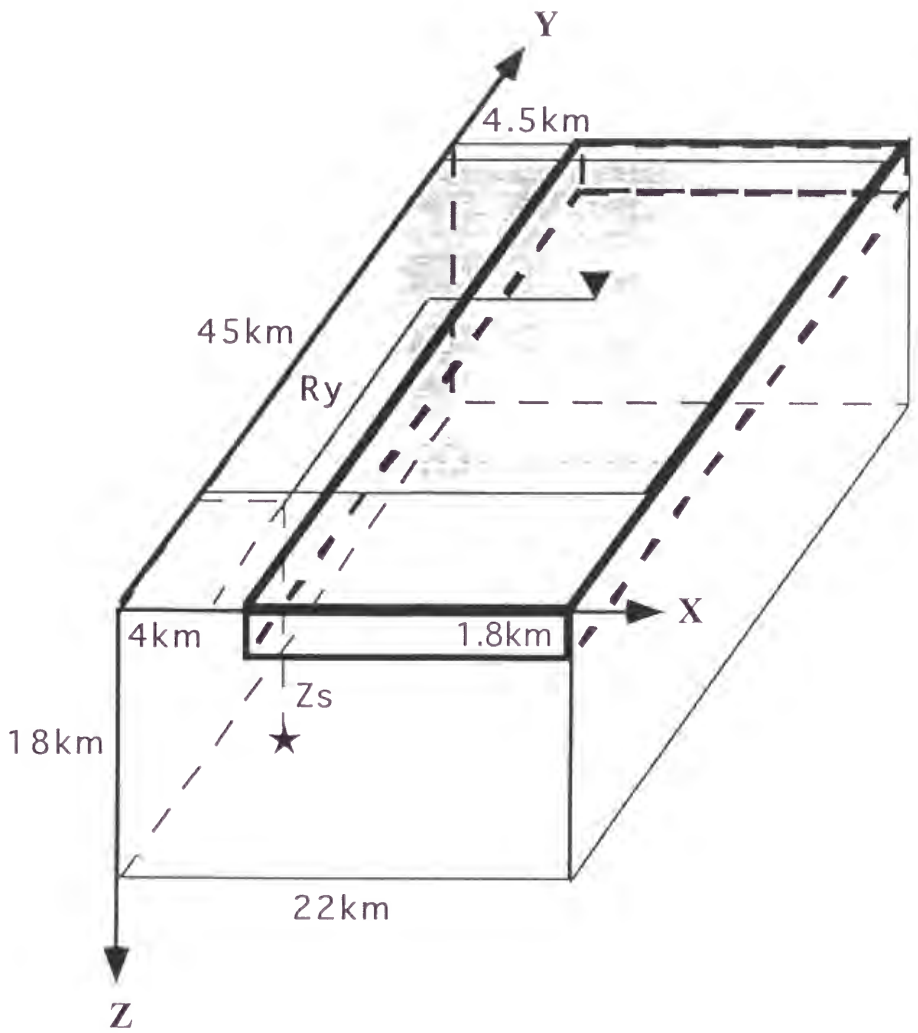

Figure 1.8

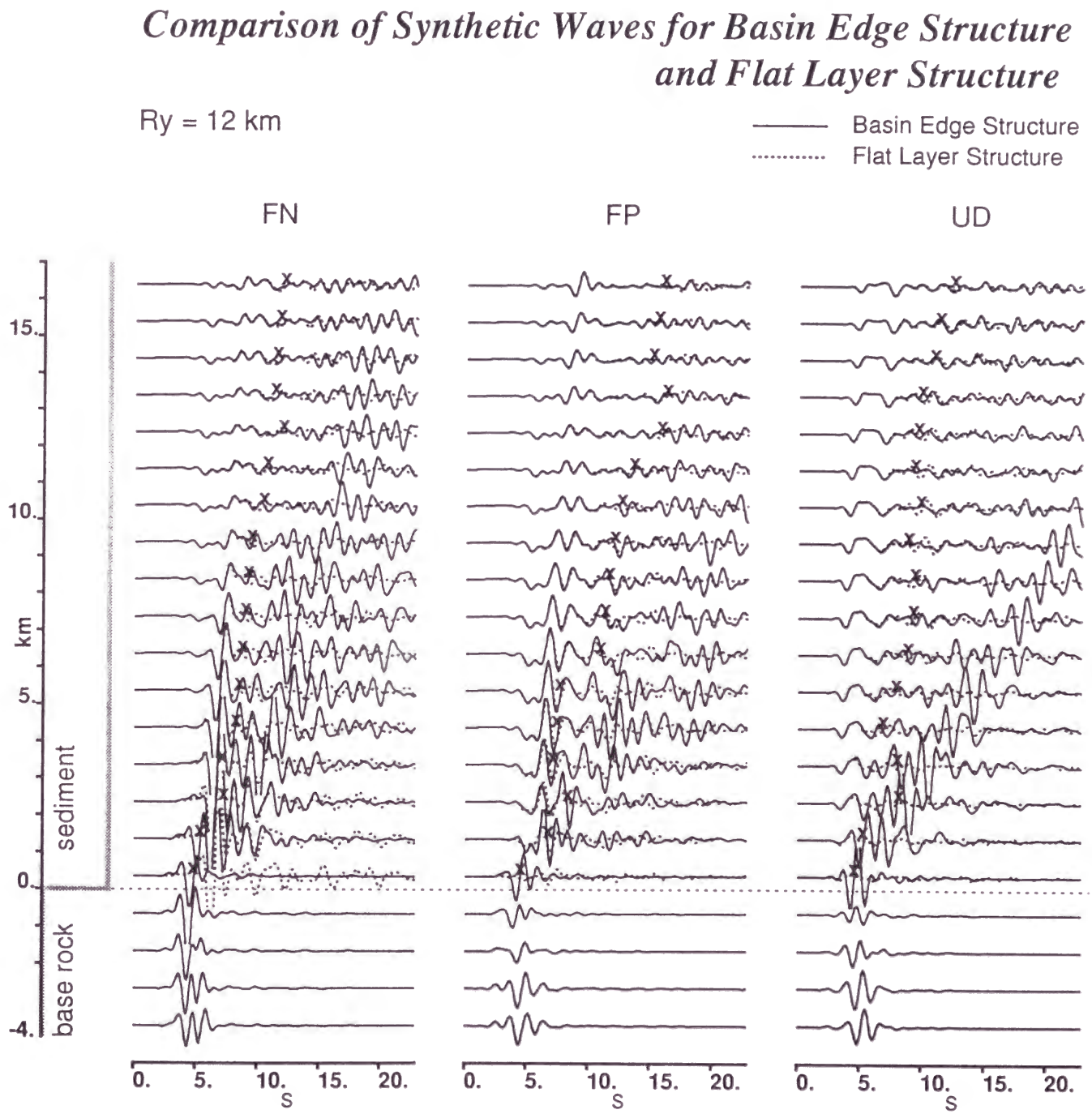
Comparison of Synthetic Waves for Basin Edge Structure and Flat Layer Structure
Ry = 12 km
Basin Edge Structure
Flat Layer Structure
FN
FP
UD
15.
10.
km
5.
0.
-4.
sediment
base rock
0.
5.
10.
15.
20.
s

Figure 1.9

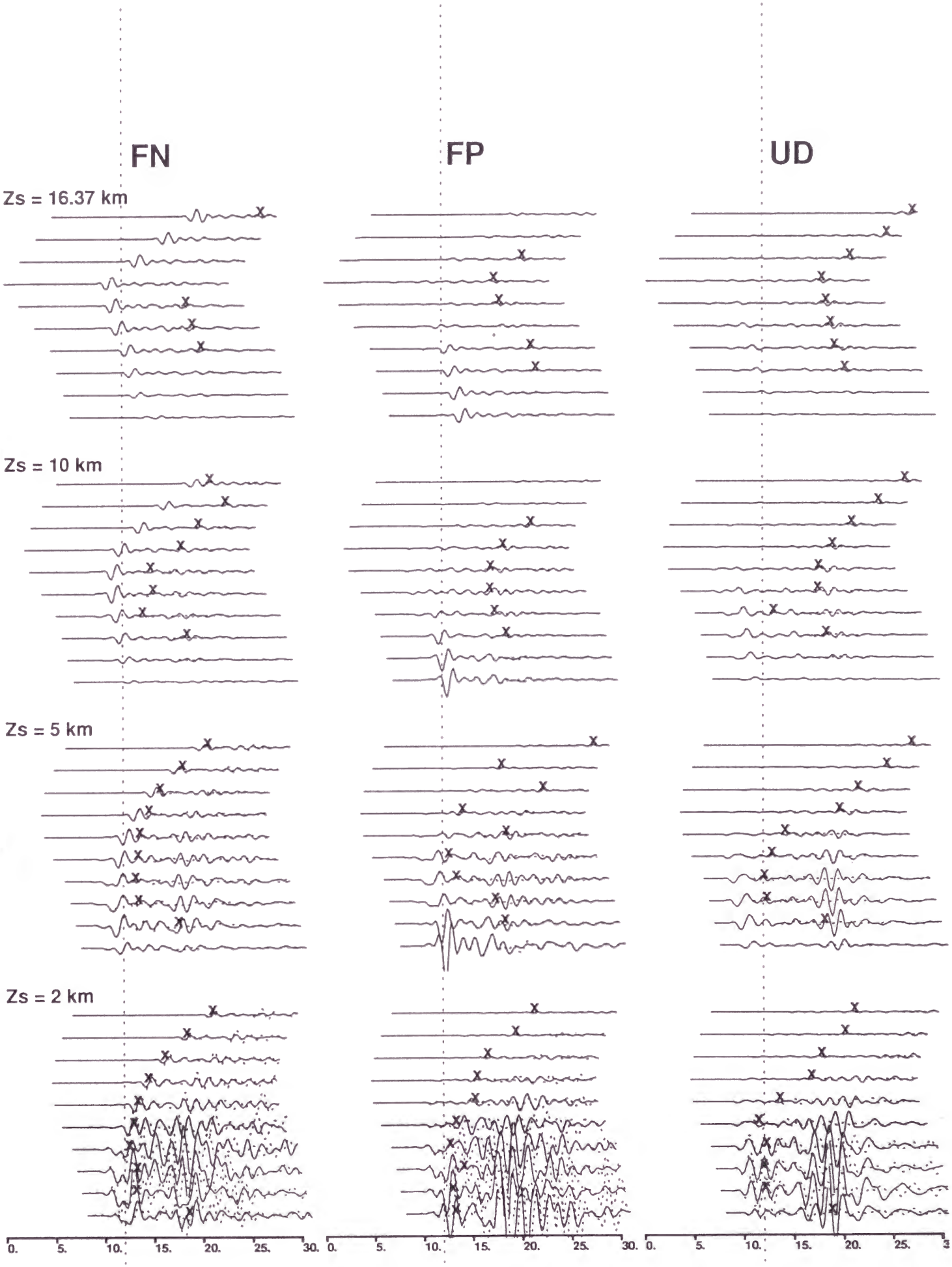

Figure 1.10

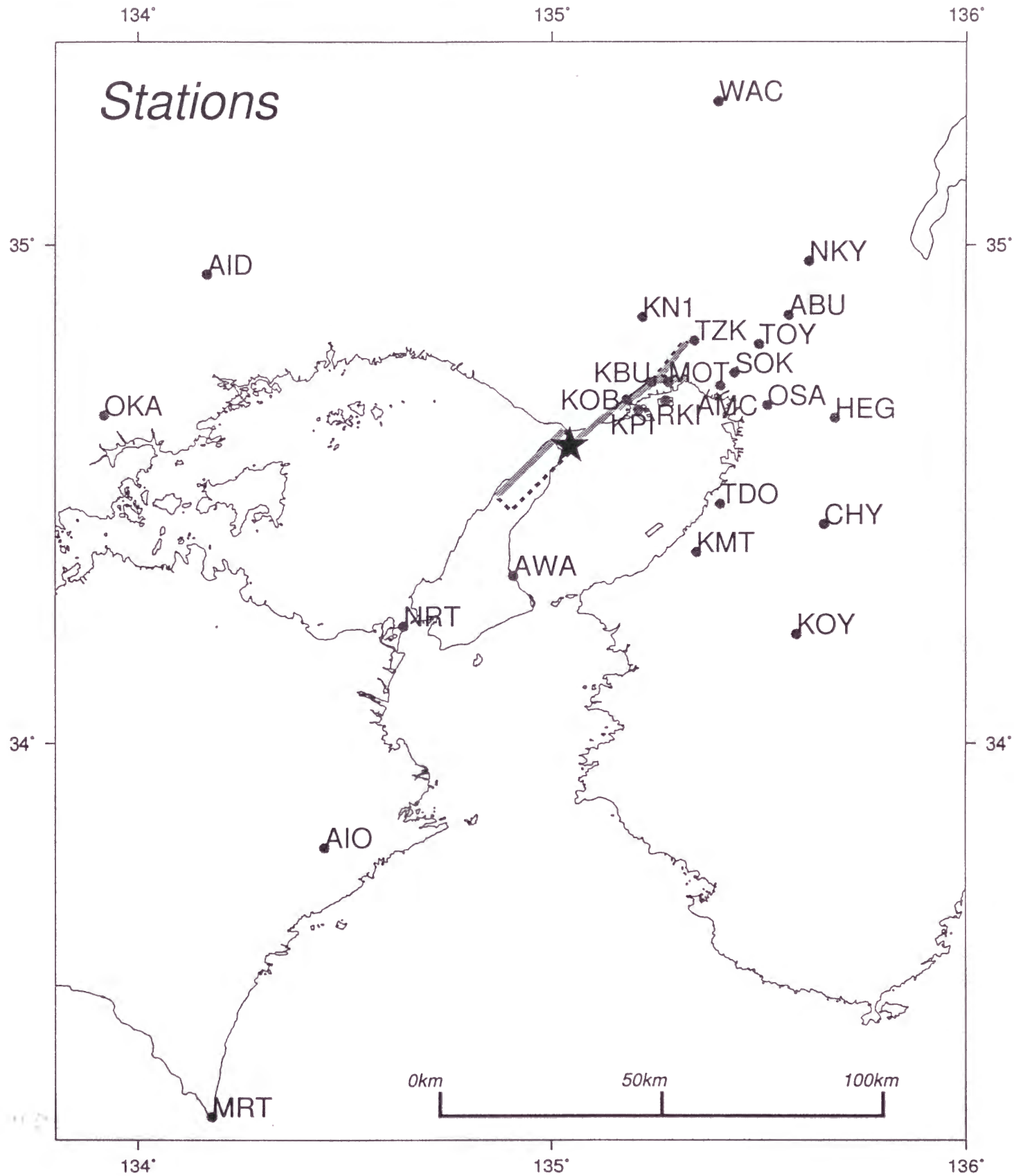
Stations
134°
135°
136°
35°
34°
WAC
NKY
AID
KN1
ABU
TZK
TOY
SOK
KBU
MOT
OKA
KOB
AMC
OSA
HEG
KPI
RKI
TDO
CHY
KMT
AWA
NRT
KOY
AIO
MRT
0km
50km
100km

Figure 1.11

Inversion Results with Different Smoothing Strengths

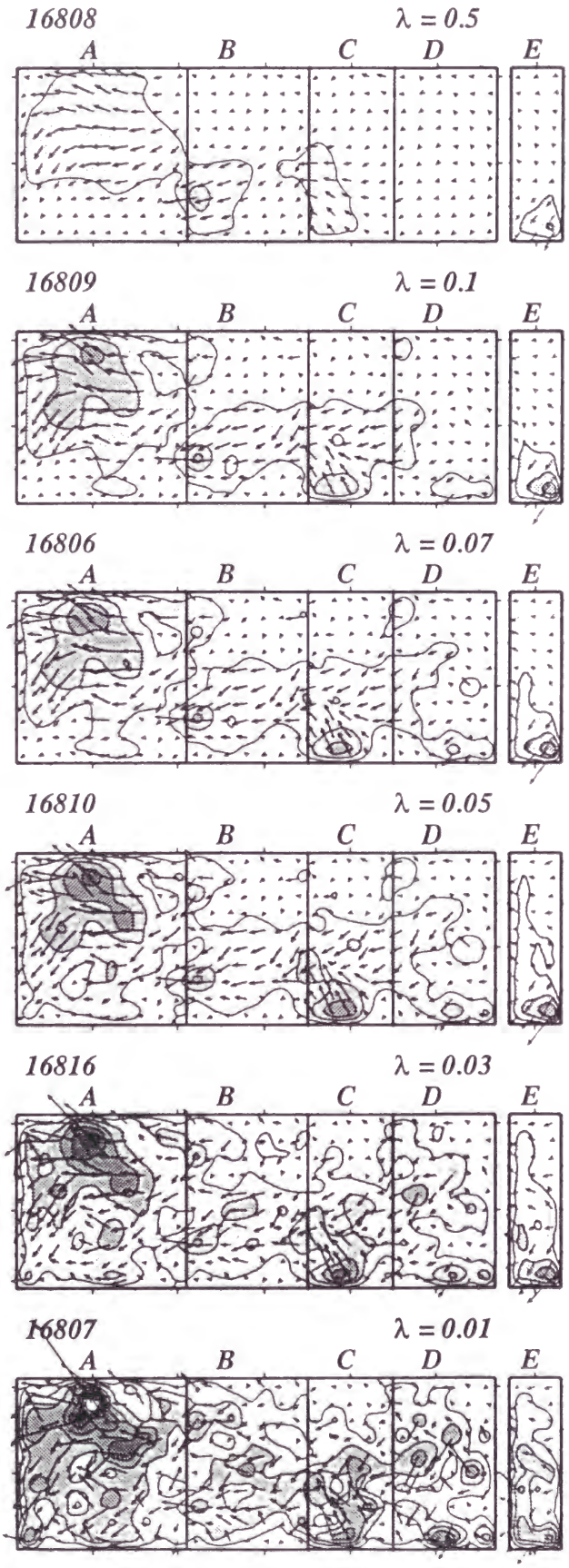

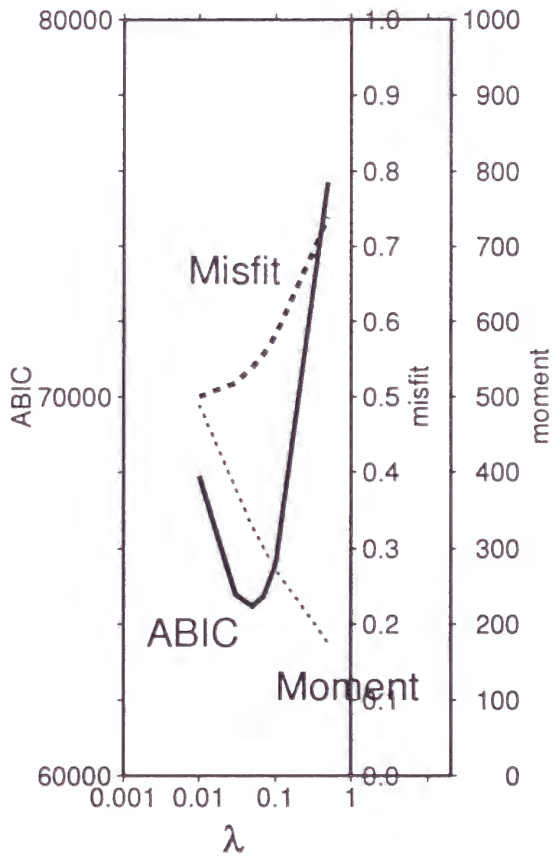

Figure 1.12

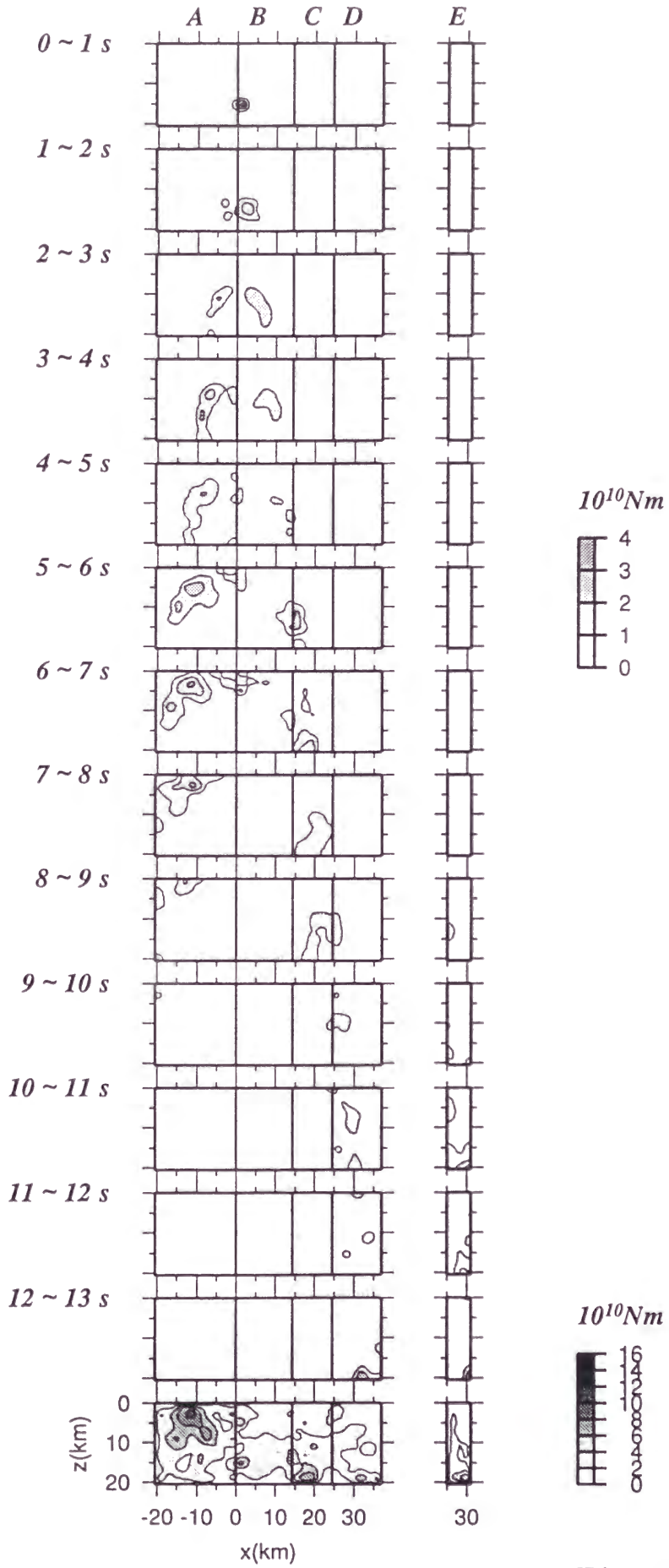
A
B
C
D
E
0 ~ 1 s
1 ~ 2 s
2 ~ 3 s
3 ~ 4 s
4 ~ 5 s
5 ~ 6 s
6 ~ 7 s
7 ~ 8 s
8 ~ 9 s
9 ~ 10 s
10 ~ 11 s
11 ~ 12 s
12 ~ 13 s
10^{10}Nm
4
3
2
1
0
10^{10}Nm
16
14
12
10
8
6
4
2
0
z(km)
0
10
20
-20 -10 0 10 20 30
30
x(km)

Figure 1.13

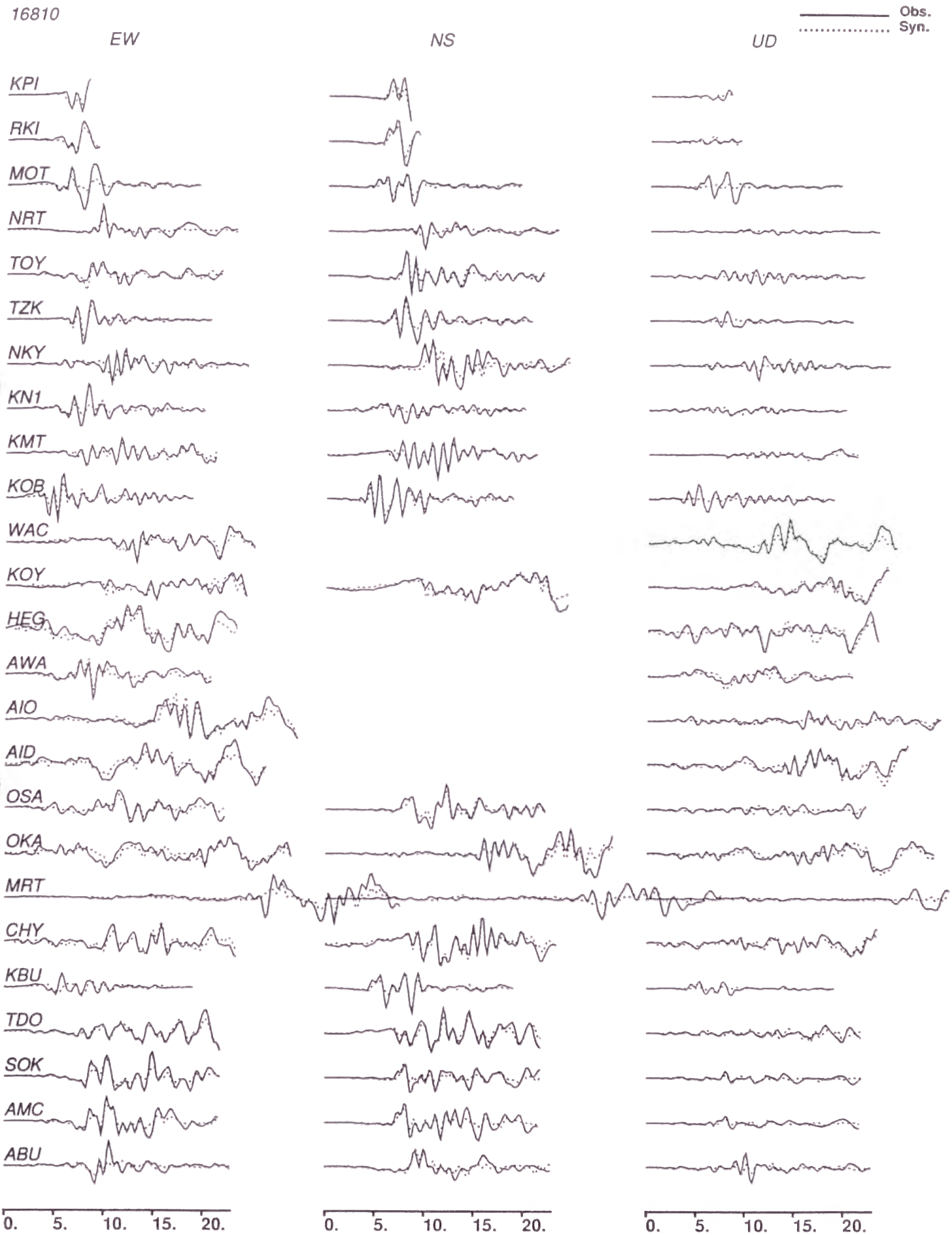
16810
Obs.
Syn.
EW
NS
UD
KPI
RKI
MOT
NRT
TOY
TZK
NKY
KN1
KMT
KOB
WAC
KOY
HEG
AWA
AIO
AID
OSA
OKA
MRT
CHY
KBU
TDO
SOK
AMC
ABU
0. 5. 10. 15. 20.
0. 5. 10. 15. 20.
0. 5. 10. 15. 20.

Figure 1.14

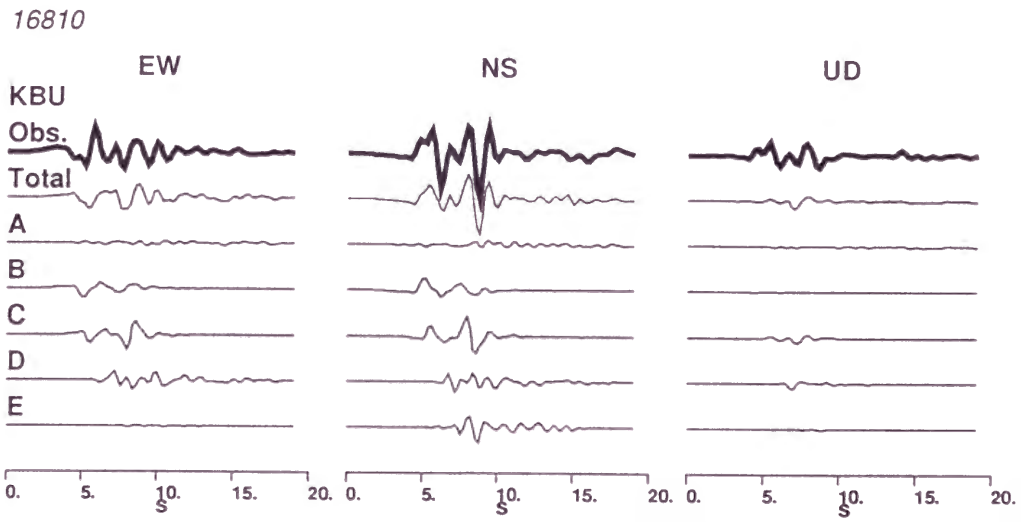

Figure 1.15

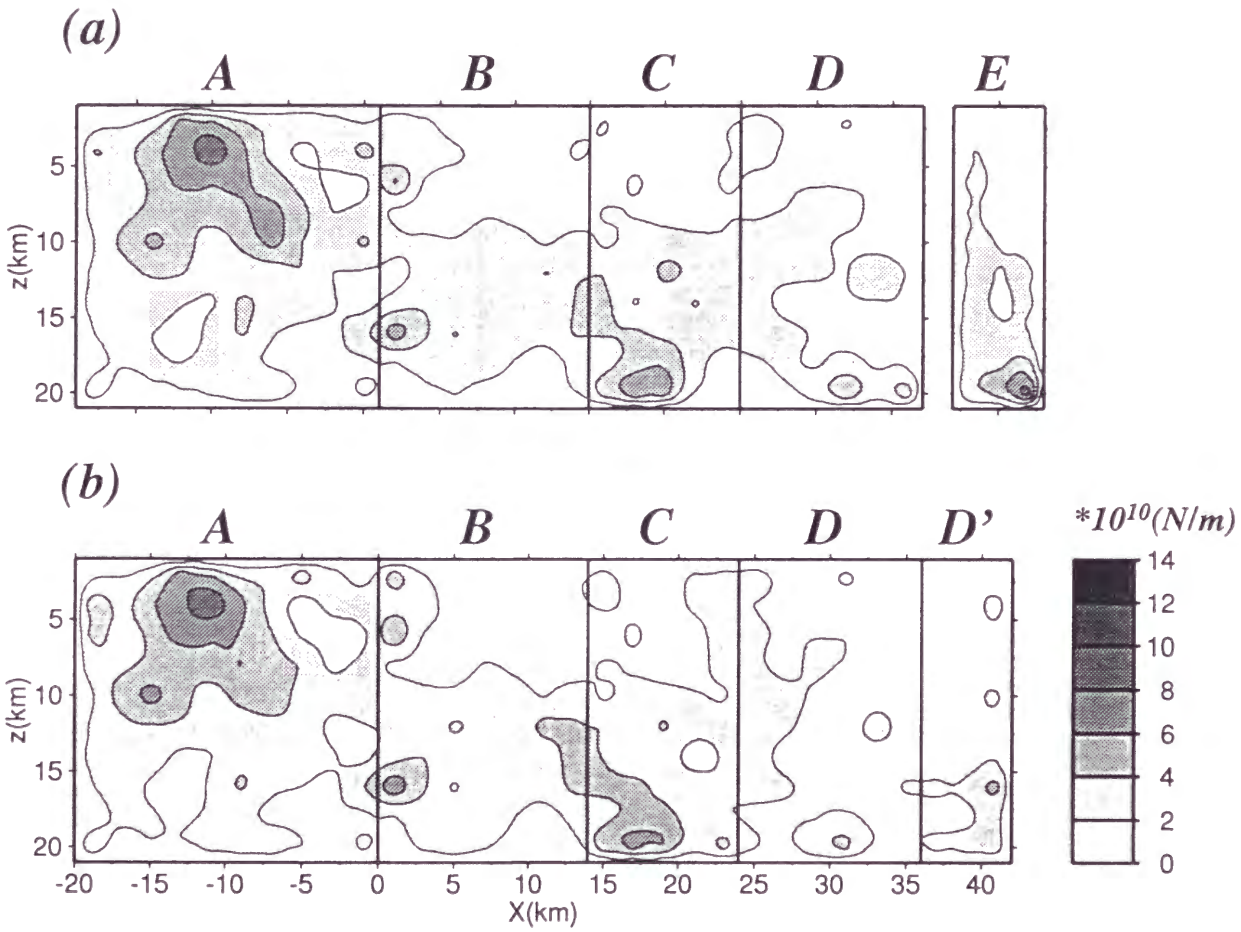
(a)
A
B
C
D
E
z(km)
5
10
15
20
(b)
A
B
C
D
D'
z(km)
5
10
15
20
-20
-15
-10
-5
0
5
10
15
20
25
30
35
40
X(km)
*10^10(N/m)
14
12
10
8
6
4
2
0

Figure 1.16

Resolution Check 2

Effect of Random Noise

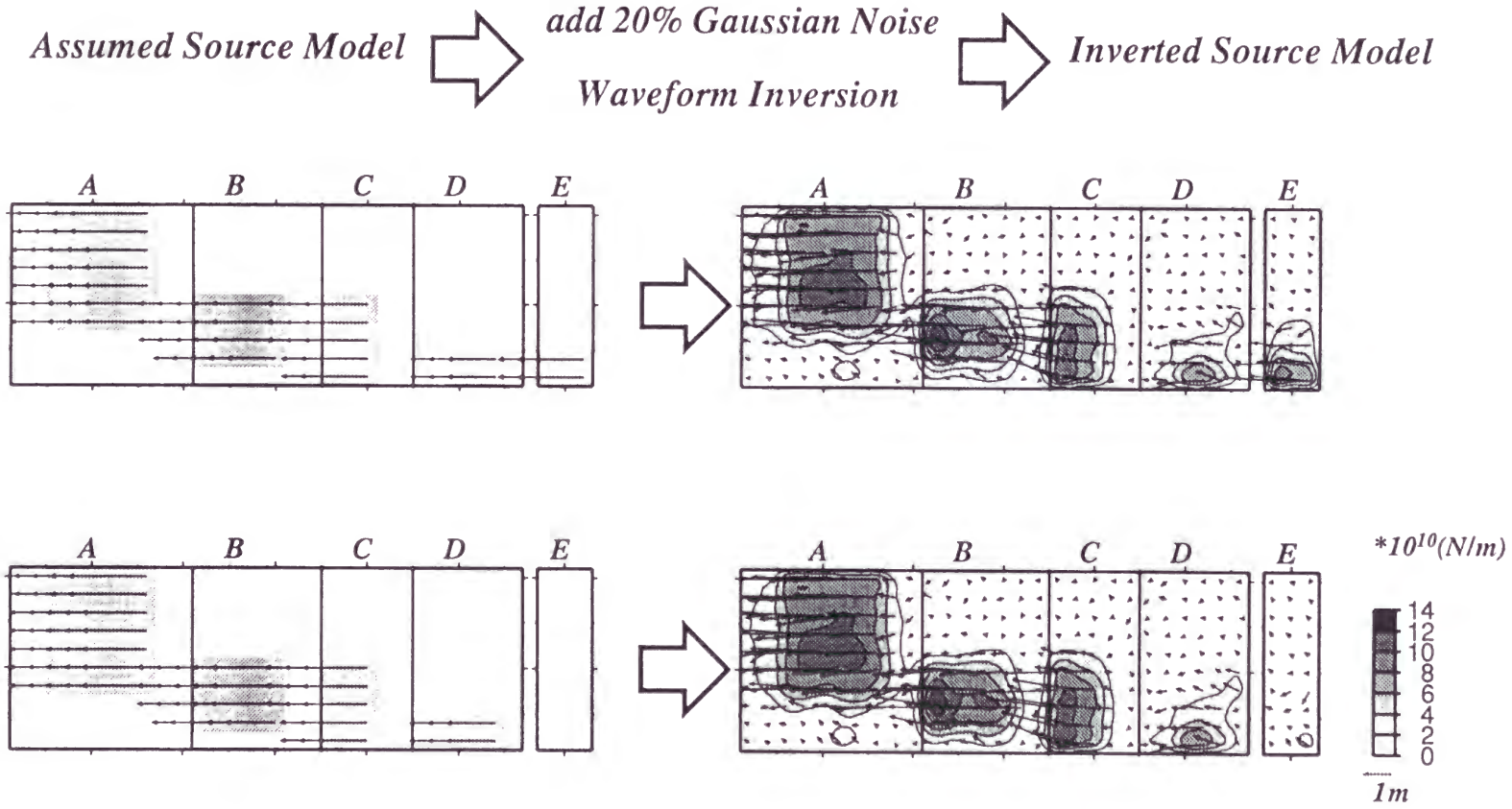

Figure 1.17

Resolution Check 3

Effect of Misestimation of Velocity Structure

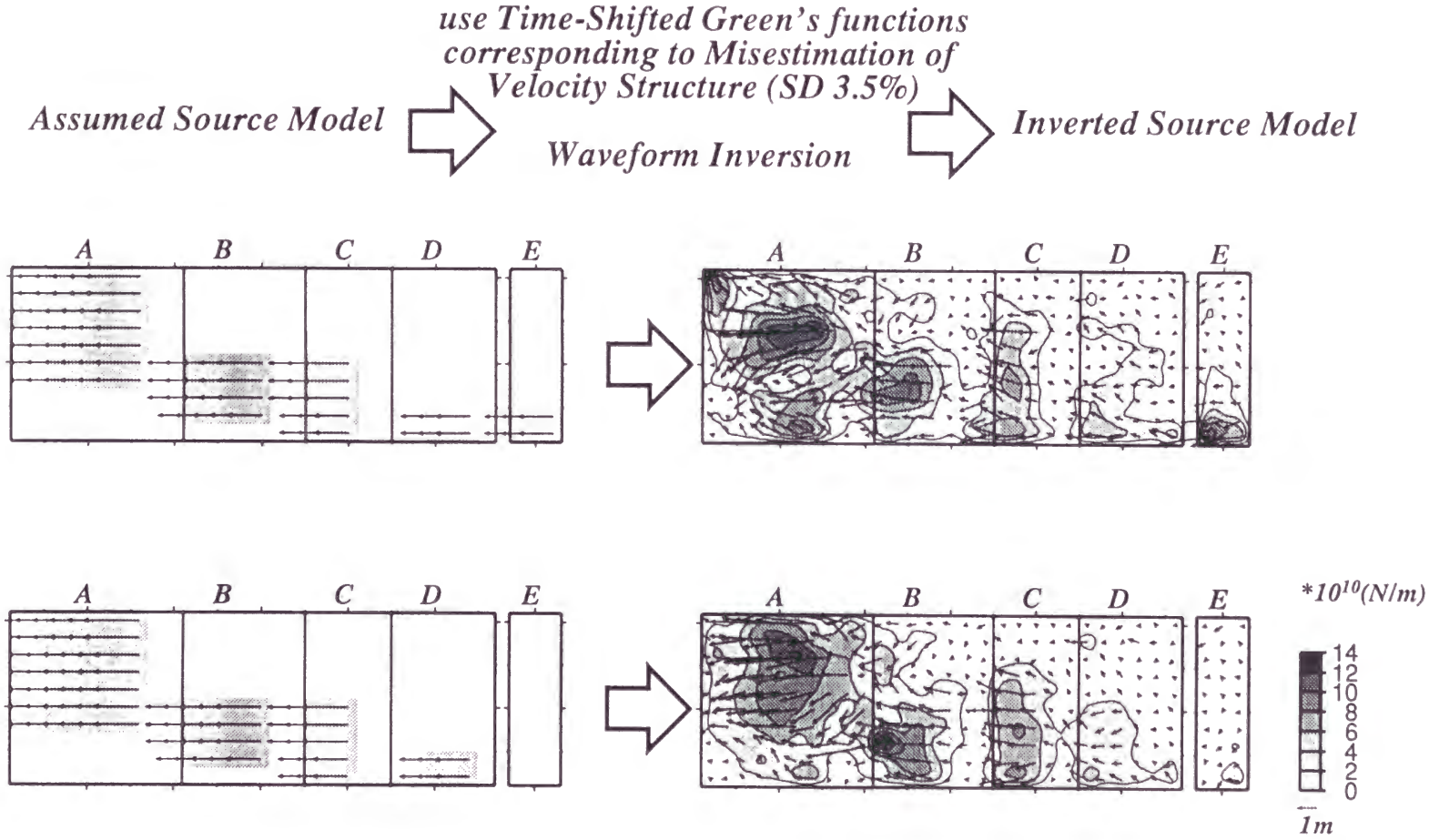

Figure 1.18

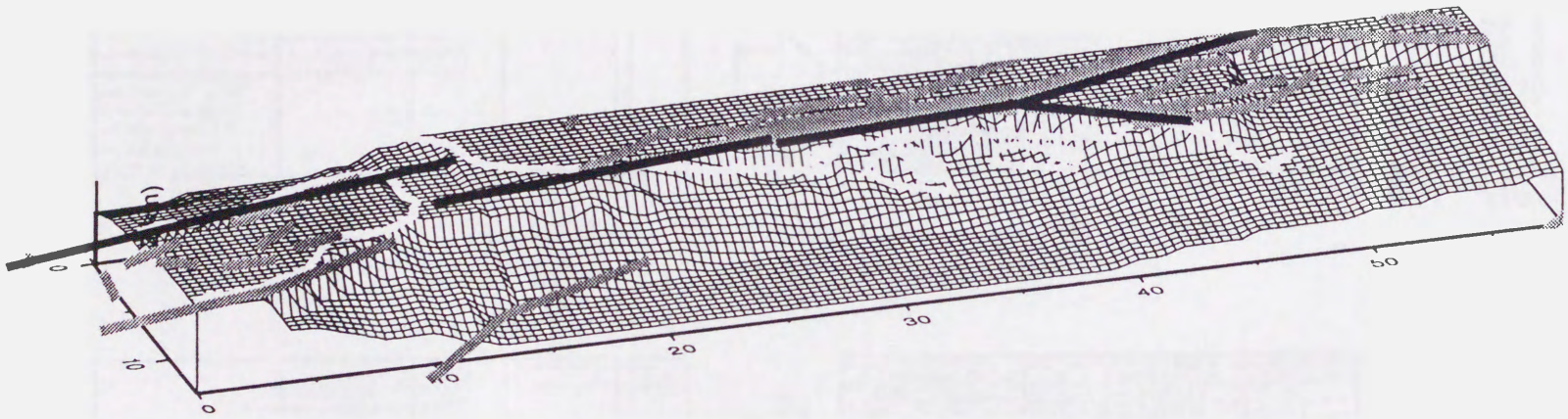

Figure 1.19

Max. Velocity Distribution (0.1-1.0 Hz)

Sediment 2-layer model

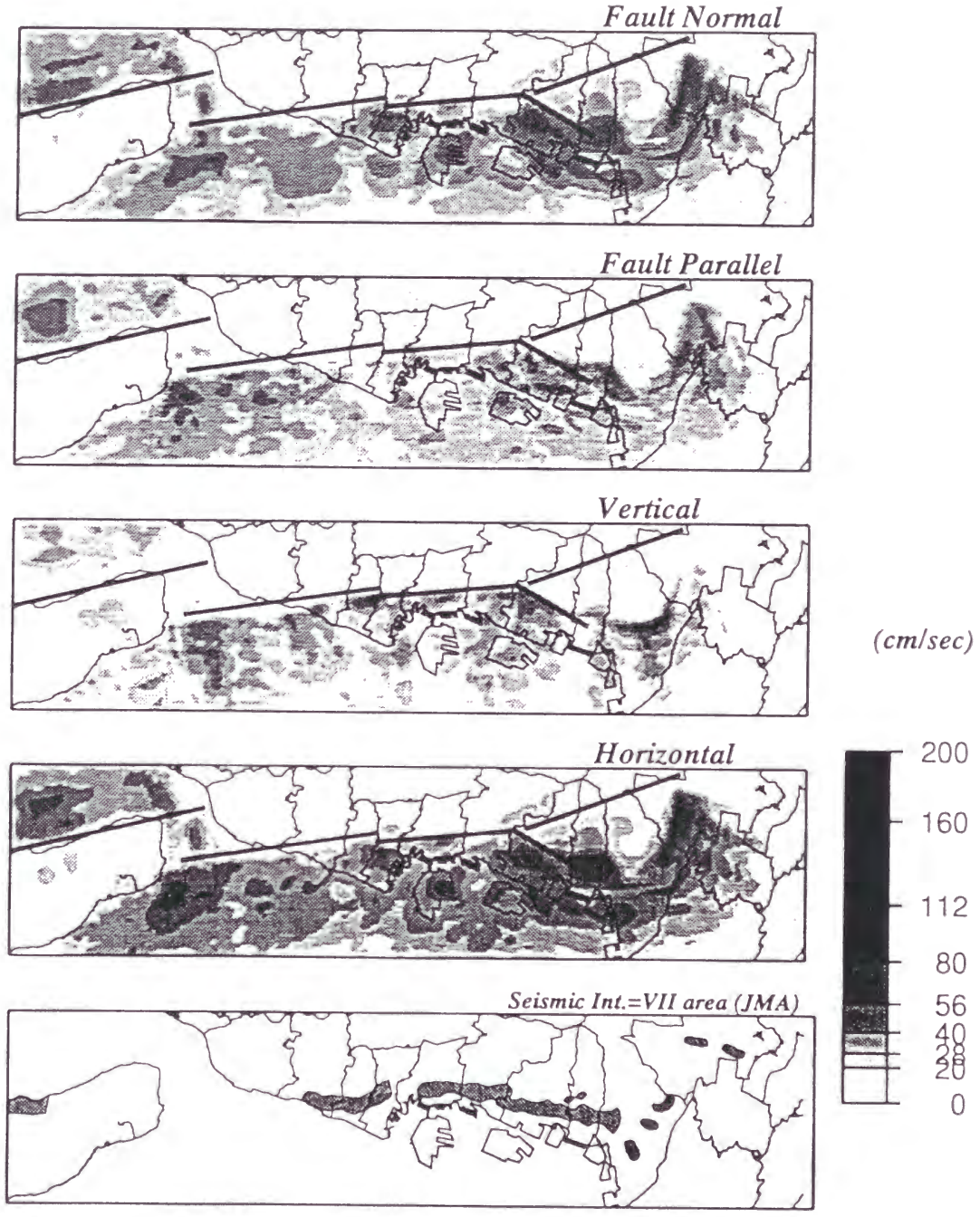

Figure 1.20(a)

Max. Velocity Distribution (0.1-1.0 Hz)

Sediment 2-layer model

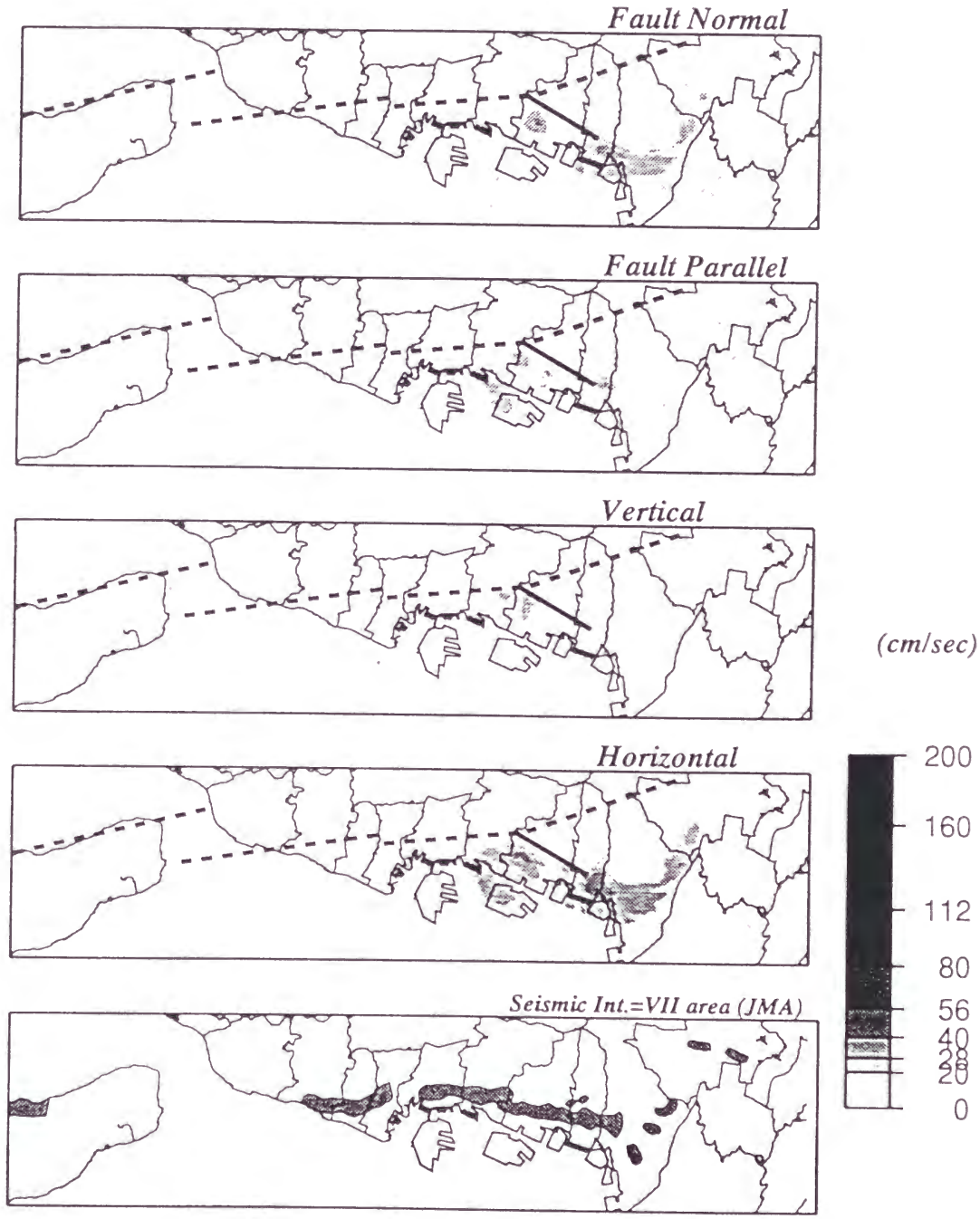

Figure 1.20(b)

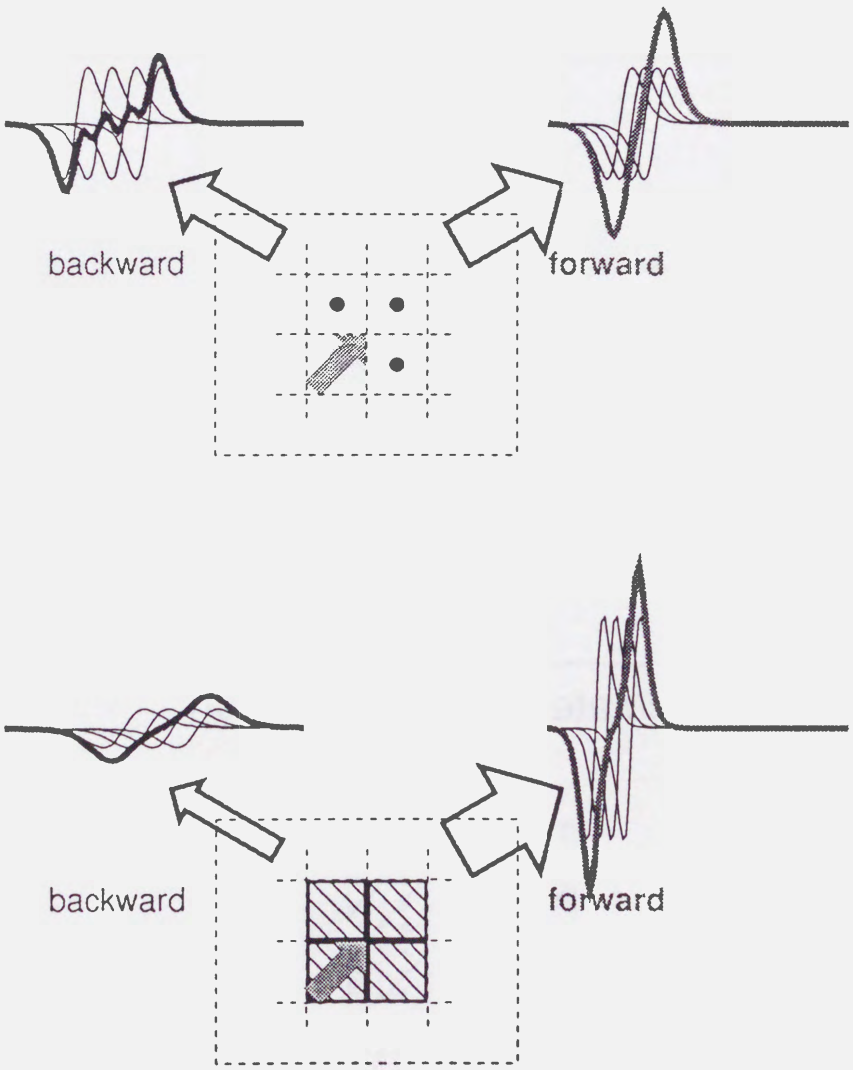

Figure 2.1

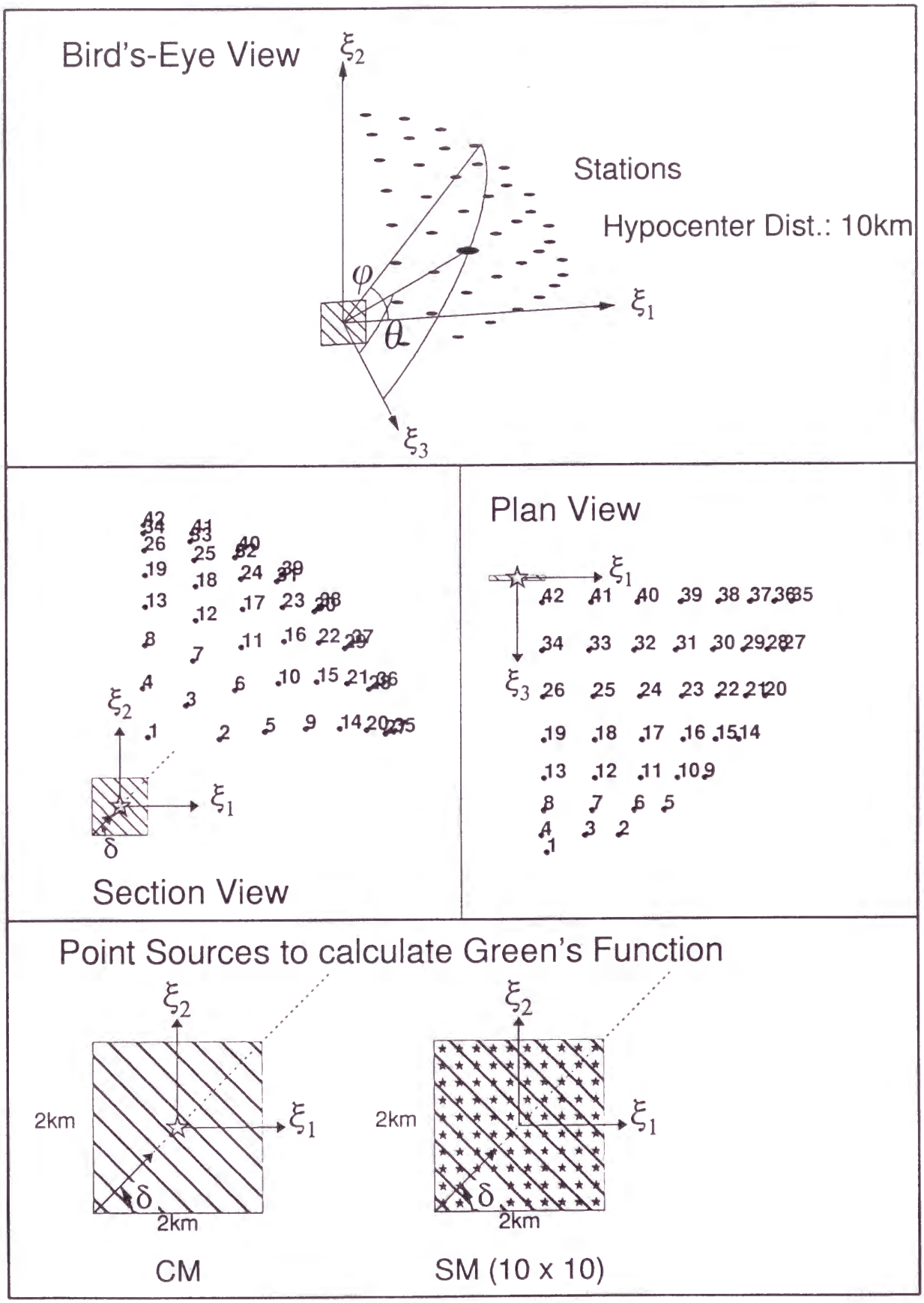
Bird's-Eye View
ξ_2
Stations
Hypocenter Dist.: 10km
φ
θ
ξ_1
ξ_3
Plan View
Section View
δ
Point Sources to calculate Green's Function
2km
2km
CM
SM (10 x 10)

Figure 2.2

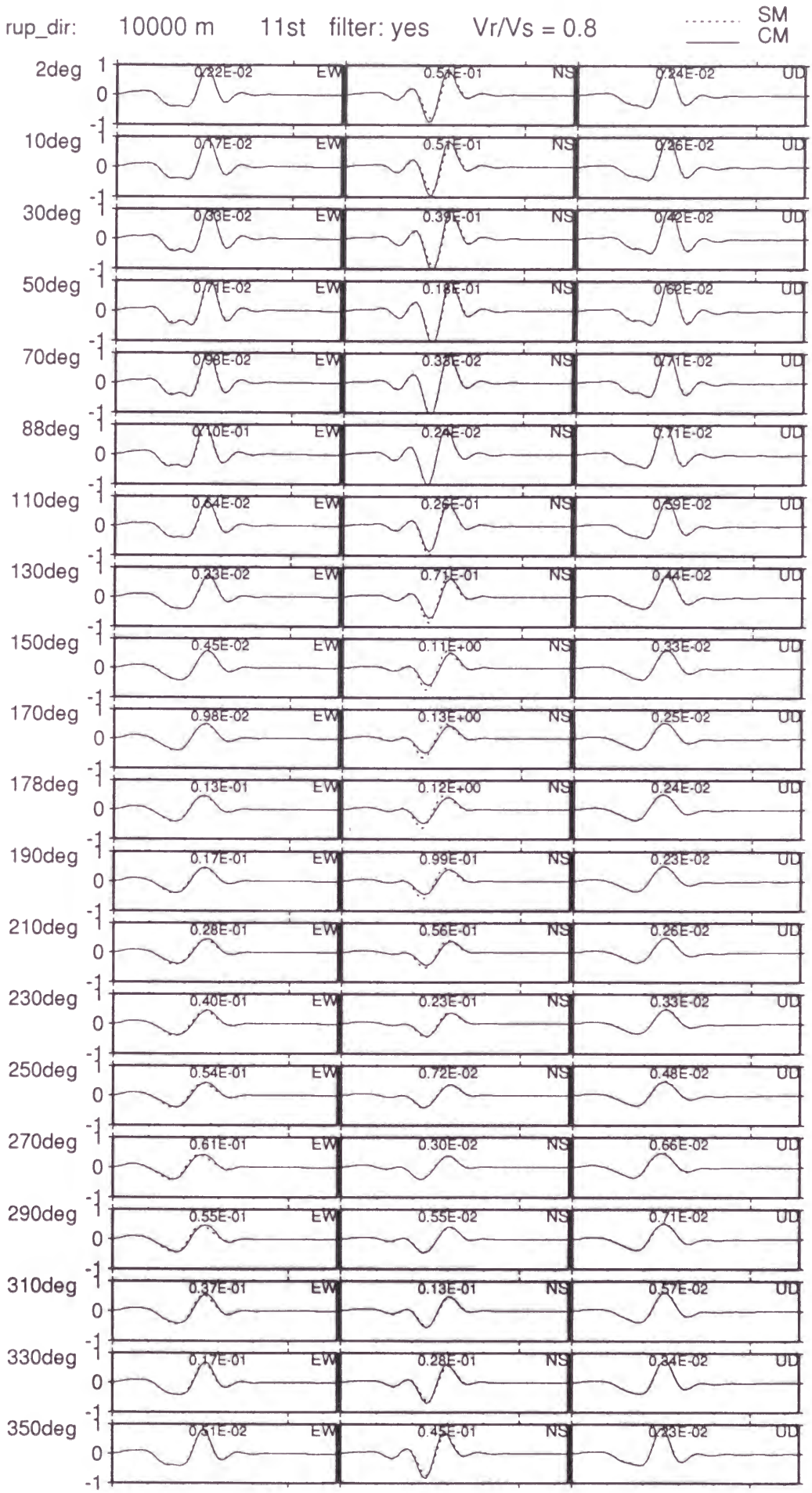
rup_dir: 10000 m 11st filter: yes Vr/Vs = 0.8
SM
CM
2deg
10deg
30deg
50deg
70deg
88deg
110deg
130deg
150deg
170deg
178deg
190deg
210deg
230deg
250deg
270deg
290deg
310deg
330deg
350deg
EW
NS
UD

Figure 2.3

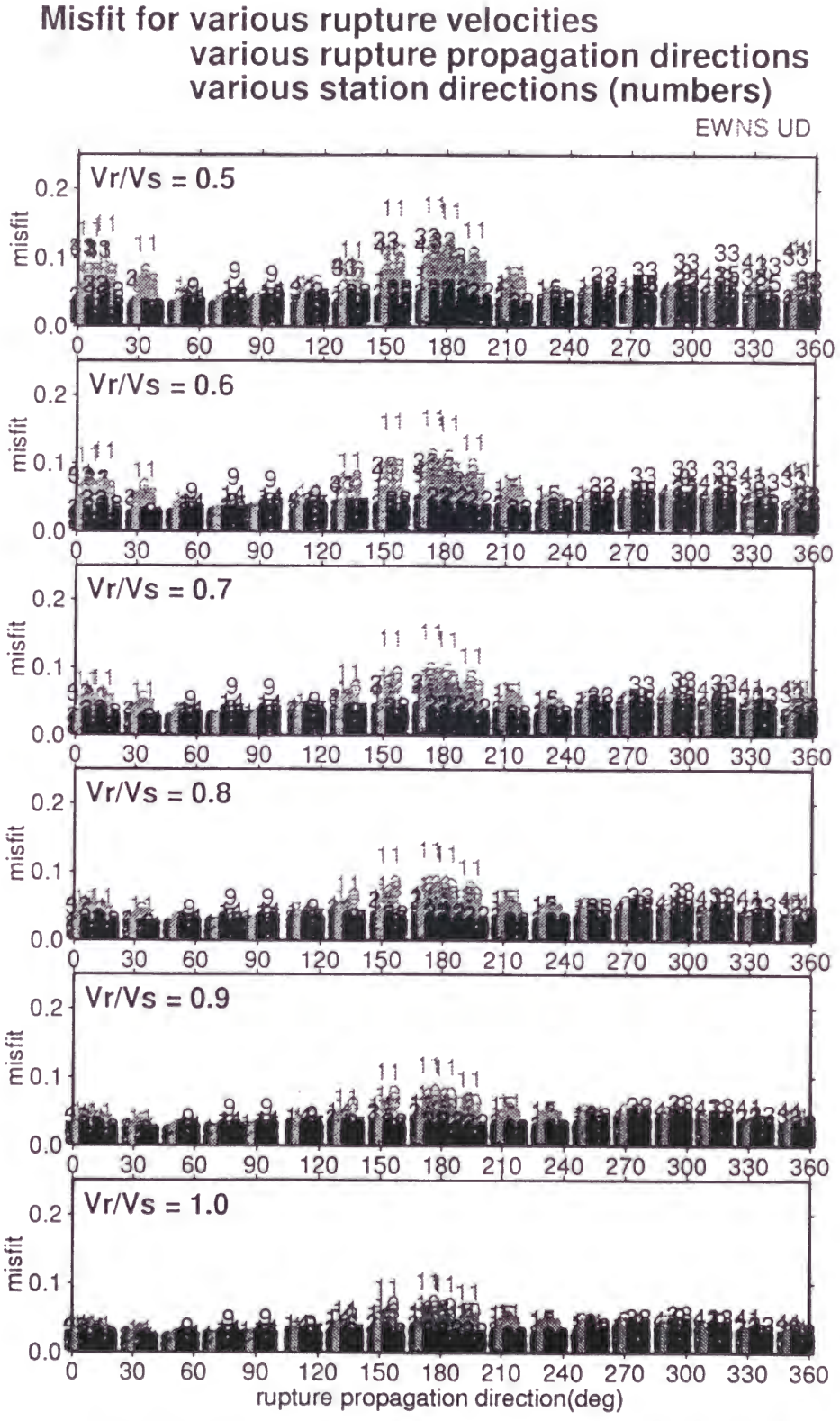
Misfit for various rupture velocities
various rupture propagation directions
various station directions (numbers)
EWNS UD
Vr/Vs = 0.5
Vr/Vs = 0.6
Vr/Vs = 0.7
Vr/Vs = 0.8
Vr/Vs = 0.9
Vr/Vs = 1.0
misfit
0.0
0.1
0.2
0 30 60 90 120 150 180 210 240 270 300 330 360
rupture propagation direction(deg)

Figure 2.4

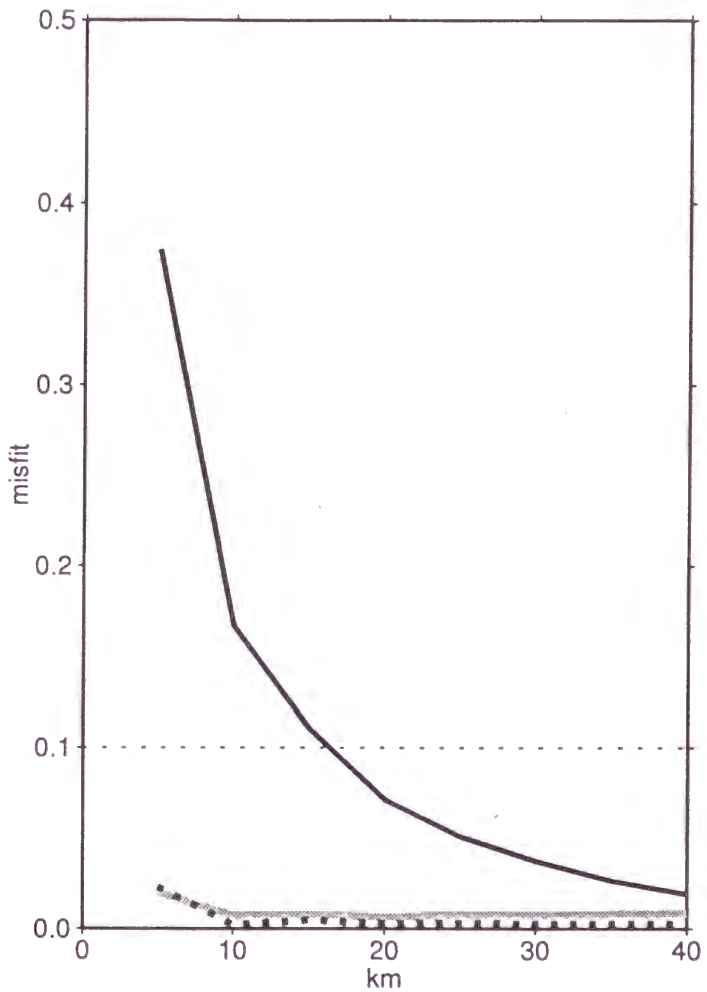

MISFIT vs HYPO_DIST.
for fixed size of source (2km x 2km)
fixed Vrup (0.5 Vs)
fixed station (11st)
fixed rupture propagation direction (170°)

EW
NS
UD

Figure 2.5

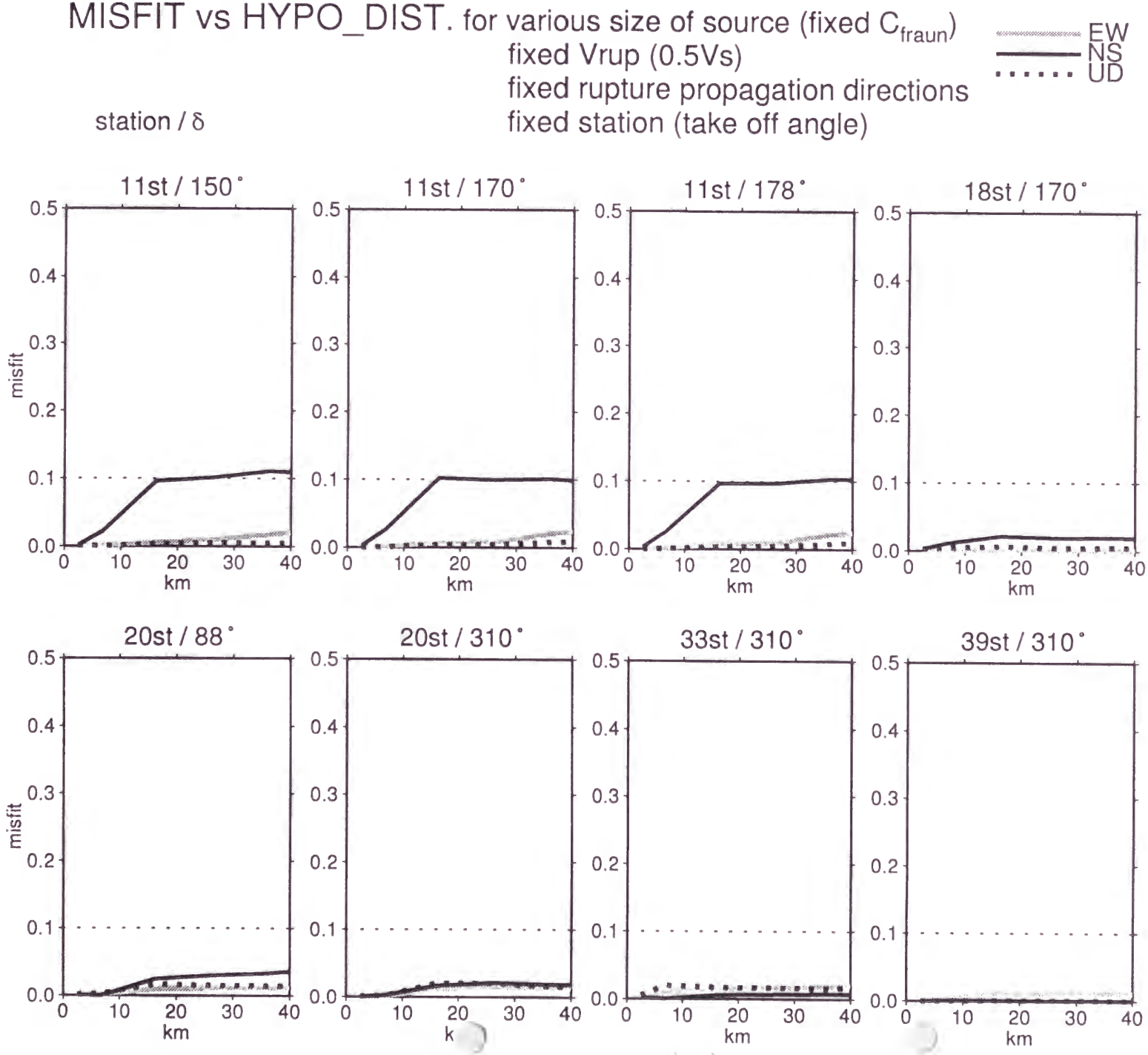
MISFIT vs HYPO_DIST. for various size of source (fixed C_{fraun})
fixed Vrup (0.5Vs)
fixed rupture propagation directions
fixed station (take off angle)
station / δ
EW
NS
UD
11st / 150°
11st / 170°
11st / 178°
18st / 170°
20st / 88°
20st / 310°
33st / 310°
39st / 310°
misfit
km
0.0
0.1
0.2
0.3
0.4
0.5
0
10
20
30
40

Figure 2.6

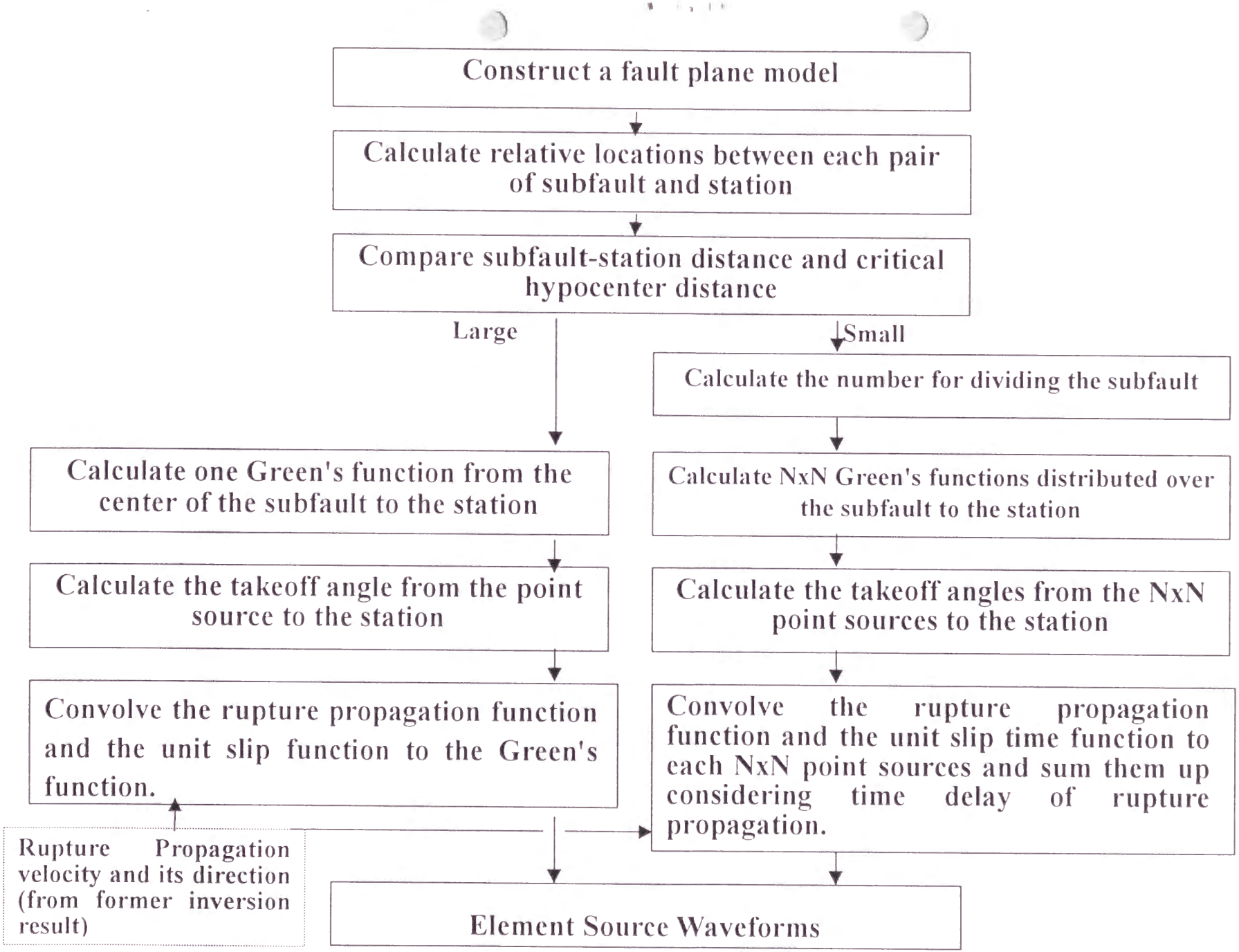
Construct a fault plane model
Calculate relative locations between each pair of subfault and station
Compare subfault-station distance and critical hypocenter distance
Large
Small
Calculate the number for dividing the subfault
Calculate one Green's function from the center of the subfault to the station
Calculate NxN Green's functions distributed over the subfault to the station
Calculate the takeoff angle from the point source to the station
Calculate the takeoff angles from the NxN point sources to the station
Convolve the rupture propagation function and the unit slip function to the Green's function.
Convolve the rupture propagation function and the unit slip time function to each NxN point sources and sum them up considering time delay of rupture propagation.
Rupture Propagation velocity and its direction (from former inversion result)
Element Source Waveforms

Figure 2.7

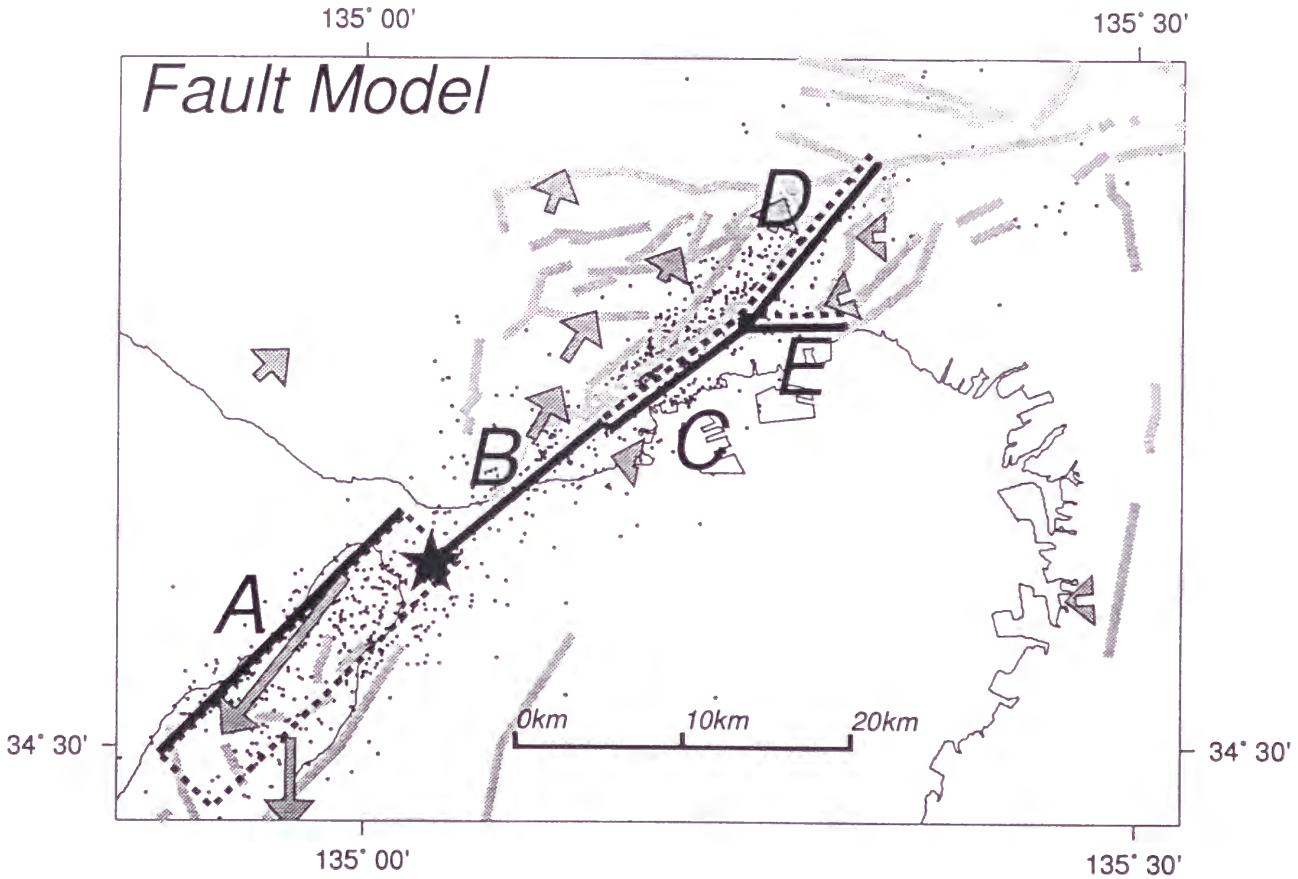
135° 00'
135° 30'
Fault Model
D
E
B
C
A
0km
10km
20km
34° 30'
34° 30'
135° 00'
135° 30'

Figure 2.8

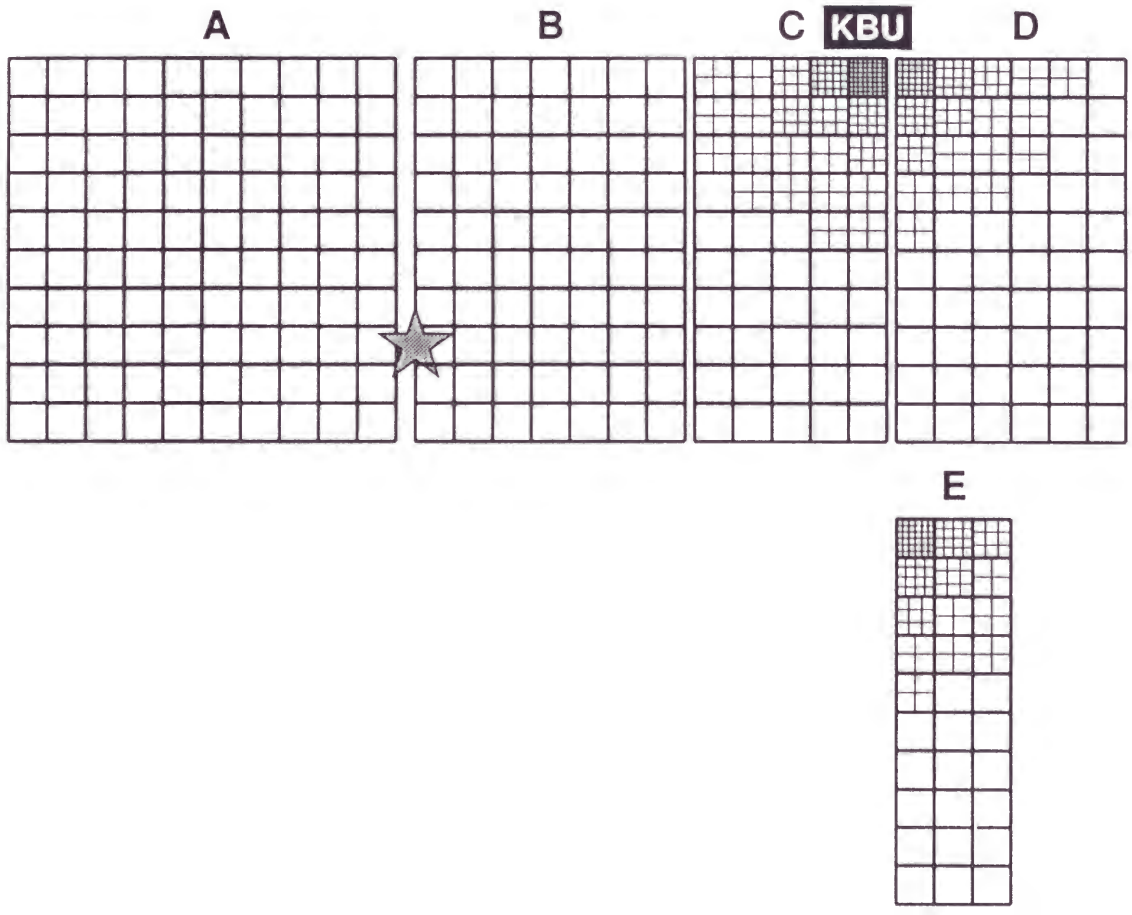

Figure 2.9

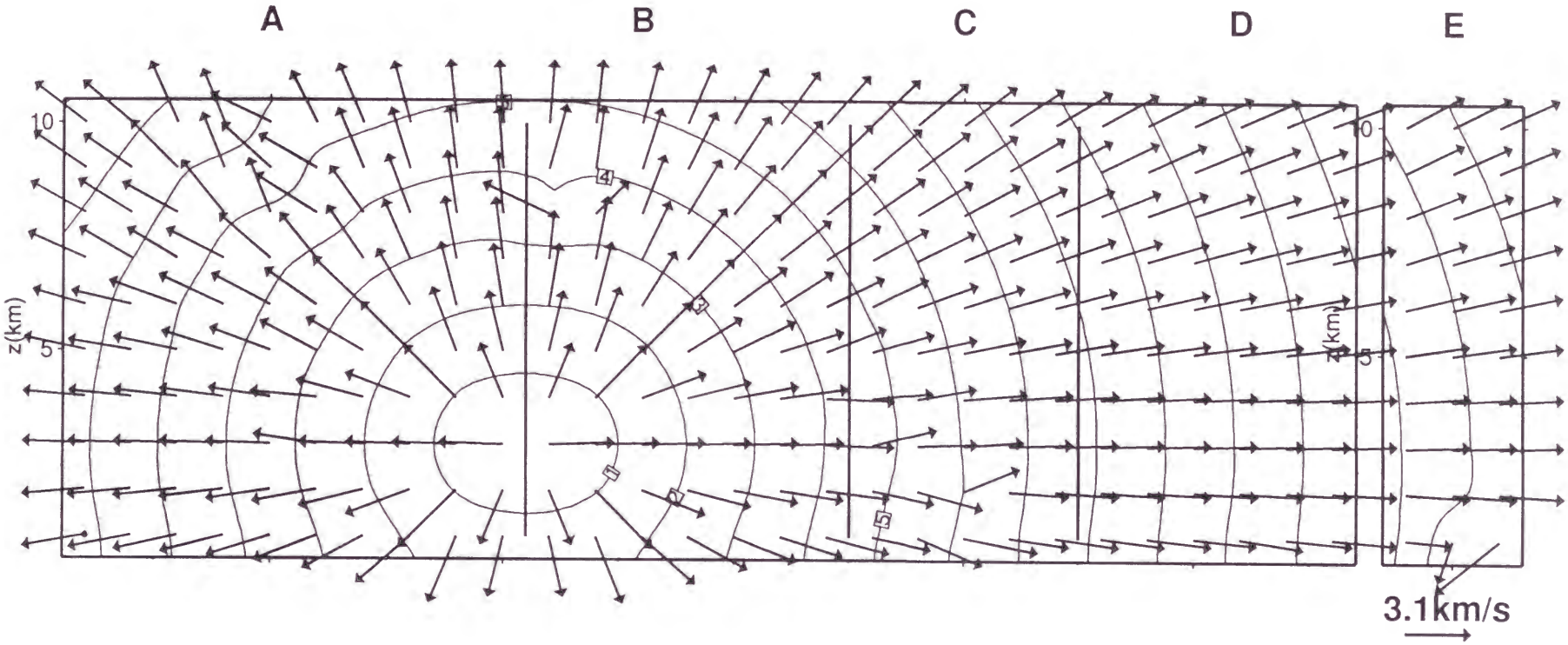

Figure 2.10

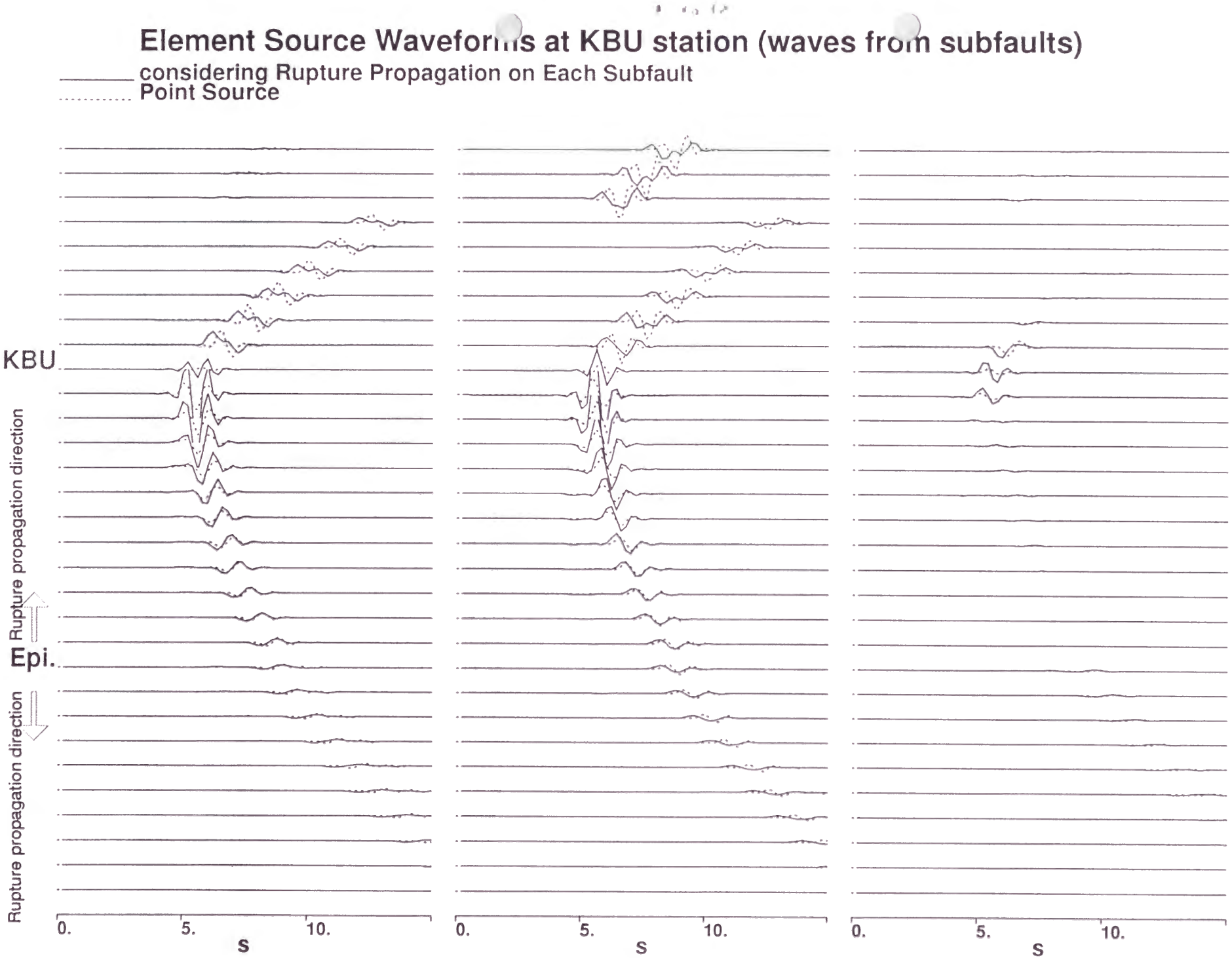
Element Source Waveforms at KBU station (waves from subfaults)
considering Rupture Propagation on Each Subfault
Point Source
KBU
Rupture propagation direction
Epi.
Rupture propagation direction
0.
5.
10.
S
0.
5.
10.
S
0.
5.
10.
S

Figure 2.11

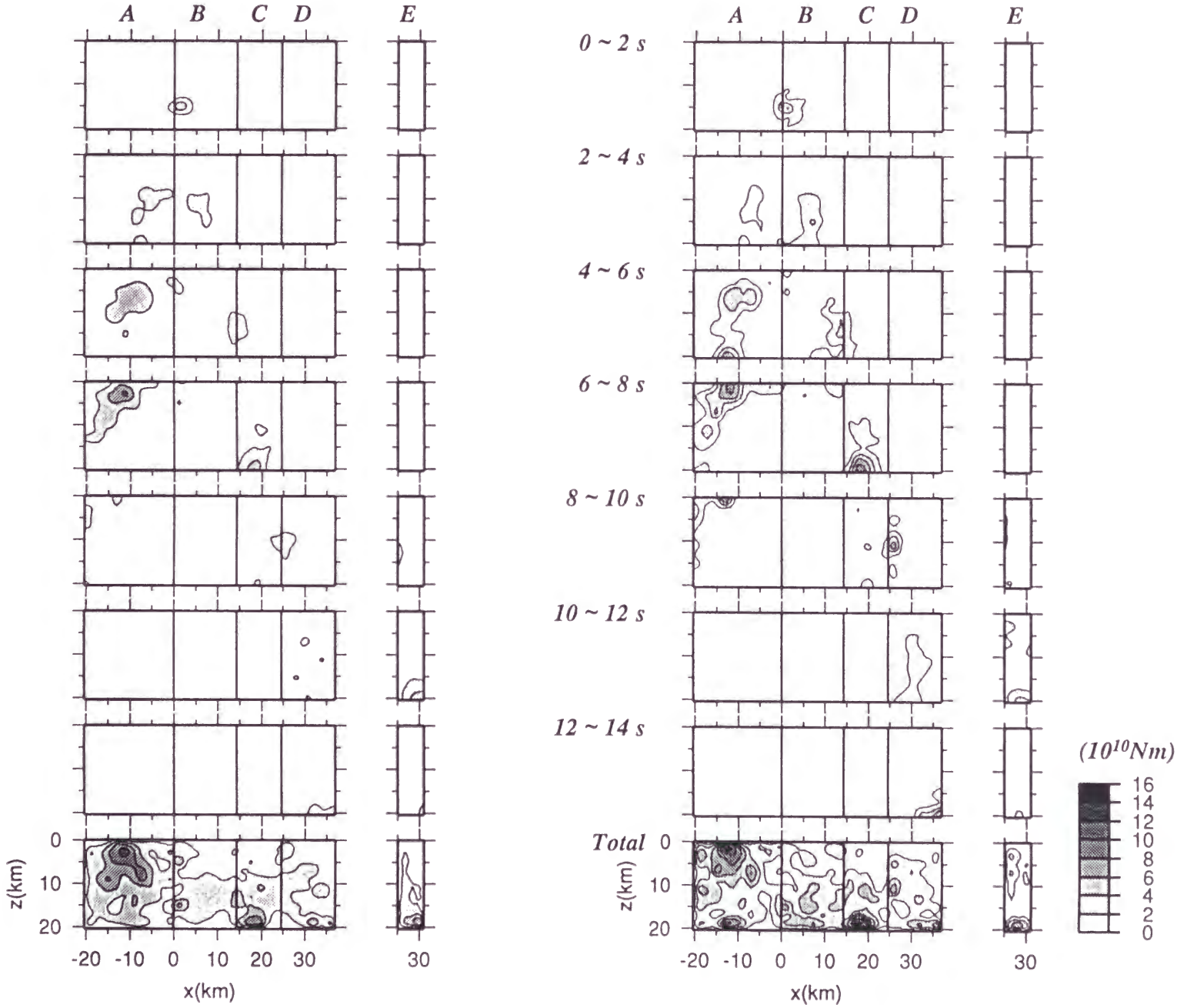
A
B
C
D
E
0 ~ 2 s
2 ~ 4 s
4 ~ 6 s
6 ~ 8 s
8 ~ 10 s
10 ~ 12 s
12 ~ 14 s
Total
z(km)
0
10
20
-20 -10 0 10 20 30
30
x(km)
(10^10Nm)
16
14
12
10
8
6
4
2
0

Figure 2.12

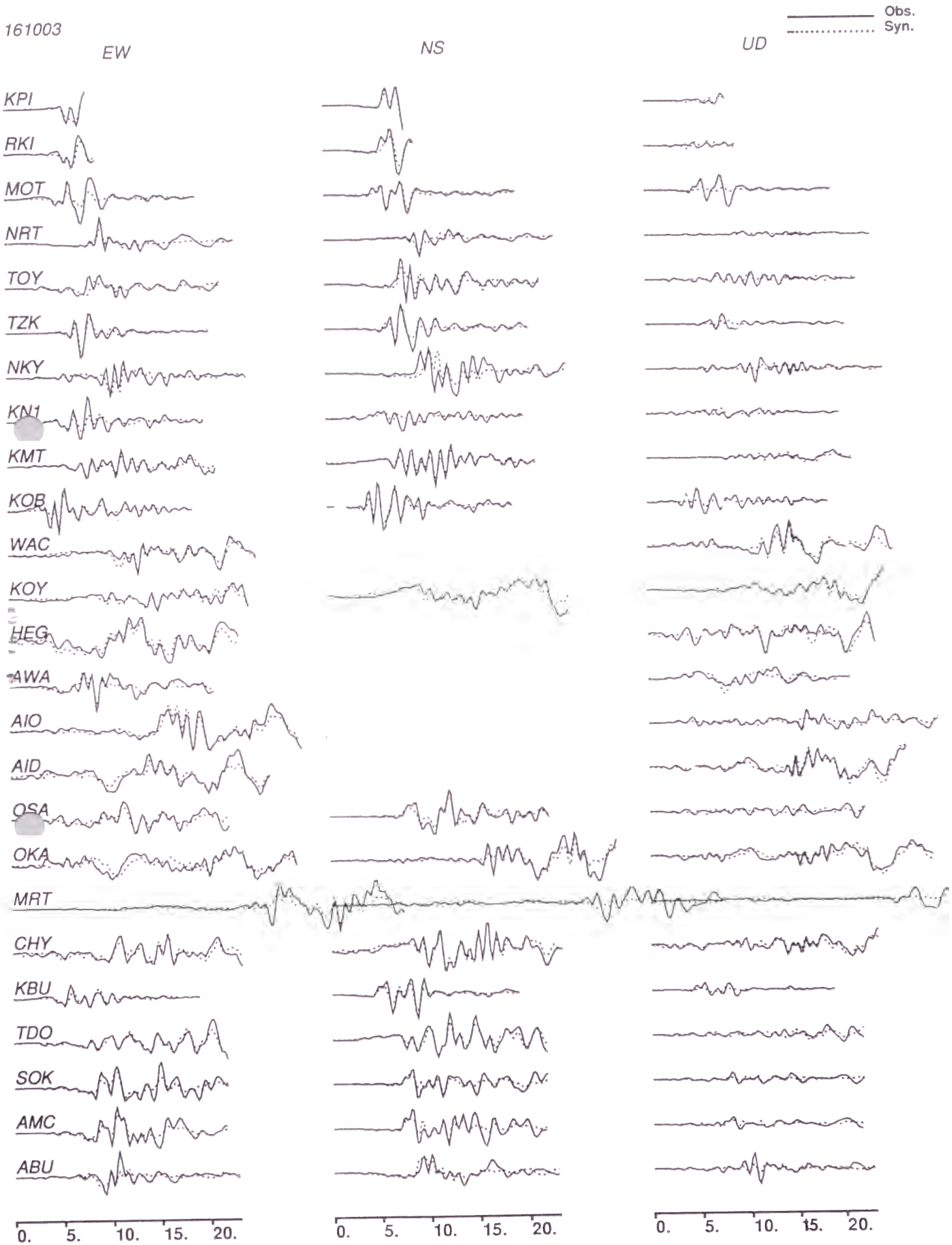
161003
EW
NS
UD
Obs.
Syn.
KPI
RKI
MOT
NRT
TOY
TZK
NKY
KN1
KMT
KOB
WAC
KOY
HEG
AWA
AIO
AID
OSA
OKA
MRT
CHY
KBU
TDO
SOK
AMC
ABU
0.
5.
10.
15.
20.

Figure 2.13

(a)

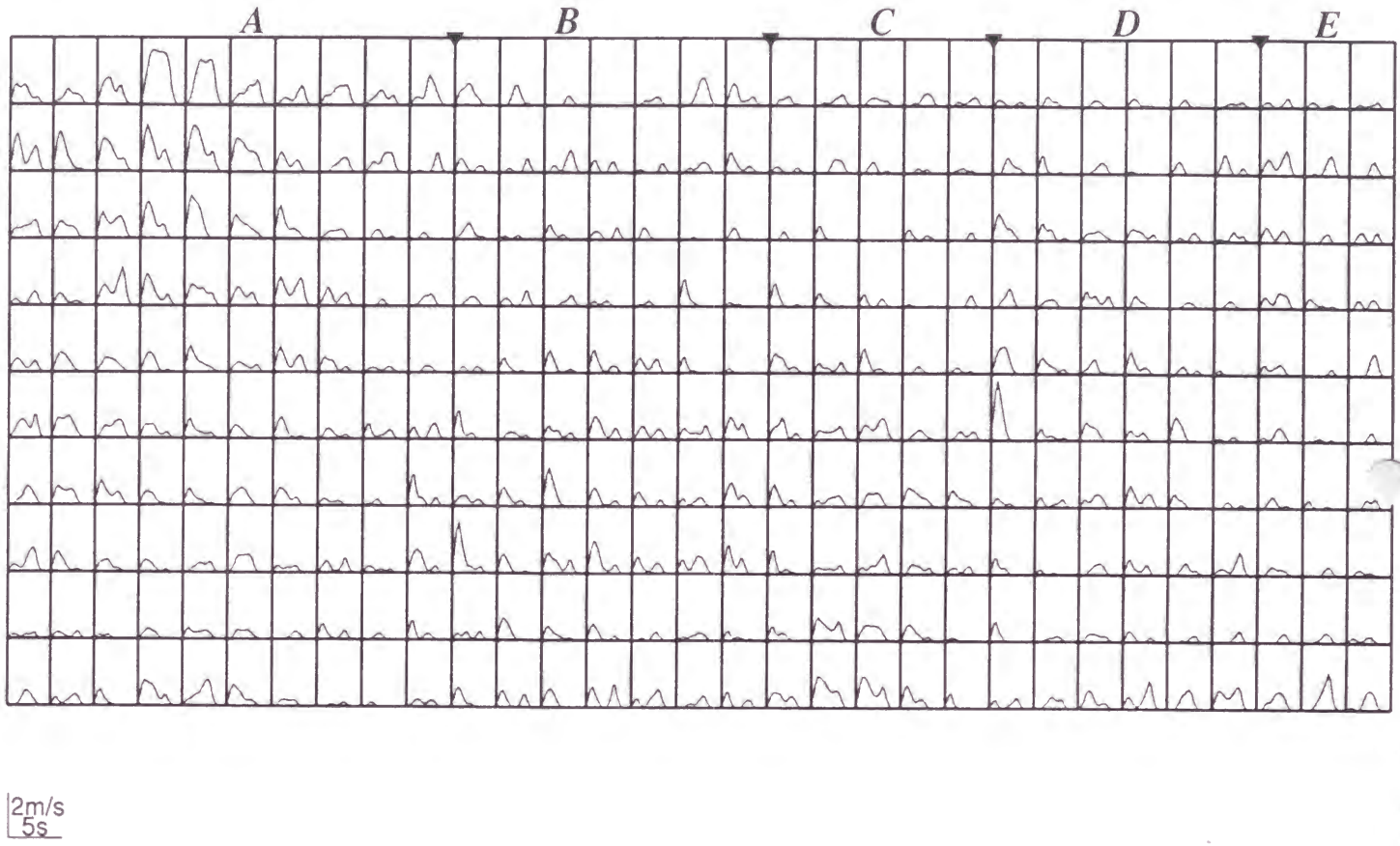

(b)

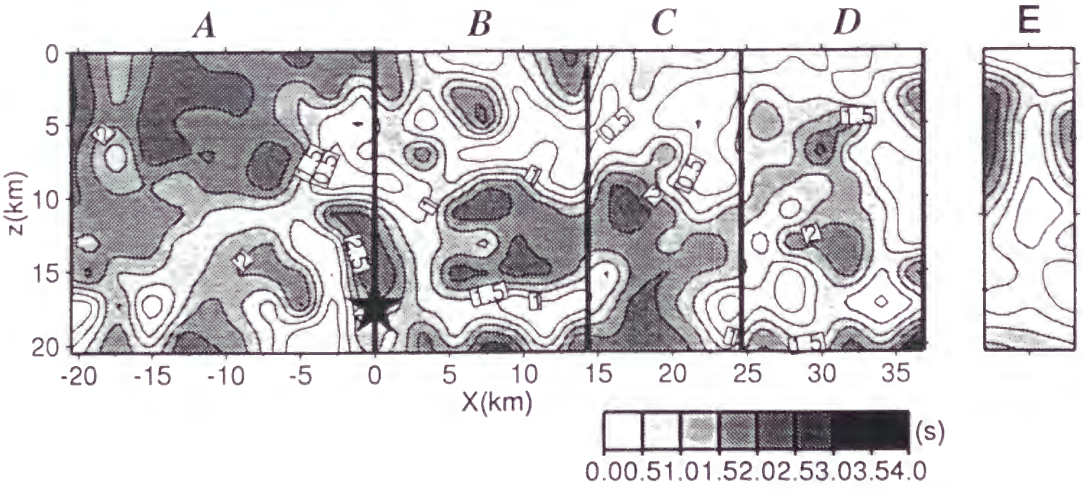

Figure 2.14

Max. Velocity Distribution (0.1-1.0 Hz)

Sediment 2-layer model, CM

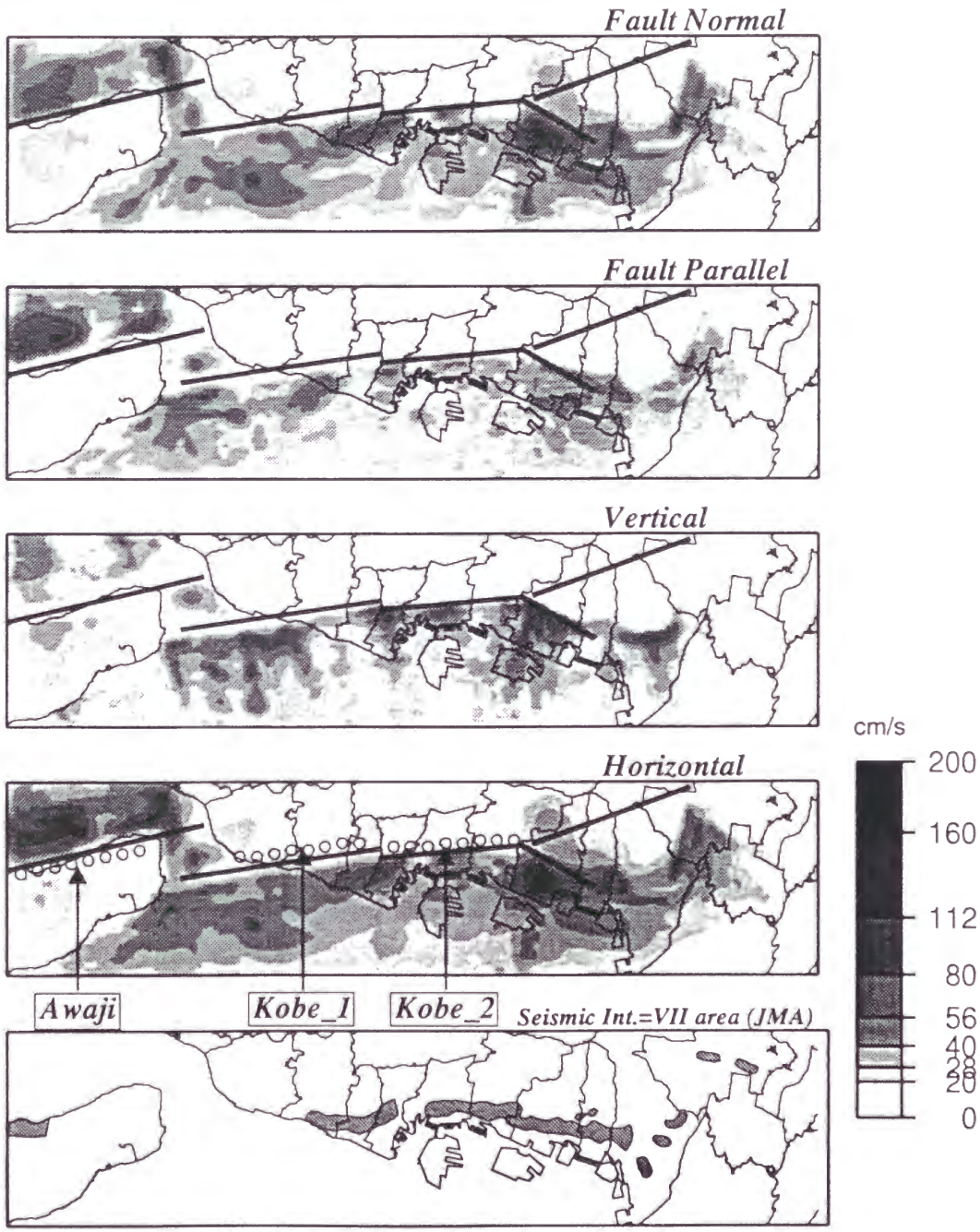

Figure 2.15

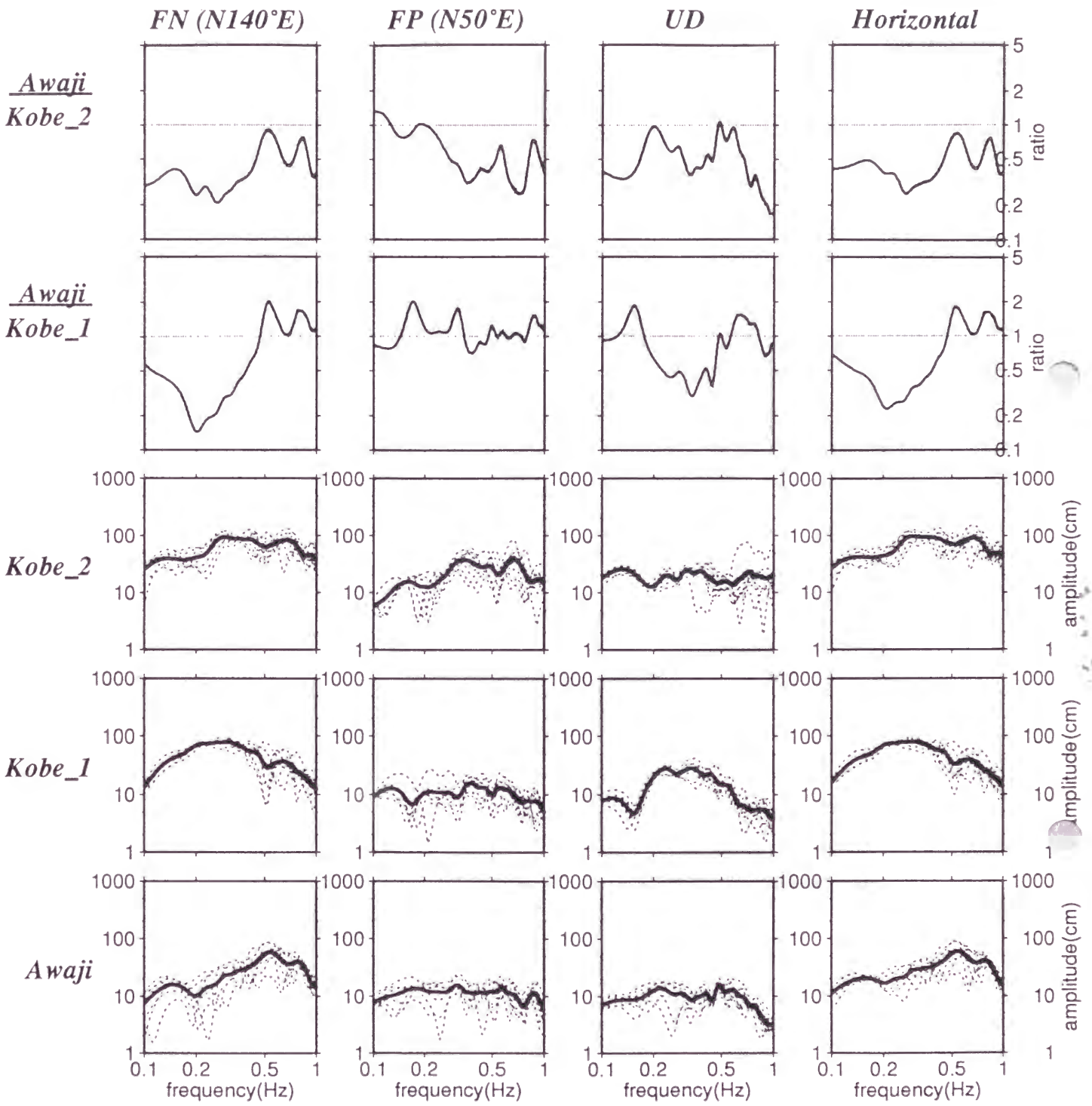
FN (N140°E)
FP (N50°E)
UD
Horizontal
Awaji
Kobe_2
Awaji
Kobe_1
ratio
Kobe_2
Kobe_1
Awaji
amplitude(cm)
frequency(Hz)

Figure 2.16